UPC CTTC

Heat transfer and fluid-dynamics in double and single skin facades

Centre Tecnològic de Transferència de Calor
Departament de Màquines i Motors Tèrmics
Universitat Politècnica de Catalunya

Débora Faggembauu

Doctoral Thesis

Débora Faggembauu

DOCTORAL THESIS

UPC – December 2006

Heat transfer and fluid-dynamics in double and single skin facades

Débora Faggembauu

TESI DOCTORAL

presentada al

Departament de Màquines i Motors Tèrmics
E.T.S.E.I.T.
Universitat Politècnica de Catalunya

per a l'obtenció del grau de

Doctor Enginyer Industrial

Terrassa, December 2006

Heat transfer and fluid-dynamics in double and single skin facades

Débora Faggembauu

Directors de la Tesi

Dr. Miquel Costa Pérez

Dr. Assensi Oliva

Dr. Manel Soria

Tribunal Qualificador

Dr. Carlos David Pérez-Segarra
Universitat Politècnica de Catalunya

Dr. Jesús Castro González
Universitat Politècnica de Catalunya

Dr. Agustín Macías Machín
Universidad de Las Palmas de Gran Canaria

Dr. Esteve Codina Macià
Universitat Politècnica de Catalunya

Dr. José Fernández Seara
Universidad de Vigo

Hoy es el día más hermoso de nuestra vida,
querido Sancho;
los obstáculos más grandes, nuestras propias
indecisiones;
nuestro enemigo más fuerte, el miedo al poderoso y
a nosotros mismos;
la cosa más fácil, equivocarnos;
la más destructiva, la mentira y el egoísmo;
la peor derrota, el desaliento;
los defectos más peligrosos, la soberbia y el rencor;
las sensaciones más gratas, la buena conciencia, el
esfuerzo para ser mejores sin ser perfectos, y sobre
todo, la disposición para hacer el bien
y combatir la injusticia donde
quiera que esté.

MIGUEL DE CERVANTES, Don Quijote de la Mancha

Para vos, mami ...

Acknowledgements

Es muy bueno poder contar con un espacio para agradecer a aquellas personas que han tenido relación con el desarrollo de este trabajo, en distinta forma, aunque sé al comenzar que seguramente alguien quedará sin su justa mención. En primer lugar, quisiera agradecer al Sr. Assensi Oliva, por brindarme la oportunidad de desarrollar un trabajo de tesis doctoral en su Laboratorio. También quiero agradecer a todos los compañeros y compañeras por todas las vivencias que hemos pasado, durante tantos largos años. Especialmente quiero agradecer a mis compañeras y amigas, Conxita y Ivette, por todas las situaciones que hemos enfrentado juntas, algunas positivas y otras no tanto, pero que nos han hecho crecer y sentirnos casi hermanas...de ambas he aprendido muchas cosas y os agradezco sinceramente vuestro apoyo y amistad... A todos mis compañeros de sala, Julián, Sergio, Stoyan y Luis, por ser compañeros encantadores. Especialmente quiero agradecer a Stoyan y a su familia, por las comidas tan buenas que prepara Gaby y por querer compartirlas con nosotros... Agradezco a Dani, por todos los marrones informáticos que siempre resuelve, y siempre poniendo la mejor voluntad, a Manolo por toda su ayuda en los montajes experimentales y su entusiasmo por hacer cosas bien hechas. También quiero agradecer la amistad de Gemma, Clara y Ramiro, por todas las excursiones compartidas y las comidas buenas que han hecho muy cortos los fines de semana... Especialmente también quiero agradecer a Dámaris, Paco, Pau y Rupa, por la amistad que nos brindan, y también por compartir con nosotros estos tiempos de tesis, a veces un poco duros... A Ale, Fernando, Omar y Mónika, por los asados argentinos (y polacos) compartidos..., me siento muy orgullosa de tenerlos como amigos. Especialmente quiero agradecer a Omar Salomón por ayudarnos tanto en los primeros tiempos, siempre será para nosotros el 'tío Omar'. Un especial recuerdo para Miquel, por sus aportes para el desarrollo de la tesis, pero sobretodo y más importante, por su amistad, por todas las discusiones que hemos tenido tan constructivas para mí, y lo bien que nos lo pasábamos... También quiero agradecer a todas mis familias, a mamá le agradezco su eterna confianza en mí, a mis hermanos, Lucio, Victoria y Ayelén, por enfrentar tantas circunstancias y mantenerse unidos, los quiero un montón...; a mi otra familia, papá, Susy, Facundo y Ale, por su apoyo constante, por su amor incondicional, por sentirlos siempre cerca aunque estemos lejos; y finalmente a mi otra familia, Rosa, Adolfo, Alberto, Marina y todos los chicos, Germi, Vicky, Chuchi y Agu, por todas las circunstancias que ya hemos vivido juntos...y todas las que nos quedan... También agradezco a Lili, por su gran amistad, y todas las veces que me ha ayudado a solucionar cosas desde Argentina, gracias, Lili, espero ansiosa el momento en que nos tomemos unas cervezas junto con Hernán para festejarlo... A mis abuelos, Matilde y Saturnino, porque son los que me han formado persona, siempre los tengo presentes, y este trabajo te lo dedico a vos, mami, porque siempre

mereciste más... Dejo para el final, las personas que más han soportado durante estos años, las que dan sentido a todos los esfuerzos, Melisa y Gusti, los amo profundamente..., y mi eterno amigo, compañero y amante, Gustavo, siempre ha sido para mí una referencia y una fuente de inspiración, siempre entusiasta, siempre interesado por lo que le explicas, me siento muy afortunada de tenerlo a mi lado, por eso no puedo dejar de decirle desde este lugar, gracias, ...

Contents

Abstract

A significant proportion of the total national energy budget of european countries is spent in buildings, therefore the efforts addressed to optimize building's thermal behaviour are of vital importance. In this sense, facades play a fundamental role. They act not only as barriers between external and internal conditions, but they can also help to reduce the consumption of energy for heating, ventilation and air conditioning. Moreover, they can help to produce healthy and comfortable indoor conditions.

The use of large, transparent areas in facades is a common current practice. Despite the architectural interest of these glazed areas, in Mediterranean climatic conditions they are responsible for building overheating. In these zones, double-skin envelopes made up of two layers of glass separated by an air channel -to collect or evacuate the solar energy absorbed by the facade- are considered to be a design option that could resolve this issue. In other climatic conditions, large heat losses may constitute the most determinant factor.

The objectives of this thesis are to give a step forward in the study and numerical analysis of passive systems in general, and advanced facades in particular. A transient code for the simulation of double and single skin facades including advanced technological elements, like phase change materials, transparent insulation and facade integrated collectors-accumulators has been developed. The features of the physic and mathematical models implemented are described. Instantaneous or integrated performance parameters describing thermal behaviour of the facades are defined. The numerical models implemented within the numerical tool have been submitted to a validation process in different forms: by comparing the numerical results with those obtained for simplified situations with analytical solutions, with tabulated global performance coefficients of simple facade configurations and with the results of other building simulation codes. Experimental research has been carried out in test cells situated at different geographical locations, thus they were subject to different climatic conditions. The main objective of the numerical code developed is to simulate advanced facades in order to assess the long term performance, and to account with a virtual tool to test passive designs, including challenging innovations. The applications of the numerical tool described in this thesis, for the optimisation of facades of real buildings are presented. As future actions, the link of the one-dimensional simulations produced by this numerical tool with a multi-dimensional simulation of specific zones of the facades is foreseen.

Preface

This work has been structured in six chapters. The first of them, introduces the concept of advanced facades in general, and double skin facades in particular. A classification of the envelopes is presented and the main advantages and disadvantages of these designs are outlined. Furthermore, the research focus of this work and the general objectives are detailed.

The second chapter introduces the main mathematical models implemented within the numerical code, the global calculation algorithm and the definition of parameters to describe global performance of facades.

Chapter 3 is devoted to the description of the verification and validation process carried out to get confidence in the numerical tool.

Chapter 4 is dedicated to a deep analysis of different facade designs, implemented as double and single skin. A parametric analysis is presented, whose objective is to describe the effects that different variables may present on the long-term performance of the envelopes.

Chapter 5 describes some applications of numerical simulation, carried out within the development of this thesis, to optimize facades of real buildings built in our surroundings.

Finally, chapter 6 outlines the general conclusions and describes further research that will continue after this work.

Chapter 1

Introduction

1.1 Overview of passive solar design

Buildings sector represents 40% of energy consumption within Europe, and it is expected that this trend will continue to grew. Energy consumption in buildings is dedicated to the following items: i)Space heating, ii)Cooling, iii) Domestic hot water, iv) Lighting and v) Ventilation.

Therefore, continuous effort is being carried out in order to get optimized thermal systems in buildings and to implement design measures favourable to energy savings. Passive design may have incidence in all the aforementioned aspects [1]. It involves design criteria, the use of advanced materials, the implementation of passive systems in building's envelope and active solar systems to help to meet energy demands.

In order to reduce heating and/or cooling loads, the envelopes of the buildings play an important role. Envelopes not only must fulfill architectural qualitative requirements (integrability, aesthetics, global image of a building, acceptance of users), but all these aspects must be combined with an optimum thermal performance.

From an energetic point of view, the most important items to take into account in a facade design are the following:

- Solar gains control
- Thermal losses control
- Thermal energy storage
- Integration with HVAC system of the building.

The main strategies to control solar gains, are the use of advanced materials (like coated glasses, serigraphy in glasses, the so called smart glasses and transparent insulation), overhangs, curtains, blinds, vegetation as curtains and as landscape modi-

Figure 1.1: Stadparkasse building. savings bank located in Dresden, Germany. The colour of individual windows can be controlled, or the total glazing in a building can be simultaneously altered by connecting it to the building's electrical management system. This system can save up to half the energy required for air conditioning in a building. (www.glass-resource.com/sneakpeek/sample4.htm)

fiers to project shadows over building surface and the removal of excedent energy by means of -for instance- the air movement in facade channel (in a double skin facade).

A smart glass, is intended to have the ability to control the amount of heat (and light), passing through [2]. The glass can change from transparent to completely opaque according to the user desire. Unlike blinds, smart windows are capable of partially blocking light while maintaining a clear view of what lies behind the window. There are different methods and properties for blocking light, such as: liquid-crystal, electrochromic and suspended-particle-device (SPD). Examples are exposed in Figure 1.1 and 1.2.

(a) (b)

Figure 1.2: Example of a smart glass partitioning: Levob Verzekeringen B.V. Leusden, The Netherlands (www.sggpivalite.com) a)Off b)On

Glasses also offer the possibility of controlling solar gains by means of the use of serigraphies, this technology allows at the same time the incorporation of a company figure or geometrical distinctive design.

The thermal losses are controlled by means of the application of thermal insulation [3], [4], which may include the use of transparent insulation [5], other factors which contribute to reduce thermal losses are the use of low thermal emissivity coating in glasses and the reduction of thermal convective losses by means of convenient vegetation which may disminish wind effects over facade surface [6].

The control of solar gains and thermal heat losses, is also related with the accumulation effects within the facade. A conveniently thick wall reduces heat losses and increments the performance of the envelope. Sensible storage is a common practice in passive design, but also latent storage is currently a design option with the utilization of phase change materials, as will be described later in chapters 2 and 4.

Sensible storage may contribute to reduce heating load in building, with water-filled solar collectors integrated in facade surface [7], [8]. Stored energy may be also used to provide domestic hot water.

1.2 Double skin facades

Double skin facades, which are nowadays an usual practice in singular buildings, (i.e: Agbar Tower in Barcelona and the new building of Caixa Terrassa, to mention some recent projects, developed in our surrounding area) may be considered advanced facades. This is due to the fact that they combine a high transparency (in facades made completely of external glass), with partial opaque internal areas, and an air channel. The air channel in these facades is used to take profit or to evacuate the solar heat gains from the facade. Several definitions of a double skin facade system have been formulated, all of them have in common the presence of two glass skins and an air cavity. Some authors remark the insulating features of the external glasses and air cavity [9], the applicability of this technology to refurbish old buildings , with the external glass skin located in front of the actual building facade [10], the ability of acoustic insulation [11], combined with the practicability of the inner glass window and the possibilities of sun shading located in the intermediate cavity [11], [10].

The thickness of the air channel may vary from 20 cm until 2 meters. The air channel of double skin facades allows to use different strategies to regulate the performance of the envelope:

- The inlet air can be from the building indoors or outdoors.
- The destination of the outlet air can be towards outdoors or indoors, or integrating the HVAC system of the building.

- In relation with the flux type within the channel:
  -Forced convection
  -Natural convection, with the channel opened or closed.
- In relation with the constructive solution: one channel by storey level or one channel with the total height of the facade, or divided in boxes with no connection between them.

Double skin facades allow also the possibility of using shadowing elements like roller curtains or blinds in the air cavity.

1.3 Classification of double skin facades

Double skin facades may be classified in several manners, according to the type of construction, the type of airflow in cavity, the origin and destination of air flow of the cavity (as commented in previous section), the tightness of both skins, the materials used, etc.

According to the tightness of both skins, they may be:

- With sealed inner and outer skin
- Operable inner and outer skin
- Airtight internal skin
- Airtight external skin
- Louver facades, as for instance the new *Agbar Tower* building at Barcelona.

According to the channel height, as mentioned by Poirazis [12], some authors classifies double skin facades in [10]:

- Building high double skin facade: the air channel has the total height of the building.
- Storey-high double skin facade: the air channel is divided in air cavities with the height of each storey.

This classification is also related with the geometry of the cavity, more precisely with the geometrical partitions air cavity may present [4], [13], [14]. All these authors agree in the following classification with little differences among them.

- Multi storey double skin facade or curtain wall

- Corridor facade
- Box window facade
- Shaft box type
- Facade with horizontal and vertical ventilation

An additional classification includes the following variants:

- Modular hybrid facade.
- Hybrid facades integrating solar collectors

Each one of these implementations will be explained in the following paragraphs.

1.3.1 Multi storey double skin facade or curtain wall

The air cavity has no separations at each storey, but it extends over the total height of the building. Air enters through the bottom zone of the cavity and it is warmed within the cavity due to solar radiation, air movement into the channel is produced by natural convection, although forced convection is also possible. Hot air outgoing through the upper zone is replaced by fresh air at bottom. Figure 1.3 shows a scheme and an example of this kind of implementation.

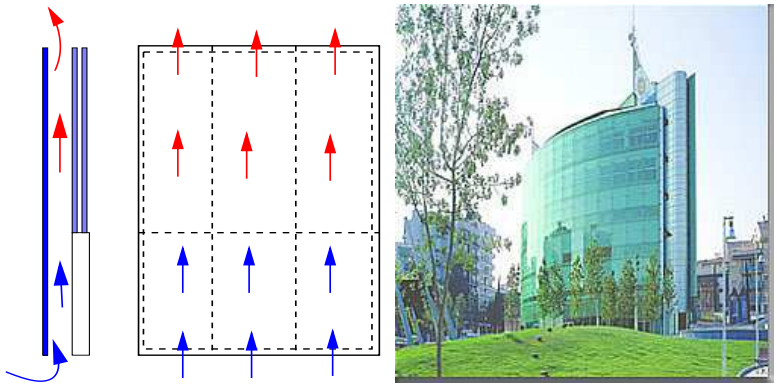

(a) (b)

Figure 1.3: Multi-storey double skin facade a)Schematic working conditions, b)Example: Caixa Terrassa headquarters office building

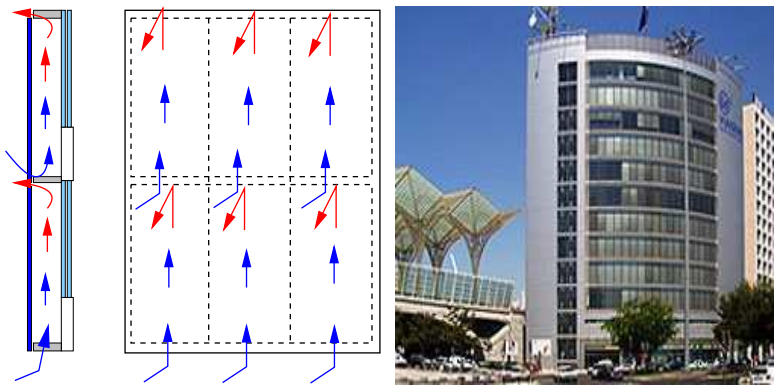

(a) (b)

Figure 1.4: Corridor facade a)Schematic working conditions, b)Example: Portugal Telecom Expo 98 Building, it has a facade partitioned per storey (corridor facade) 11.5m width, 43.72m height

1.3.2 Corridor facade

In this case, the cavity has horizontal partitions, realized by acoustic, fire, security or ventilation reasons. Air movement is due to natural convection. Figure 1.4 shows as implementation of this facade.

1.3.3 Box window facade

The air cavity has horizontal partitions at each floor and vertical partitions on each window, in a manner that smaller and independent boxes are created. The inlet and outlet vents are placed at each level. Some authors, as Zollner in [13], describe a variant of this type, in which a diagonal air streaming is produced. Air inlets and outlets are located in cross form. Air enters from input of bottom box and it is extracted through the neighbouring top box. In this form, it is possible to avoid the re-infiltrations of air from the outlet of a zone to the inlet of the inmediate top zone. This configuration also prevents fire spreading [12]. Figure 1.5 shows an scheme of the working conditions of this facade.

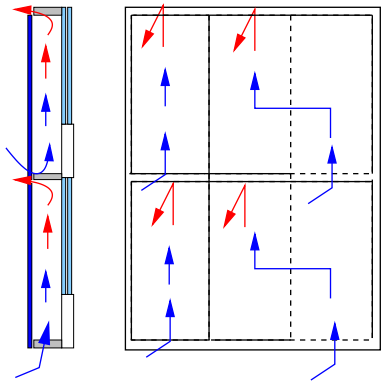

Figure 1.5: Box window facade, schematic working conditions

1.3.4 Shaft box type

In this case, the facade is a combination of a multi-storey cavity (shaft zone) with box window facades. At both sides of the central shaft, the box window areas discharge air into the central zone, where it is warmed and due to stack effect it raises and is exhausted through the top level of shaft. The large stack effect of central shaft improves the ventilation at the box windows. During winter, central shaft cavity may be closed, and box windows may work driving warm air to inside room. In summertime, it is possible to use forced convection only in the central shaft, in this form a good ventilation of the whole facade is possible. An example is shown in Figure 1.6.

1.3.5 Facade with horizontal and vertical ventilation

This case is similar to corridor facades, but in this implementation, also vertical flow between different storeys is possible, since horizontal partitions in the cavity allow the flow to pass. Along the total height of the building, vertical fans are installed to produce the horizontal movement of air, thus horizontal forced convection is combined with natural convection vertical flow. This implementation allows a homogenous distribution of temperatures during winter, even in north oriented facades. In summer, the cooler air from north facade is used to refresh the south facades.

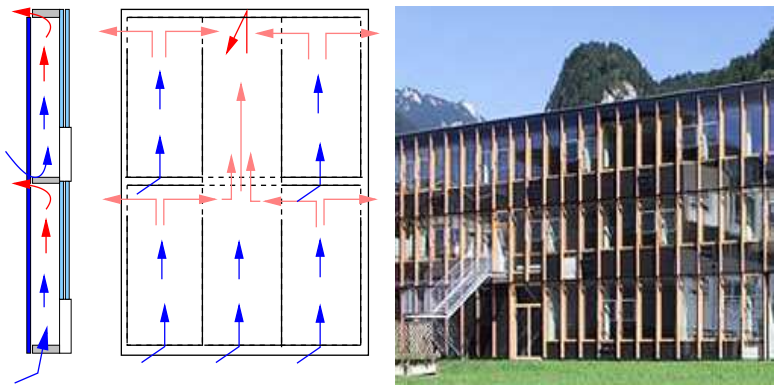

(a) (b)

Figure 1.6: Shaft box facade a)Schematic working conditions, b) Example: Academy of Applied Sciences, (Kufstein, Austria), width x height= 39.7x 11m

Figure 1.7: Facade with horizontal and vertical ventilation, Gotz headquarters, Wurzburg, Germany. Fans in the corners of the cavity switch on to redistribute the warm air from the sunny to shaded faces of the building.

An additional classification, is the:

1.3.6 Modular hybrid facade

This implementation according to author description, is constituted by four box-windows, with seasonal differentiated configuration [13]. In Wintertime, two vertical adjacent boxes form the so-called 'admission module', external air enters in

the box window through little fans, it is warmed and sent to the inside room. The adjacent two vertical boxes form the 'discharge module', the internal air is removed through the box window and sent outside. These two air flows may be used in a heat exchanger to preheat air before entering it to building. During summertime, boxes are covered by curtains, and two air currents are produced in the cavity. A bottom to top flow is produced behind curtains with cool air proceeding from the room. Other flow is produced between curtain and external glazing with air proceeding from outside and extracted at each level. These flows allow to keep temperatures inside channel and curtains at a low level.

1.3.7 Hybrid facades integrating solar collectors

The denomination of hybrid facades has been also used by other authors [15], [16] to denominate passive facades which integrate solar collectors. These facade-collectors are used to warm water which circulates through ducts in the absorber surface. This hot water is used to reduce the heating load of the building or for domestic hot water purposes. This thesis will focus on hybrid facades formed by collectors with water accumulators integrated in the same envelope, in a single or a double skin facade. These implementations will be described in Chapter 4.

1.4 Single and double skin green facades

This general denomination has been used to refer to passive ecologic designs, including different strategies to get improved thermal behaviour (painting, orientation, scarce impact on ecosystem) and moreover, the designs whose production stage was carefully carried out to encourage the use of recycling materials. This name refers also to facades designs which integrate deciduous vegetation [6] as shadowing element to produce an improved behaviour of the whole building. Vegetation may be attached to external envelope in single skin facades, or in double skin facades. In this case, vegetation may grow at the air cavity. One example of the use of vegetation as natural shadow projector is shown in Figures 1.8(a) and 1.8(b).

(a) (b)

Figure 1.8: Examples of the implementation of a green curtain in a single skin facade. Deciduous vegetation allows to improve solar control during summer months, with scarce influence during winter period. The vegetation curtain also presents an additional design factor as the use of the variable leaves colours in different stages of the year.

1.5 Advantages and disadvantages of double skin facades

1.5.1 Advantages

The main advantages that double skin facades offer in comparison to single skin ones, may be summarized as:

- Improved acoustic insulation. According to some authors [10], [13], [14], , this is the most remarkable property of double skin facades which has decided owners and architects to carry out this kind of constructions. Level of noise insulation depends on the openings in external skin, and the type of double skin facade practiced.
- Possibility of natural ventilation of the building using the stack effect of cavity to renovate internal air. On the other hand, this implementation makes possible the aperture of indoor windows even in high buildings, due to the reduction of the wind pressure achieved by the additional skin.

- Improved thermal insulation, thus lower heating load. The attachment of an additional skin plus the air cavity with natural convection produces a reduction of heat losses (improved U value of the facade).

  During summertime, forced ventilation in air cavity assures a large ventilation of the whole facade, when natural ventilation is desired, it is of high importance the position and materials of shading.

- Possibility of night time ventilation.

- Possibility of positioning solar control and lighting devices in cavity (they are best protected against wind and rain, with less maintenance and cleaning demands).

- Reduction of cooling load.

- Possibility of applying cross ventilation (for instance, from north facades).

- Possibility of heat recovery.

- Less working hours of HVAC system.

- Architectural attractive design and reduced environmental impacts.

- High degree of natural lighting, which improves internal comfort.

- Reduction of temperature difference between the internal surface of the facade and indoor air, improving the thermal comfort.

1.5.2 Disadvantages

Double skin facades also have some disadvantages, which may be summarized as follows:

- Necessity of a careful design of the ventilation cavity to avoid overheating problems, since air temperature may be very high.

- Additional operational costs. Cleaning in the cavity, filters, joints, openings and maintenance tasks cause an increment of operational costs ([14]).

- Higher construction costs. The existence of an additional glass skin, usually with special glass features makes these facades more expensive than the single skin ones.

- Reduction of inhabited space. Air cavity deep is settled from 0.1 to two meters, this space represents a reduction of the available useful area. However, this effect has its counterpart in the increment of internal areas with improved comfort conditions: double skin allows the utilization of the areas adjacent to the facade since temperatures are closer to ambient temperatures.
- Glare effects of increased glass areas.

1.6 Research focus on double skin facades

Double skin facades need an intensive research of heat transfer and fluid flow to make them optimal for different climatic conditions and geometrical implementations. Accumulation effects are important in facades including thick walls or water accumulators, it makes necessary to analyse envelopes in a transient mode.

The research on envelopes passive implementations requires the long term performance assessment of the following principles:

- Utilization of improved glasses, with special coatings with incidence in optical and thermal properties (improved solar heat gain coefficient and global heat transfer coefficient).
- Reduction of heat gains in warmer climates, in order to reduce cooling load of the building.
- Reduction of heat losses in cold climates, taking maximum profit of solar absorbed energy to reduce heating requirements.
- Thermal storage in facade. Sensible storage in thick conventional walls, liquid-based accumulators integrated in the facade, latent storage in walls including phase change materials.
- Shading devices, such as blinds, overhangs, or green louvers (vegetation integrated to the facade).
- Integration of passive implementations with the heating, ventilation and air-conditioning system of the building.

To make it possible, it is necessary to develope accurate models to describe all the complex heat transfer phenomena produced in an envelope and the internal building. These models must use heat transfer coefficients in order to reduce the multi-dimensional transient nature of the problem to an affordable transient one-dimensional numerical approach. A validation process is necessary to detect bugs

in the numerical code and get confidence in numerical results. Once validated, a numerical code represents an useful tool to optimize different envelope designs, becoming a testing bank of virtual prototypes.

1.7 Objectives of this work

The objectives of this thesis are to give a step forward in the study and numerical analysis of passive systems in general, and advanced facades in particular. This thesis began with a first version of a specific numerical simulation code to simulate double skin facades ($AGLA$ code). During several years, (continuing currently) this code was augmented and validated in several forms, which will be detailed in following chapters. This work has been done in the framework of two european projects: MFVF [17] and ASFIC [18], and several spanish projects at different levels. The work developed within this thesis has been focused on:

- Contribute to increment implemented models in $AGLA$ code.
- Validate the implemented models individually and as a whole, by comparison with analytical solutions, with wide-accepted scientific published data, and with experimental data obtained in the framework of different projects.
- Colaborate with the experimental infraestructure developed within the *Centre Tecnològic de Transferència de Calor* (CTTC) to validate the numerical results.
- Contribute to the numerical study of the performance of double and single skin facades, by means of parametric analysis (influence of channel width, flow regime, climate, materials in the facade, etc).
- Contribute to develop parameters to characterize long-term thermal performance of advanced facades.

References

[1] J. D. Balcomb, R. Jones, C. Kosiewicz, G. Lazarus, R. McFarland, W. Wray, S. C. Kaushik, and M. A. S. Malik. *Passive Solar Design Handbook*. American Solar Energy Society, Inc., 1983.

[2] M. Fischetti. Vidrio Inteligente, discreto y fresco. Investigación y Ciencia., 2006.

[3] B. Todorovic and B. Maric. The influence of double facades on building heat losses and cooling loads. Faculty of Mechanical Engineering, Belgrade University. Technical Report. 2002.

[4] D. Saelens and H. Hens. International Energy Agency. Exco Energy Conservation in Buildings and Community Systems Programme. Copenhaguen meeting, 15-17 April 1998. Annex 32, Subtask B: U- Value and Solar Heat Gain Coefficient Performance, 1998.

[5] D. Faggembauu, A Oliva, and M. Soria. Analysis of transient effects on the performance of advanced double and single skin facades including transparent insulation. Numerical study and experimental validation. In *Proceedings of the 6th ISES Europe Solar Conference (EUROSUN 2006)*, 2006.

[6] M. Soria and A. Oliva. Vegetation for Cooling advanced glazed facades: Arquitectural integration, Gardening Technology, Numerical Simulation. GREENFACADE project: Publishable Final Report. Technical report, 2004.

[7] I. Industry Workshop. IEA-SHC Task 26. Bergmann. Facade Integrated Collectors. Constructions, building physics and the results of two monitored systems. Technical report, Arbetisgemeinschaft Erneuerbare Energie. Institute for Sustainable Technologies., 2002.

[8] C. Dharuman, J. H. Arakeri, and K. Srinivasan. Performance evaluation of an integrated solar water heater as an option for building energy conservation. *Energy and Buildings*, 38:214–219, 2006.

[9] T.M. Boake. The Tectonics of the Double Skin: North American Case Studies. University of Waterloo. Technical Report. 2006.

[10] A. Compagno. *Intelligent Glass Facades*. Birkhäuser Berlin, 1995.

[11] E.Lee, S.Selkowitz, V. Bazjanac, V. Inkarojrit and C. Kohler. High-Performance Commercial Building Façades. Building Technologies Programm, Environmental Energy Technologies Division, Ernest Orlando Lawrence Berkeley National Laboratory. (LBNL), University of California, Berkeley, USA.2002.

[12] H. Poirazis. Double Skin Façades for Office Buildings. Report EBD-R-04/3. Technical report, Division of Energy and Building Design. Lund University, 2004.

[13] A. Zöllner. *Experimentelle und theoretische Untersuchung des kombinierten Wärmetransports in Doppelfassaden*. PhD thesis, Technischen Universität München, 2001.

[14] E. Oesterle. *Double Skin Facades: Integrated Planning*. Prestel Publishing, 2001.

[15] G. Rockendorf, S. Janssen, and H. Felten. Transparently insulated hybrid wall. *Solar Energy*, 58(1-3):33–38, 1996.

[16] B. Bartelsen S. Janssen, G. Rockendorf. Gebäude-integration von Sonnenkollektoren mit Flüssigkeits-kühlung. Technical report, Institut für Solarenergieforschung GmbH Hammeln/Emmerthal, 1998.

[17] M. Costa, A. Oliva, M. Soria, and D. Faggembauu. Multi-Functional Ventilated Facades (MFVF). Publishable Final Report. Technical report, 2000.

[18] D. Faggembauu, M. Costa, and A. Oliva. Advanced Solar Facades with Integrated Collectors-accumulators for domestic hot water and space heating applications (ASFIC). Publishable Final Report. Technical report, 2003.

Chapter 2

Development of a numerical model to simulate advanced facades

2.1 Previous works and motivation

Numerous works have analysed the thermal behaviour of dwellings in order to reduce the energy consumption that stems from the necessity for air-conditioning and space heating in buildings. The practice of implementing building designs conceived to take the maximum profit of natural forces in order to reduce energy consumption, is known as passive solar design. The main available resource is the solar energy, but also wind forces, vegetation, shadows, and the global landscape are taken into account. This practice in new and retrofitted buildings to reduce cooling and heating demands is slowly spreading. Passive systems must combine attractive architectonic designs with improved thermal comfort conditions. The double skin facades, also known as Double Skin Curtain Wall, Multiple Skin Facade or Dynamic Facade, were reported since 1840, according to [1]. Some authors mention the first instance of a double skin curtain wall to appear in 1903, in the *Steiff Factory in Giengen, Germany* [2], where the priorities were to maximize daylighting while taking into account the cold weather and strong winds of the region. More recently, the possibilities of using windows to preheat air before introducing it into buildings have been studied in order to achieve a ventilation with a lower heating load [3]. Efforts have been made to improve passive solar heated buildings by improving the design of the storage wall. For instance, a wall with multiple inlets and outlets with a higher efficiency than a traditional Trombe wall has been analysed [4]. Other studies have focused on thermosyphon air panels [5], TIM-PCM applications [6], ventilated facade panels implemented like a composite Trombe wall [7] and multifunctional solar facades for

daylight and electricity production [8]. Results obtained with multi-functional ventilated facades addressed to three different climatic conditions have been reported [9].

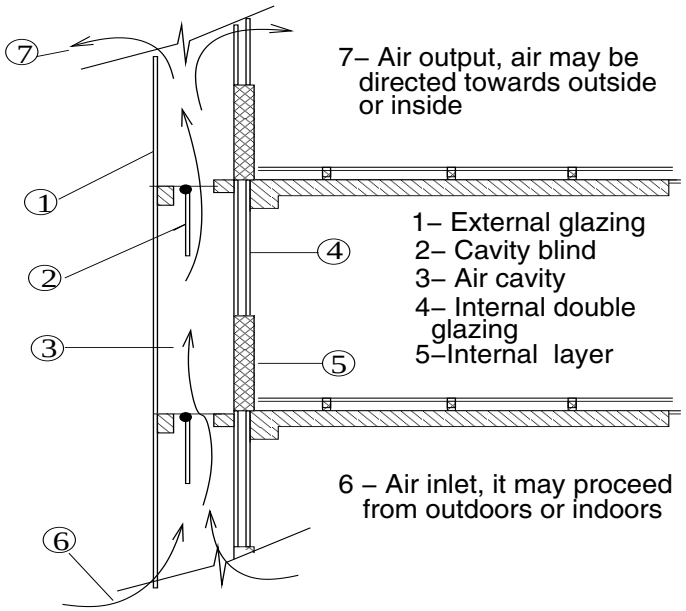

Figure 2.1: Scheme of a double skin facade formed by an external glass layer and an internal layer with a transparent and an opaque zone. Air in the cavity may proceed from outside or inside, it may be directed towards the internal room or the external side of the facade.

However, little information is available on the behaviour of ventilated glazed facades in Mediterranean climates (moderate winters, hot summers). At the same time, it has been an important increase in the number of glazed facades applied to commercial and singular buildings in this type of climate.

Numerical simulation is a powerful tool to test passive designs, this has motivated the development of numerical codes for the simulation of a single ventilated facade [10] or Trombe wall [11] during approximate time intervals of one day. By means of a two or three-dimensional discretization of the facade, CFD techniques allow the determination of detailed temperature, velocity and pressure maps with little empirical information. However, this thesis will focus on a numerical code designed for the transient simulation of all the facades (ventilated or conventional) of

a building over long time intervals (typically, one year). Therefore, to reduce the CPU time to a reasonable level, one-dimensional discretizations of the air channel are used. The scarce experience about the performance of these facades in these climatic conditions, and the no-existence of specific tools for the simulation of these systems have encouraged the development of the present work.

2.2 General description of the problem

Ventilated glazed facades are formed by two layers of different materials, opaque or transparent, that are separated by an air channel, used to collect or evacuate the solar radiation that is absorbed by the facade (Figure 2.1). This two-layer disposition provides large flexibility, that can be used to adapt the designs to different requirements while keeping (if desired) a uniform outdoor aspect.

For architectonic reasons, the outer layer is usually made entirely of glass, while the indoor layer may be partially opaque. This allows direct solar gains to be reduced and increases the thermal inertia of the building. However, external layer may be also constituted by transparent insulation, and the internal layer may be totally glazed, or include a storage phase change material wall layer. In this chapter, a presentation of the numerical code developed within this thesis, so called $AGLA$ (for *Advanced GLAzed facades simulation*) will be carried out. The objective of the numerical tool is to allow the dynamic simulation of ventilated double and single skin facades. It is based on time-accurate, one-dimensional discretizations for the channel and the different zones, and allows heat fluxes and temperature distributions in the facade to be obtained over the course of one year. The numerical code allows advanced elements to be integrated into the facade, such as phase change materials, selective surfaces and improved glasses.

The discrete equations are obtained from the continuous governing equations using the finite-volume method [12]. The building skin is assumed to be divided into a number of independent *facades*, and each facade is in turn divided into a number of *zones*, which are only coupled due to the presence of the air channel. One-dimensional discretizations are used for the air-channel and for each of the zones (orthogonally to the facade). This approach, that is between a one-dimensional and a two-dimensional model, has proved to be a good compromise between accuracy (compared with the experimental results) and computing time.

In the following paragraphs the models implemented will be described.

2.3 Outdoor conditions

Although the code can use transient data measured outdoors if they are available, it is usually of interest to work with a reduced set of monthly-averaged measurements and to generate transient outdoor boundary conditions from them. The typical weather data introduced in the code are:

- Monthly-averaged daily integrated values of global horizontal solar radiation,
- Maximum and minimum temperatures,
- Wind velocity,
- Wind direction and
- Relative humidity.

The diffuse component of the global solar radiation is obtained using Collares-Pereira-Rabl correlations [13]. The same correlations are used to calculate instantaneous values of diffuse, beam and total radiation. Values on arbitrary sloped surfaces are obtained from a Liu and Jordan isotropic diffuse model [14]. For ambient temperatures, a sinus distribution is assumed to exist between its maximum and minimum values. Outdoor thermal radiation considers the radiation interchange between the facade and two bodies: a fictitious black surface at the so-called sky temperature, calculated with Berdahl and Martin's expression [15] and another surface, the ground, which is considered to have a given thermal emissivity. A view factor between the facade and the ground is introduced. To calculate the ground temperature, the ground is assumed to be adiabatic and to have a given solar reflectivity. The convective heat transfer coefficient is calculated as a function of the wind velocity [15]. Outdoor convective heat transfer coefficients are calculated from empirical expressions [16], taking into account wind direction and wind velocity, for leeward and windward surfaces.

2.4 Indoor conditions

Regarding the indoor conditions, it is assumed that a single constant indoor air and walls temperature exists to evaluate the convective and radiative heat transfers respectively. Indoor convective heat transfer coefficients are calculated considering natural convection [17].

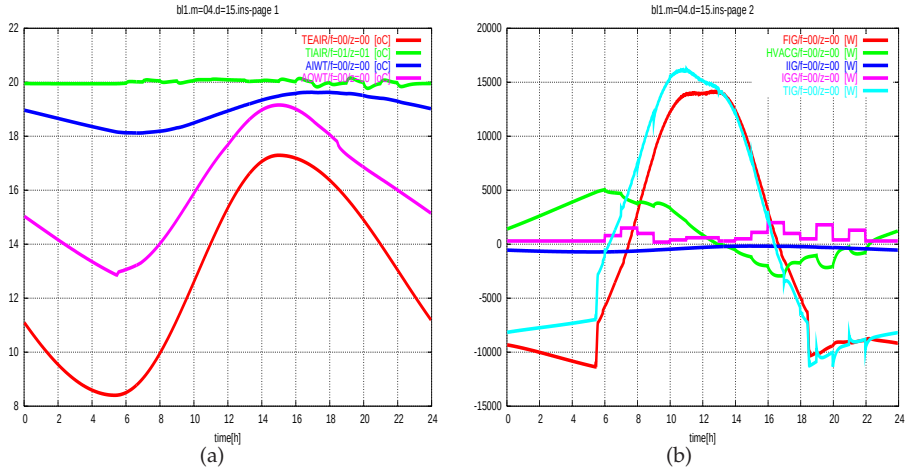

(a) (b)

Figure 2.2: Instantaneous temperatures and heat fluxes calculated from the imposed internal and external conditions. a) TEAIR: external air temperature, TIAIR: internal air temperature, AIWT: internal wall surface temperature, AOWT: external wall surface temperature; b) Heat fluxes: FIG: internal gains through the facade, HVACG: heating, ventilation and air-conditioning demand, IIG: internal infiltration gains, IGG: internal generated gains, TIG: total internal gains.

Indoor air temperature, may be imposed as a constant value, or it may be calculated as a result of a heat balance, among the heat gains through the facade, the internal generated gains (imposed as a time dependent data), the internal energy provided or extracted by the heating/cooling system and the imposed air renovation rate. The difference between the resulting internal temperature and the indoor set temperature will determine the heating/cooling requirements. When indoor air temperature is imposed as a constant value, it is equivalent to assume that a perfect controlled HVAC equipment is able to keep this temperature in any condition. More details are described in [18].

Figure 2.2(a) shows an example of daily external and internal air temperatures, together with wall surface calculated temperatures, for an april day. Figure 2.2(b) shows the daily heat fluxes which take place in the internal heat balance.

2.5 Glazed areas

A global model was developed to solve heat transfer through a system formed by any number of semi-transparent layers. The heat transfer mechanisms involved in the model are as follows: heat conduction within each glass layer, natural convection between glass layers, natural or forced convection with the air of the channel, thermal radiation between glass layers and solar radiation absorption and transmission. Optical properties are considered independent of direction (diffuse) and wavelength (grey).

2.5.1 Conduction in each glass layer

The one-dimensional expression of energy conservation equation, with an additional source term to include solar absorption, is solved to calculate heat conduction through the glasses layers (equation 2.1).

$$\frac{\partial T}{\partial t} = \frac{k}{\rho c_p}\frac{\partial^2 T}{\partial x^2} + Q \tag{2.1}$$

For each glass layer, the source term includes solar absorption:

$$Q[i] = IA[i] \tag{2.2}$$

Solar absorption in each layer is calculated using equation 2.7.

2.5.2 Natural convection between glass layers

This phenomena is governed by Navier-Stokes equations (expressions 2.65, 2.66, 2.67 and 2.71). However, in this case, a simplified model is applied, which makes use of heat transfer convective coefficients for natural convection between glass layers determined from empirical expressions of the Nusselt number between two parallel vertical plaques [19].

2.5.3 Thermal radiation between glass layers

The thermal radiation, q_{rt} between glass layers is determined by solving for the net heat transfer between two infinite opaque parallel plates:

$$q_{rt} = \frac{\epsilon_i \;\; \epsilon_{i+1} \;\; \sigma(T_i^4 - T_{i+1}^4)}{\epsilon_{i+1} + \epsilon_i(1 - \epsilon_{i+1})} \tag{2.3}$$

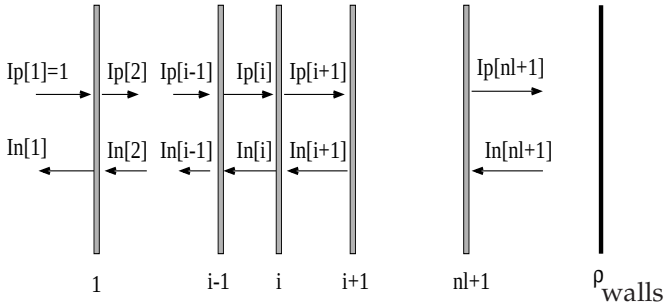

Figure 2.3: Schematic behaviour of a glazing system formed by nl+1 layers and an inner opaque surface of solar reflectivity ρ_{walls}, receiving energy from outdoor (left) surface. The space between the glass layers can be a closed air gap or the main air channel of the facade

2.5.4 Solar radiation

Solar irradiosity on the outdoor surface of a system of any number of glass layers from $i = 1$ to $i = nl + 1$, as schematically shown in Figure 2.3, is partially absorbed, reflected and transmitted by each one of the semi-transparent layers. These fractions are calculated by an iterative net heat radiation algorithm [20]. For each layer the values of reflectivity, absorptivity and transmissivity are known. Solar radiation is divided in two components: positive (I_p) and negative (I_n). The positive component for each layer is the fraction transmitted of the incident radiation plus the fraction reflected of the negative component of the opposite layer. The value of the first layer is known ($I_p[1]$). For layers 2 to nl+1, it is evaluated as:

$$I_p[i] = I_p[i-1]\tau[i-1] + I_n[i]\rho[i-1] \tag{2.4}$$

The negative component for the last glass layer is:

$$I_n[nl+1] = I_p[nl+1]\rho_{walls} \tag{2.5}$$

The rest of the negative components (from nl to 1) are computed as:

$$I_n[i] = I_n[i+1]\tau[i] + I_p[i]\rho[i] \tag{2.6}$$

It is assumed that the reflectivity is the same for both surfaces of each layer. For each layer, the absorptance is the difference between the energy that enters and the energy that emanates from the surface:

$$A[i] = (I_p[i] + I_n[i+1]) - (I_p[i+1] + I_n[i]) \tag{2.7}$$

Then, applying a reduced number of iterations, total absorptance, reflectance and transmittance factors are calculated as:

$$A_s = \sum_{i=1}^{i=nl} A[i] \tag{2.8}$$

$$R_s = I_n[1] \tag{2.9}$$

$$T_s = I_p[nl+1] - I_n[nl+1] \tag{2.10}$$

2.6 Transparent insulation materials in building facades

Transparent insulation materials (TIM) are a transparent cellular array made of glass or polycarbonate material, with a honeycomb arrangement between two bounding surfaces. They offer the advantage of allowing to combine a high degree of transparency (large solar gains) with a good degree of insulation (avoiding thermal losses).

These materials are being used nowadays for different applications mainly in central European climates, which are characterized by moderate summers and cold winters. They are applied in solar collectors [21], [22], greenhouses, skylights and building insulation. Numerous works have been published dealing with optical and thermal properties of plastic honeycomb-type structures [23], [24], and the implementation of combinations of TIM materials with glasses in advanced facades [25], [26]. Some authors [27] have carried out a review of solar TIM in terms of applications, fabrication procedures, availability and cost trends. Integrated collector-storage solar water systems efficiency can be improved by means of the placing of TIM between external glass and absorber surface [28], [29].

Heat is transferred through honeycomb layers in the forms of radiation and conduction. Natural convection is practically eliminated due to the small size of the cells. Transparent insulation materials can be used bounded by solid opaque plates, with an air gap between one bounding surface and the adjacent honeycomb face (known as compound honeycomb), with bounding surfaces partly transparent to long wave radiation (plastic sheets or glass layers) and with limiting surfaces with a low-emissivity coating in order to increase thermal insulation capacity. The air gap between honeycomb face and bounding surface in this last case has the function to uncouple radiative and conductive modes of heat transfer.

Models have been developed to calculate the overall conductance of compound honeycombs [30] applied to greenhouses [31]. According to these models honeycomb thermal conductance varies between 2.2 to 3.1 W/m^2K.

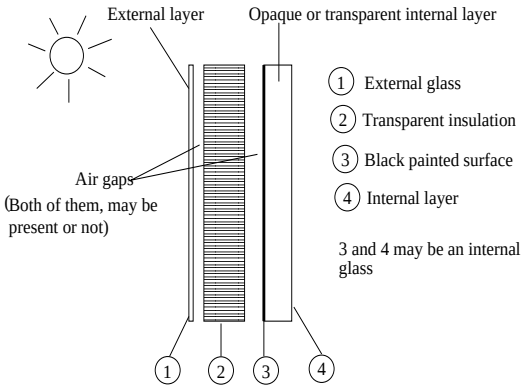

Figure 2.4: Geometric configuration of a facade including transparent insulation

2.6.1 General considerations about radiation heat transfer

Honeycomb-type structures within a facade are usually bounded by an external and internal surface made of glass. It is also a common practice to use TIM in combination with an opaque black-painted wall (see Figure 2.4), in order to increase the solar absorption of the whole facade, this surface is also combined with the use of selective coverings to reduce thermal emissivity, and therefore, long-wave radiation losses.

Honeycomb-type structures must be modelled as a medium that participates in radiation heat transfer, meaning that the medium emits, absorbs and scatters radiation. Moreover, this medium is linked with two surfaces which may reflect, absorb and transmit radiation. Within the medium, radiative heat transfer is described by the general radiative heat transfer (RTE) equation [32]:

$$\frac{dI_\eta}{ds} = \hat{s} \cdot \nabla I_\eta = \kappa_\eta I_{b\eta} - \beta_\eta I_\eta + \frac{\sigma_{s\eta}}{4\pi} \int_{4\pi} I_\eta(\hat{s_i}) \Phi_\eta(\hat{s_i}, \hat{s}) d\Omega_i \tag{2.11}$$

This equation is an energy balance on the radiative energy which travels in the direction $\vec{s}$ within a small pencil of rays (Figure 2.5). Intensity varies along this direction $\vec{s}$ due to contributions which produce an attenuation of radiation (absorption and out-scattering), and contributions which produce an augmentation of radiation (emission and in-scattering).

Absorption and out-scattering are quite similar phenomena, both are directly proportional to the distance (s) that the ray travels through the medium and to the incident energy (I). This proportionality is represented by a linear absorption

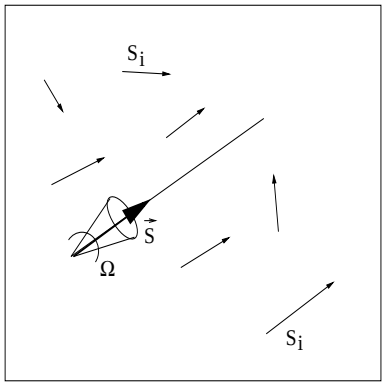

Figure 2.5: Scheme for energy balance equation. An intensity ray travels in the direction $\vec{s}$ within a small pencil of rays $d\Omega$ receiving contributions from other directions (emission and in-scattering) and suffering attenuations by absorption and scattering towards the other directions $\vec{s_i}$ (out-scattering)

coefficient(κ_η) and a scattering coefficient ($\sigma_{s\eta}$). The difference between both mechanisms is that absorption produces an augment of internal energy and out-scattering a re-distribution of energy which dissapears from the analyzed direction to appear in another.

Emitted intensity is proportional also to the length path and the local energy content in the medium, due to thermodynamic equilibrium it is proportional to blackbody intensity; in-scattering takes into account contributions from all the directions to the analyzed direction, so it must be calculated integrating over all solid angles.

The general radiative heat transfer equation (equation 2.11) establishes that the change in intensity is due to energy emission (first term of the last member) minus the extingued portion of energy (due to absorption and out-scattering), which are considered with the extinction coefficient (β_η), plus the in-scattering contribution. This last term is calculated from the phase function Φ_η which describes the probability that a ray from a direction $\vec{s_i}$ will be scattered into the direction $\vec{s}$, as extensively developed by Modest in [32].

All the magnitudes of equation 2.11 depend on the wavenumber (η) and space, moreover intensity and scattering depend on direction ($\vec{s}$ and $\vec{s_i}$). Time variation has been neglected since radiative intensity dependance on time (influenced by light speed) is negligible in this heat transfer application.

Equation 2.11 is a general energy balance, which is valid anywhere in an arbitrary enclosure, for each wavenumber or for a gray medium. Its solution is normally ob-

tained from the knowledge of the intensity for each direction at the enclosure boundary.

2.6.2 Radiative heat flux

If equation 2.11 is integrated over all solid angles, as shown in expression 2.12:

$$\int_{4\pi} \hat{s} \cdot \nabla I_\eta d\Omega = \int_{4\pi} \kappa_\eta I_{b_\eta} d\Omega - \int_{4\pi} \beta_\eta I_\eta(\hat{s}) d\Omega + \int_{4\pi} \frac{\sigma_{s\eta}}{4\pi} \int_{4\pi} I_\eta(\hat{s_i}) \Phi_\eta(\hat{s_i}, \hat{s}) d\Omega_i d\Omega \tag{2.12}$$

The left hand side is the spectral radiative heat flux while the right hand side may be arranged taking into account that $\int_{4\pi} \Phi_\eta(\hat{s_i}, \hat{s}) d\Omega = 4\pi$ and $\kappa_\eta = \beta_\eta - \sigma_{s\eta}$, resulting in:

$$\nabla \cdot \vec{q_{r_\eta}} = \kappa_\eta (4\pi I_{b\eta} - G_\eta) \tag{2.13}$$

Where:

$$G_\eta = \int_{4\pi} I_\eta \hat{s} d\Omega \tag{2.14}$$

is the incident spectral radiation.

The equation 2.13 expresses that the spectral net losses of radiative energy from a control volume is equal to emitted minus absorbed energy. No scattering appears since it only involves a redistribution of energy and it does not affect the energy content in the control volume. The integration of equation 2.13 over the complete spectrum allows to obtain the total heat flux:

$$\nabla \cdot \vec{q_r} = \kappa (4\sigma T^4 - G) \tag{2.15}$$

where G is the total incident radiation.

2.6.3 Numerical method

Equation 2.11 may be solved analitically in few limited, idealized and simplified cases. Therefore, several approximate methods have been developed to solve it numerically; among these methods, it may be mentioned, the discrete ordinates method (DOM), first proposed by Chandrasekhar [33] and extensively developed by Modest [32], which has been used to deal with heat transfer through transparent insulation used in facades. In this method the intensity is assumed to be constant over discrete parts of the total solid angle 4π. A set of n different directions $\hat{s_i}$; $i = 1, 2, ...n$, are chosen and the equation 2.11 is solved for each of these directions. As a result of the application of the method, the equation of transfer is transformed into a set of n

simultaneous partial differential equations. In these equations, the integrals over directions are replaced by sums for all the directions each one associated with a weight factor. The weight factors w_i are the quadrature weights associated with the directions $\hat{s_i}$, that is:

$$\int_{4\pi} f(\hat{s})d\Omega \simeq \sum_{i=1}^{n} w_i f(\hat{s_i}) \tag{2.16}$$

Therefore, equation 2.11 may be approximated by a set of n equations:

$$\vec{s_i} \cdot \nabla I(\vec{r}, \vec{s_i}) = \kappa(\vec{r}) I_b(\vec{r}) - \beta(\vec{r}) I(\vec{r}, \vec{s_i}) + \frac{\sigma_s(\vec{r})}{4\pi} \sum_{j=1}^{n} w_j I(\vec{r}, \vec{s_j}) \Phi(\vec{r}, \vec{s_i}, \vec{s_j}) \tag{2.17}$$

with $\quad i = 1, 2, ...n$

subject to boundary conditions:

$$I(\vec{r_w}, \hat{s_i}) = \epsilon(\vec{r_w}) I_b(\vec{r_w}) + \frac{\rho(\vec{r_w})}{\pi} \sum_{\hat{n} \cdot \hat{s_j} < 0} w_j I(\vec{r_w}, \hat{s_j}) \mid \hat{n} \cdot \hat{s_j} \mid \qquad \hat{n} \cdot \hat{s_i} > 0 \tag{2.18}$$

For each $\hat{s_i}$ direction analyzed, the ray intersects the enclosure surface twice: where the ray emanates from the wall and where it strikes it to be absorbed or reflected (in the case of an opaque bounding surface). From the pair of equations 2.17 and 2.18 the radiation intensity I_i may be numerically calculated, an iterative method is imposed since the temperature field is not known.

Once the intensity field is known, the radiative heat flux inside the medium may be calculated, using equation 2.15, taking into account that, while using the DOM method, the incident radiation is approximated by:

$$G \approx \sum_{i=1}^{n} w_i I_i \tag{2.19}$$

The method has been applied considering the sets of directions and weights mentioned by Modest [32] and Saatdjian [34].

2.6.4 Modelling of transparent insulation in facades

In a material medium, like the building's facades, radiation is coupled with the thermal behaviour of solid elements. The temperature field through the facade containing transparent insulation materials must be determined from the energy conserva-

tion equation. In this case, it must include the thermal radiation heat transfer and it may be stated as:

$$\rho c \frac{DT}{D\tau} = \nabla(k\nabla T) - \nabla \cdot (\vec{q_r}) \tag{2.20}$$

The divergence of the radiative heat flux comes from the radiative heat transfer equation. Since it is an integral equation depending on intensity field, which depends on temperature, an iterative calculation is mandatory.

To model the use of transparent insulation, some restrictive assumptions can be assumed. The following are the most important:

- One-dimensional behaviour. It is considered that radiation intensity only varies in one direction (the width of TIM). This assumption does not imply isotropic radiation, the intensity may present directional variations.
- Azimuthal simmetry. Intensity is considered to not vary within a cone of angle θ around an axis perpendicular to the wall.
- Spectral variations are taken into account considering two bands: solar and thermal.

The discrete ordinates method applied to a one-dimensional slab, assuming azimuthal simmetry, produces for every direction, from $i = 1$ to N, $N/2$ intensities emanating from the right wall, and $N/2$ which emanate from the left wall. This means that for each direction, two equations are solved (positive and negative ways I_i^+ and I_i^-), the weights are the same for both.

Figure 2.6 shows the radiative intensity emanating from left wall in a one-dimensional plane-parallel medium in the right direction. Intensity depends on a space coordinate (z) and a direction coordinate (θ).

If z is chosen as the spacial coordinate between the two plates ($0 \leq z \leq L$), and the optical thickness coordinate τ is introduced, $d\tau = \beta dz$, with $0 \leq \tau \leq \tau_L$, equation 2.17 may be expressed as:

$$\mu_i \frac{dI_i}{d\tau} = (1-\omega)I_b - I_i + \frac{\omega}{4\pi} \sum_{j=1}^{N} \omega_j^{,} I_j (1 + A_1 \mu_i \mu_j) \tag{2.21}$$

$i = 1, 2, ...N$

Where $\mu = cos\theta$, is the direction cosine of the polar angle, $\omega_j^{,}$ are the summed quadrature weights and A_1 is the scattering phase function. Once the radiative intensity is solved the radiation flux can be computed as:

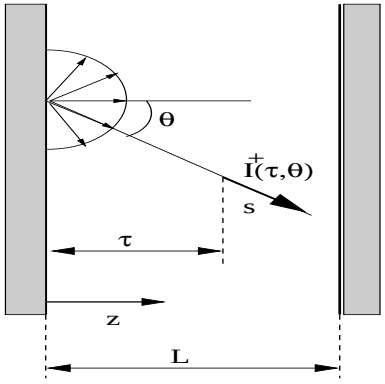

Figure 2.6: Radiative intensities in a one-dimensional plane-parallel medium emanating from the left wall

$$q_r = \sum_{i=1}^{N/2} \omega_i^{\cdot} \mu_i (I_i^+ - I_i^-) \tag{2.22}$$

The numerical algorithm to solve transparent insulation in the facades must take into account the use of bounding surfaces which maybe semitransparent (like glasses) or opaque selective surfaces. This set will be called a TIM layer.

TIM layer is considered in its most general implementation, as a part of a set of n glasses, which may be located at the oudoor or indoor surface of the facade and therefore, it may interacts with outdoor, indoor air, or with an air channel or an air gap. For these reasons, different boundary conditions must be considered.

The general algorithm may be summarized as:

1- Imposition of initial conditions: Temperatures and intensity radiation vectors.

2- Calculation of temperatures field.

2.1- Calculation of coefficients to solve the energy conservation equation (Eq.2.20) in a discrete one-dimensional form:

$$a_p T_p = a_e T_e + a_w T_w + b \tag{2.23}$$

Where T_p is the temperature in the node analyzed, T_e and T_w are the temperatures of the neighbour nodes, a_p, a_e, a_w and b are the coefficients which will be calculated for each specific boundary condition. The terms

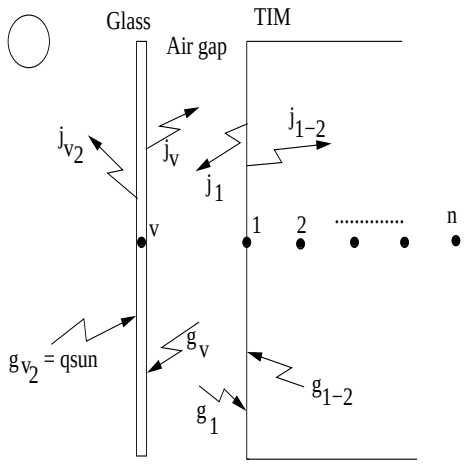

Figure 2.7: Solar radiation heat fluxes between the external glass and the TIM surface. In the general case, an air gap exists between glass and TIM. Solar reflectivity air-TIM ($\rho_{s_{TI_1}}$) is considered the same whatever the impinging direction is. g_{v_2} is the solar radiation impinging on the glass. g_{1-2} is the portion of solar radiation delivered by TIM to glass

involving the radiation heat flux will be present in the source term (b) of linear discrete equation. These terms are computed according to a solar and thermal radiation balance, as explained in Section 2.6.5.

2.2- Resolution of equation 2.23, by means of a tri-diagonal matrix algorithm [12], and evaluation of the maximum change of temperatures. The value admitted has been fixed in $\epsilon = 1\text{x}10^{-6}$.

2.3- Iteration is necessary since the coefficients will depend on radiation heat fluxes, which as well depend on intensity radiation, which at the same time depends on temperature.

3- Calculation for each position and direction of the new intensity field for both senses (positive and negative) and both bands (solar and thermal).

4- Points 2 and 3 are repeated until convergence for the current instant time is achieved.

2.6.5 Linking of TIM with bounding panes. Combination glass-air gap-TIM

Solar radiation balance

To calculate the solar radiation absorbed by the limiting glasses the radiosity method is used, which is schematically depicted at Figure 2.7.

Diffuse optical properties of the limiting glasses or opaque surfaces and solar reflectivity of TIM surface ($\rho_{s_{TI_1}}$) are known. ρ_{si} and ρ_{se} are respectively the internal and external solar reflectivities of limiting surfaces whatever the impinging direction and τ_s is its solar transmissivity. View factors are considered equal to 1 (as the width of the gap is low in contrast with the total height), so:

$$g_v = j_1 \qquad\qquad g_1 = j_v \tag{2.24}$$

$$j_v = \rho_{si} j_1 + \tau_s g_{v_2} \tag{2.25}$$

$$j_1 = \rho_{s_{TI_1}} j_v + (1 - \rho_{s_{TI_1}}) g_{1-2} \tag{2.26}$$

$$j_{v_2} = \rho_{se} g_{v_2} + \tau_s j_1 \tag{2.27}$$

$$j_{1-2} = \rho_{s_{TI_1}} g_{1-2} + (1 - \rho_{s_{TI_1}}) j_v \tag{2.28}$$

From the previous system of equations it is possible to obtain the solar radiation absorbed by the glass linked with TIM (q_{abs}):

$$q_{abs} = (g_v + g_{v_2}) - (j_v + j_{v_2}) \tag{2.29}$$

The value of g_{1-2} proceeds from the dom calculation:

$$g_{1-2} = \sum_{s=1}^{s=SN} W_s \mu_s I(1,s)_{\eta=solar} \tag{2.30}$$

Thermal radiation balance

Figure 2.8 represents the scheme used to calculate thermal radiation balance. Glass is considered thin and represented by one central node plus two nodes at both edges, temperature is considered to be the same for all the glass T_v. The reflectivity air-TIM is considered the same for any impinging direction ($\rho_{t_{TI_1}}$).

View factors are considered equal to 1, so:

$$g_v = j_1 \qquad\qquad g_1 = j_v \tag{2.31}$$

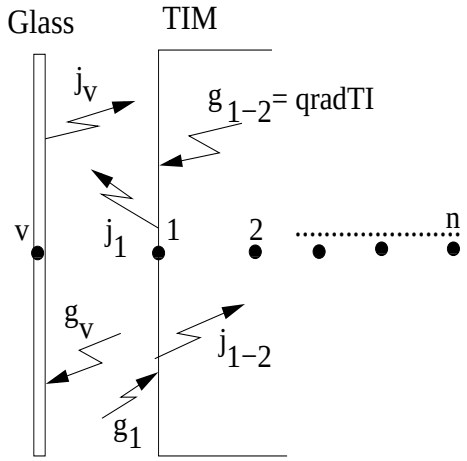

Figure 2.8: Thermal radiation heat fluxes between the external glass and the TIM surface. In the general case, an air gap exists between glass and TIM. Thermal reflectivity air-TIM ($\rho_{t_{TI_1}}$) is considered the same whatever the impinging direction is. g_{1-2} is the thermal radiation delivered by TIM to glass

From Figure 2.8 the following system of equations is deduced:

$$j_v = \epsilon_{tv}\sigma T_v^4 + (1-\epsilon_{tv})j_1 \tag{2.32}$$

$$j_1 = g_{1-2}(1-\rho_{t_{TI_1}}) + \rho_{t_{TI_1}} j_v \tag{2.33}$$

$$j_{1-2} = \rho_{t_{TI_1}} g_{1-2} + (1-\rho_{t_{TI_1}})j_v \tag{2.34}$$

$$j_v = \frac{\epsilon_{tv}\sigma T_v^4 + (1-\epsilon_{tv})(1-\rho_{t_{TI_1}})g_{1-2}}{1-(1-\epsilon_{tv})\rho_{t_{TI_1}}} \tag{2.35}$$

$$q_r = j_v - j_1 \tag{2.36}$$

g_{1-2} proceeds from the DOM calculation:

$$g_{1-2} = qradTI = \sum_{s=1}^{s=SN} W_s \mu_s I(1,s)_{\eta=thermal} \tag{2.37}$$

Energy balance

A net energy balance is performed in order to determine the superficial temperatures of glass and TIM. The heat fluxes are shown in Figure 2.9.

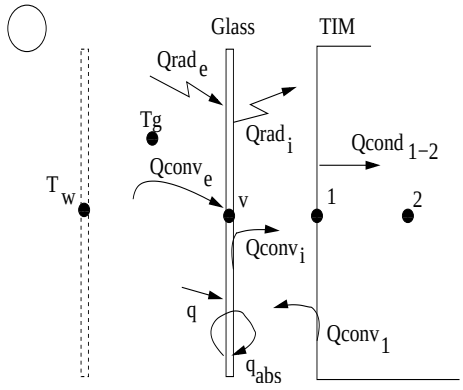

Figure 2.9: Heat fluxes between external glass and TIM surface. External glass is in contact with outdoor air at T_g, thermal radiation exchange is considered to occur with a surface at sky temperature (T_w). The same balance is valid for the internal surface of TIM and the internal wall. In this last case, T_w will be the temperature of the opposite wall.

In Figure 2.9, T_g corresponds to varying external air temperature. On the external surface of the glass the heat fluxes are due to thermal radiation ($Qrad_e$) and convection ($Qconv_e$). The glass can be in contact with external air, internal room air or with channel air (in the case that the TIM layer constitutes one of the skins of a double skin facade). In any of these cases the convective heat transfer coefficient will be particular and is represented by h^*. T^* will be the fluid temperature or the opposite wall temperature. External thermal radiation is linearized as:

$$Qr_e = hr_e(T_w - T_v) \tag{2.38}$$

$$Qc_e = h^*(T^* - T_v) \tag{2.39}$$

$$Qc_i = hg(T_v - T_1) \tag{2.40}$$

$$Qr_i = q_r \tag{2.41}$$

If the glass is external, that is, it is in contact with external air, T_w will be the sky temperature, otherwise it will be the temperature of the opposite wall. The convective heat transfer coefficient hg is calculated from the expressions cited in [35] for air gaps between parallel plates, in function of the walls temperatures, the gap width and the total height. General superficial balance on glass, will allow to calculate

glass temperature:

$$Qr_e + Qc_e + q + q_{abs} = q_{tr} + Qc_i \tag{2.42}$$

$$T_v = \frac{q + q_{abs} - q_r - Qc_i + hr_e T_w + h^* T^*}{hr_e + h^*} \tag{2.43}$$

The TIM interphase temperature is obtained from a surface thermal balance:

$$\frac{k_{TIM}(T_1 - T_2)}{\Delta x} = hg(T_1 - T_v) \tag{2.44}$$

2.6.6 Combination glass-TIM (with no air gap)

When TIM is glued to glass, the temperature of the glass and the TIM interphase is assumed to be the same ($T_v = T_1$). From the energy balance over the glass surface:

$$T_v = \frac{q + q_{abs} - q_{tr} + hr_e T_w + h^* T^* + T_2 k/\Delta x}{hr_e + h^* + k/\Delta x} \tag{2.45}$$

The thermal radiation balance in this situation is obtained as a particular case of the more general case with air gap described in the previous section. Thermal reflectivity glass-air is considered zero, and the thermal reflectivity TIM-air is replaced by the reflectivity TIM-glass.

A similar procedure is carried out to calculate solar radiation balance in this particular situation. Indoor solar reflectivity glass-air is considered zero, and solar reflectivity TIM-air is replaced by reflectivity TIM-glass.

2.7 Opaque solid walls

The model of opaque construction elements, such as brick, insulation panels and coverings is considered in this section. They are assumed to be made up of different layers of several materials. It is considered that there is a good thermal contact between the various materials. For conventional elements, as in the aforementioned examples, a standard transient and one-dimensional conduction model, as described by equation 2.1 is used. Thermophysical properties are considered to remain constant. The case of phase change materials is considered with more detail in the next section.

2.7.1 Phase change materials

The opaque wall can be made from phase change materials (PCM) to provide large thermal inertia making use of solid-liquid latent heat energy. In the simulation they

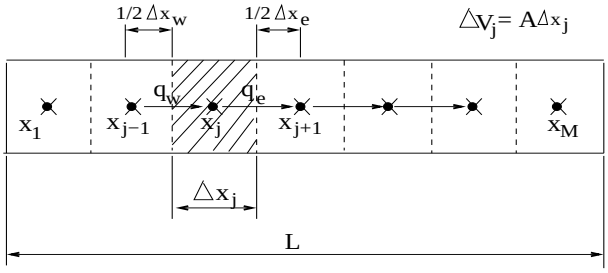

Figure 2.10: One-dimensional grid for opaque walls which can be constituted by phase change materials. Dashed zone represents the control volume (V), which is limited by control surfaces (SC).

are dealt as common opaque walls into which PCM has been impregnated. Convection in the liquid phase is neglected. In the late 19th century, J. Stefan [36] formulated the problem of finding the temperature distribution and freezing front history of a solidifying slab of water. Over last 40 years, the problem bearing his name, has been extended to include complex phenomena such as solidification of alloy systems, super cooling, melting due to Joule heating, etc. The feature of phase-change phenomena, is that in addition to the temperature field, the location of the interface is unknown. The model implemented and known as the Classical Stefan Problem incorporates the following simplifying assumptions: heat transfer is assumed to occur only by conduction, latent heat and phase change temperature are constant, the phases are separated by a sharp inter-phase of zero thickness, thermo-physical properties are assumed to be constant in each phase and density is considered constant (negligible convection within the liquid phase), no internal heating sources are present in the material. The main simplification is the assumption of negligible convection, if convection must be considered the problem is more involved [37].

Conservation energy formulated in the integral form leads to:

$$\int_t^{t+\Delta t} \frac{\partial}{\partial t}\left(\int_V E dV\right) dt - \int_t^{t+\Delta t} \int_{SC} (-\vec{q}\cdot\vec{n}\ \ dSdt) = 0 \tag{2.46}$$

Where $E = \rho e$ is the energy density (by volume unit) and $\vec{q}\cdot\vec{n}$ is the heat flux towards the volume V through the control surface (SC). Applying the expression 2.46 in a discrete form to a one dimensional mesh like the one shown in Figure 2.10, it stands:

$$(E_j^{n+1} - E_j^n)\Delta x_j = (q_{j-1/2}^{n+1} - q_{j+1/2}^{n+1})\Delta t_n \tag{2.47}$$

where j represents the position of the node and n the instant time. In an implicit

scheme, total contents of energy is expressed as:

$$E_j^{n+1} = E_j^n + \frac{\Delta t_n}{\Delta x_j}(q_{j-1/2}^{n+1} - q_{j+1/2}^{n+1}) \tag{2.48}$$

Discrete heat fluxes will be:

$$q_{j-1/2} = q_w = -\frac{T_j - T_{j-1}}{R_{j-1/2}} \qquad q_{j+1/2} = q_e = -\frac{T_{j+1} - T_j}{R_{j+1/2}} \tag{2.49}$$

Where R represents the thermal resistance, q_w and q_e stand for the heat fluxes through west and east faces, T_{j-1} and T_{j+1} represent the temperatures at the west and east nodes.

$$R_{j-1/2} = R_w = \frac{1/2\Delta x_{j-1}}{k_{j-1}} + \frac{1/2\Delta x_j}{k_j} \qquad R_{j+1/2} = R_e = \frac{1/2\Delta x_j}{k_j} + \frac{1/2\Delta x_{j+1}}{k_{j+1}} \tag{2.50}$$

Calling:

$$\mu = T - T_m \tag{2.51}$$

where T_m represents the melting temperature.

$$C_j = \frac{\Delta t}{\Delta x_j}\left(\frac{1}{R_{j+1/2}} + \frac{1}{R_{j-1/2}}\right) \tag{2.52}$$

$$Z_j = E_j^n + \frac{\Delta t}{\Delta x_j}\left(\frac{\mu_{j+1}^{n+1}}{R_{j+1/2}} + \frac{\mu_{j-1}^{n+1}}{R_{j-1/2}}\right) \tag{2.53}$$

Energy conservation is expressed as:

$$E_j^{n+1} + C_j\mu_j^{n+1} = Z_j \tag{2.54}$$

If specific heat in each phase is considered constant (C_S and C_L), total enthalpy is related with temperature, according to:

$$E_j = \begin{cases} \rho C_S(T - T_m) & \text{for } T < T_m, \\ \rho C_L(T - T_m) + \rho L & \text{for } T > T_m \end{cases} \tag{2.55}$$

Where L is the latent heat. In a solid node $\mu_j \leq 0$, thus:

$$E_j^{n+1} = \rho C_S \mu_j^{n+1} \leq 0; \qquad \mu_j^{n+1} = \frac{Z_j}{\rho C_S + C_j} \leq 0 \tag{2.56}$$

in a liquid node $\mu_j > 0$

$$E_j^{n+1} = \rho C_L \mu_j^{n+1} + \rho L > 0; \qquad \mu_j^{n+1} = \frac{Z_j - \rho L}{\rho C_L + C_j} > 0 \tag{2.57}$$

In a partially liquid and partially solid volume control ("mushy node"):

$$0 < E_j^{n+1} < \rho L; \qquad \mu_j^{n+1} = 0 \tag{2.58}$$

A mushy volume will contain an interface, the fraction of volume occupied by liquid is given by expression 2.59.

$$\lambda_j = \frac{E_j}{\rho L} \tag{2.59}$$

2.7.2 Calculation algorithm for PCM model

1. From the values of temperatures of the previous iteration, or the guessed values for the first iteration (T_j^* and μ_j^*), Z_j and C_j are calculated.

$$Z_j = E_j^n + \frac{\Delta t}{\Delta x_j}\left[\frac{\mu_e^{n+1}}{R_e} + \frac{\mu_w^{n+1}}{R_w}\right] \tag{2.60}$$

$$C_j = \frac{\Delta t}{\Delta x_j}\left[\frac{1}{R_e} + \frac{1}{R_w}\right] \tag{2.61}$$

2. Determination of the new value of μ_j:

$$\mu_j^{n+1} = \begin{cases} \frac{Z_j}{\rho C_s + C_j} & \text{for } Z_j \leq 0 \text{ (solid state)}, \\ 0 & \text{for } 0 < Z_j < \rho L \text{ (mushy state)}, \\ \frac{Z_j - \rho L}{\rho C_L + C_j} & \text{for } Z_j \geq \rho L \text{ (liquid state)} \end{cases} \tag{2.62}$$

3. If the maximum absolute difference between the new value of μ_j and the previous one, is lower than a fixed tolerance, for all the control volumes, the new values of temperatures and energy contents are calculated, and a new instant time is initiated. Otherwise, point 1 is again carried out from the previous values of μ_j. Thus,
   If $MAX|\mu_j^{n+1} - \mu_j^*|_{1 \leq j \leq M} \leq$ tolerance
   then, $T_j^{n+1} = \mu_j^{n+1} + T_m$ and $E_j^{n+1} = Z_j - C_j \mu_j^{n+1}$
   otherwise, return to point 1

Grouping terms for the temperature of the actual calculated node, and the neighbour nodes, temperature may be obtained from a linear expression like the expressed by equation 2.63, applying a tri-diagonal matrix algorithm.

$$a_p T_p = a_e T_e + a_w T_w + b \tag{2.63}$$

As indicator of phase, the liquid fraction (λ_j) of the control volume is utilized.

$$\lambda_j^n = \begin{cases} 0 & \text{if } E_j^n \leq 0 \text{ (solid state)} \\ \frac{Z_j}{\rho L} & \text{if } 0 < E_j^n < \rho L \text{ (mushy state)} \\ 1 & \text{if } E_j^n \geq \rho L \text{ (liquid state)} \end{cases} \tag{2.64}$$

This formulation does not compute the interface location, it becomes a result of the enthalpy formulation, and is an output derived from the liquid fraction. The implemented model has been verified by the computation of cases with analytical solutions, the results are shown in Chapter 3.

2.8 Air channel heat transfer and fluid flow

The most relevant feature of double skin facades is the presence of an air channel between both layers which constitute the facade. This air space is used to collect or evacuate the solar radiation absorbed by the envelope, thus the air channel may represent an additional thermal resistance contributing to reduce the overall thermal coefficient of facade or it may contribute to the pre-heating of an air flow rate which may be used in different manners.

Heat transfer within facade channels has been experimentally studied [38], [39] and numerically analyzed taking into account laminar regime and turbulent mixed convection applying a two-equations turbulence model [40], [41] and [42].

When the channel remains closed, air movement due to natural convection has been studied extensively, due to the wide applicability of this geometry in many engineering fields. Different boundary conditions have been analyzed, including the case of isothermal side walls and asymmetric heating and radiative condition [43].

2.8.1 Governing equations

Heat transfer and fluid flow within facade channel is described by Navier-Stokes equations. These equations represent a conservation principle of mass and momentum. In a transient, incompressible, two-dimensional approach, in cartesian co-ordinates they are expressed by:

$$\frac{\partial u}{\partial x} + \frac{\partial v}{\partial y} = 0 \tag{2.65}$$

$$\frac{\partial(\rho u)}{\partial \tau} = -\frac{\partial(\rho u u)}{\partial x} + \rho g_x - \frac{\partial P}{\partial x} - \left(\frac{\partial \tau_{xx}}{\partial x} + \frac{\partial \tau_{yx}}{\partial y}\right) \tag{2.66}$$

$$\frac{\partial(\rho v)}{\partial \tau} = -\frac{\partial(\rho v v)}{\partial y} + \rho g_y - \frac{\partial P}{\partial y} - \left(\frac{\partial \tau_{xy}}{\partial x} + \frac{\partial \tau_{yy}}{\partial y}\right) \tag{2.67}$$

where, according to Stokes viscosity constitutive law:

$$\tau_{xx} = -2\mu\frac{\partial u}{\partial x} + \frac{2}{3}\mu\nabla\cdot\vec{V} \tag{2.68}$$

$$\tau_{yy} = -2\mu\frac{\partial v}{\partial y} + \frac{2}{3}\mu\nabla\cdot\vec{V} \tag{2.69}$$

$$\tau_{xy} = \tau_{yx} = -\mu\left(\frac{\partial u}{\partial y} + \frac{\partial v}{\partial x}\right) \tag{2.70}$$

If the flow is not isotherm, it is necessary to include the energy conservation equation:

$$\frac{\partial T}{\partial \tau} + u\frac{\partial T}{\partial x} + v\frac{\partial T}{\partial y} = \frac{k}{\rho c_p}\left(\frac{\partial^2 T}{\partial x^2} + \frac{\partial^2 T}{\partial y^2}\right) \tag{2.71}$$

Where the friction heat is considered negligible, there is no radiation heat exchange, and thermo-physical properties are considered constant.

The solution of this system of equations can be carried out numerically, and from its solution, detailed temperature, velocity and pressure distributions are obtained. However, this approach called Computational Fluid Dynamics (CFD) is not possible in this case from a practical point of view, due to excessive CPU time consumption. For this reason, a one-dimensional and transient numerical simulation is used. In this context, it will be useful to distinguish the following flow configurations:

- Closed channel
  - Temperature differences between walls produce a recirculating natural convection flow, similar to a highly differentially heated cavity flow [44], which transports energy from the hot wall to the cold wall.
- Opened channel

- Forced convection. A known air flow rate is imposed.
- Natural convection. The flow rate is driven by the temperature difference between the air and the channel walls. The result is a time-dependent flow rate.

2.8.2 Closed channel: natural convection heat transfer in closed enclosures

Convective heat transfer in a rectangular or square cavity filled with gas (commonly air) has been extensively studied since the forties. This fact is due to its importance in many engineering applications: cooling of electronic equipment, heat exchangers, insulating windows, solar collectors and also facade application. Literature deals with closed cavities with isothermal side walls at different temperatures [45], [46] and [47], opened channels with isothermal and adiabatic side walls [48] and asymmetric heating coupled with radiative condition [43].

Sets of correlations based on experimental data and numerical work have been published by several authors. Ostrach [49] has described the physical phenomena of a buoyancy driven flow in a closed enclosure, remarking that the main difficulty in this configuration is the interaction between the boundary layers formed near the walls and the core region. Since the core is partially or totally encircled by the boundary layers, the core flow is not determined from the boundary conditions, but depends on the boundary layer which, in turn is influenced by the core.

Dimensional analysis of governing equations leads to the well-known set of non-dimensional groups governing natural convection: Prandtl: $Pr = \frac{\mu Cp}{\lambda}$ (0.71 for air with $-20 \leq T \leq 40$), Grashof: $Gr_w = \frac{g \cdot \beta \cdot w^3 \cdot \Delta T}{\nu^2}$, Rayleigh: $Ra_w = Gr_w \cdot Pr$ and Reynolds: $Re_w = \frac{w_o \cdot w}{\nu}$ where w_o is the mean velocity. In this geometrical configuration the rate between total height of the cavity (H) to the width (w) thus, the aspect ratio, constitutes an additional non-dimensional group which influences thermal transport.

Heat transfer through gas layers confined in a rectangular cavity composed by isothermal vertical walls, and perfectly conducting or adiabatic horizontal surfaces, was investigated by Batchelor [50], for cases with aspect ratio from 5 to 200, ElSherbiny [45] developed experimental correlations for aspect ratios from 5 to 110. Depending on the Rayleigh number and the aspect ratio, different flow regimes could occur within the cavity. All authors conclude that for low Rayleigh numbers, convection is not important compared with conduction. Also in the asymptotic case of $H/w \rightarrow \infty$ and general Ra, conduction is the sole means of heat transfer [49]. In these cases, fluid flow is completely vertical and temperature distribution in the air vary linearly between the walls.

With increasing Ra numbers and depending also on the aspect ratio ($A = H/w$), circulation flow intensifies and it concentrates in a narrow boundary layer along the plates. In this regime, the upward and downward moving flow layers are separated by a stratified core region, as was experimentally shown by Eckert and Carlson [51]. The boundary layer may become turbulent and corner areas may present eddy zones.

Correlations for closed enclosures

The following correlation for the mean Nusselt number is cited by Catton [52]:

$$\overline{Nu_w} = 0.22\left(\frac{Pr}{0.2+Pr}Ra_w\right)^{0.28}\left(\frac{H}{w}\right)^{-0.25} \tag{2.72}$$

for $2 < \frac{H}{w} < 10, \quad Pr < 10^5, \quad 10^3 < Ra_w < 10^{10}$

Hollands [53] experimented with enclosures with different slope angles (0-75°), and determined the following correlation between Nusselt number and Rayleigh number:

$$Nu = 1 + 1.44\left[1 - \frac{1708(sin1.8\cdot\beta)^{1.6}}{Ra\cdot cos\beta}\right]\left[1 - \frac{1708}{Ra\cdot cos\beta}\right]^{+} + \left[\left(\frac{Ra\cdot cos\beta}{5830}\right)^{\frac{1}{3}} - 1\right]^{+} \tag{2.73}$$

Where the $+$ exponent means that only the positive values of that term should be used, otherwise it has to be considered null. Rayleigh is calculated taking the width of the enclosure (w) as characteristic length. According to Duffie and Beckmann [15], this expression is also applicable to vertical enclosures.

ElSherbiny [45] experimentally tested an air layer bounded by flat isothermal plates at different temperatures and by a perfectly conducting boundary around the edges, considering aspect ratios between 5 and 110, and for a Rayleigh range between 10^2 to $2\cdot10^7$. The following correlation equations to calculate the heat transfer across the air layer were deduced.

$$\overline{Nu_w} = max(Nu_1, Nu_2, Nu_3) \qquad 10^3 < Ra_w < 10^7 \tag{2.74}$$

with:

$$Nu_1 = 0.0605\cdot Ra_w^{1/3} \qquad Ra_w \leq 10^3, \qquad \overline{Nu_w} \simeq 1 \tag{2.75}$$

$$Nu_2 = \left[1 + \left[\frac{0.104\cdot Ra_w^{0.293}}{1+(6310/Ra_w)^{1.36}}\right]^3\right]^{1/3} \tag{2.76}$$

$$Nu_3 = 0.242 \cdot \left[\frac{Ra_w}{\frac{H}{w}} \right]^{0.272} \tag{2.77}$$

Yin et al. [47] obtained experimental data and proposed the following correlation which fitted experiments in a 94% within a deviation of around 20%:

$$Nu = 0.23 \cdot \frac{H}{w}^{-0.131} \cdot Ra_w^{0.269} \quad 10^3 \leq Ra_w \leq 5 \times 10^6 \quad 4.9 \leq \frac{H}{w} \leq 78.7 \tag{2.78}$$

Wright [54] suggested a correlation based on data from the literature, specially for the purpose of window analysis, for $\frac{H}{w} \geq 40$ and $Ra_w < 10^6$.

$$Nu = 0.0673838 \cdot Ra_w^{0.3} \quad 5 \times 10^4 \leq Ra_w \leq 10^6 \tag{2.79}$$

$$Nu = 0.028154 \cdot Ra_w^{0.4134} \quad 10^4 \leq Ra_w \leq 5 \times 10^4 \tag{2.80}$$

$$Nu = 1 + 1.75967 \times 10^{-10} \cdot Ra_w^{2.2984755} \quad Ra_w \leq 10^4 \tag{2.81}$$

Zhao et al. [46] proposed a correlation based on experimental data (with a maximum deviation of 6%), for Rayleigh numbers chosen so that only laminar flow occurred.

$$Nu = \left[1 - 0.00813277 \frac{Ra_w}{H/w} + 0.00723291 \frac{Ra_w}{H/w}^{1.08597} \right]^{0.279072} \tag{2.82}$$

$Ra_w < 10^4$ and $5 \leq H/w \leq 80$

CFD experiments for closed enclosures

Numerical simulation has been carried out within this work to test some of the available correlations previously described. CFD simulations were performed with a laboratory code (DPC) considering aspect ratios of 20, 40 and 80 and Rayleigh numbers from 10^3 to 10^6. These aspect ratios may be found in building facades, although it should be remarked that generally Rayleigh numbers within a facade channel or enclosure (closed channel) will be larger than 10^6, this fact leads to a turbulent flow within the facade. In an actual building, air channel is not rectangular: it may have a variable section, and usually it accounts with internal obstacles. Since a real situation may present a large range of geometrical variations, the rectangular geometry is considered in this approach as the simplified suitable geometry. Modelling was two-dimensional, this means that the length in the 'z' co-ordinate is large compared with the thickness w. Boundary conditions are shown in Figure 2.11.

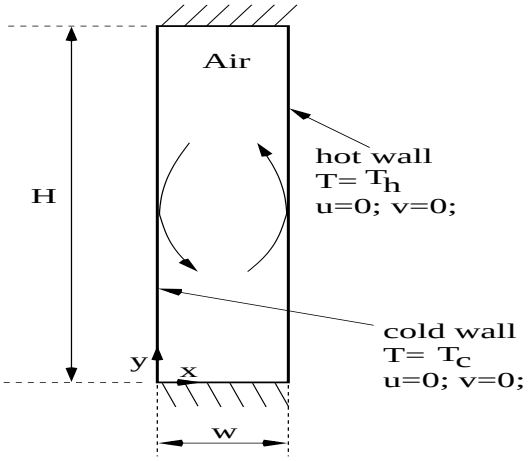

Figure 2.11: Schematic vertical enclosure, top and bottom are adiabatic, side walls remain isothermal, right wall is at a hot temperature, while left one is at a cold temperature

At top and bottom, zero heat flux conditions are imposed:

$$\frac{\partial T}{\partial y}|_{y=0} = 0 \qquad \frac{\partial T}{\partial y}|_{y=H} = 0 \tag{2.83}$$

In all bounding surfaces, velocity is null.

$$u(x=0,y) = v(x=0,y) = 0 \qquad u(x=w,y) = v(x=w,y) = 0 \tag{2.84}$$

$$u(x,y=0) = v(x,y=0) = 0 \qquad u(x,y=H) = v(x,y=H) = 0 \tag{2.85}$$

Vertical side walls are isothermal:

$$T(x=0,y) = T_c \qquad T(x=w,y) = T_h \tag{2.86}$$

A finite volume method has been used to discretize differential equations, an orthogonal (refined near the vertical walls) grid of 80x240 nodes has been used in all the cases, an upwind (or SMART) numerical scheme is applied to solve the convective-diffusive terms, and a variation of the simple algorithm [12] is used to handle the coupling between pressures and velocities. Air properties were assumed to be constant, except for the density which is treated with the Boussinesq approximation. Iterative calculation is stopped when the steady-state solution is reached.

Solution is considered to be converged when maximum increment and maximum residual of each one of the variables (mass, x-velocity, y-velocity and T) are lower than a prescribed value (10^{-8}) for any grid point. Once steady state has been reached, the average Nusselt number is calculated.

$$\overline{Nu} = \frac{q}{\frac{k}{w}(T_h - T_c)} \tag{2.87}$$

where k is the thermal conductivity of air, w is the width of the enclosure, T_h and T_c are the temperatures of the vertical walls and $q = -k\frac{\partial T}{\partial n}|_{wall}$ is the average convective heat transfer across the air layer.

At Ra=10^3, the flow is laminar and the conduction regime, with $Nu = 1$ is observed.

As stated by Wright [55], as Ra is increased further, a multicellular flow arises. The critical value of Ra at which the onset of secondary cells appears is given by expression 2.88.

$$Ra_c = 8000(1 + \frac{5}{H/w})Pr \tag{2.88}$$

Wright presents a summary of experimental data about the observation of secondary cells at different Ra numbers and aspect ratios by different researchers, pointing that thermal stratification in the core suppresses the formation of secondary cells. Thermal stratification will be stronger in enclosures of smaller aspect ratio. Figure 2.12 shows the results of temperature distribution through the enclosure of aspect ratio 20 for different Ra numbers predicted by this numerical work. When Ra is sufficiently large, the heat transfer is governed primarily by turbulent boundary layers, separated from each other by a core of uniform temperature. In this work, it has been found that no laminar steady solution was found from $Ra = 10^5$ from the aspect ratio $A = 40$. This behaviour is in accordance with the results found by different researchers [55], [40], [41]. To solve those cases, a two-equations $k - w$ turbulent model has been applied. It consists in a transformation of Navier-Stokes equations, assuming that a turbulent flow may be modelled by a mean value of the instantaneous properties plus a fluctuation component.

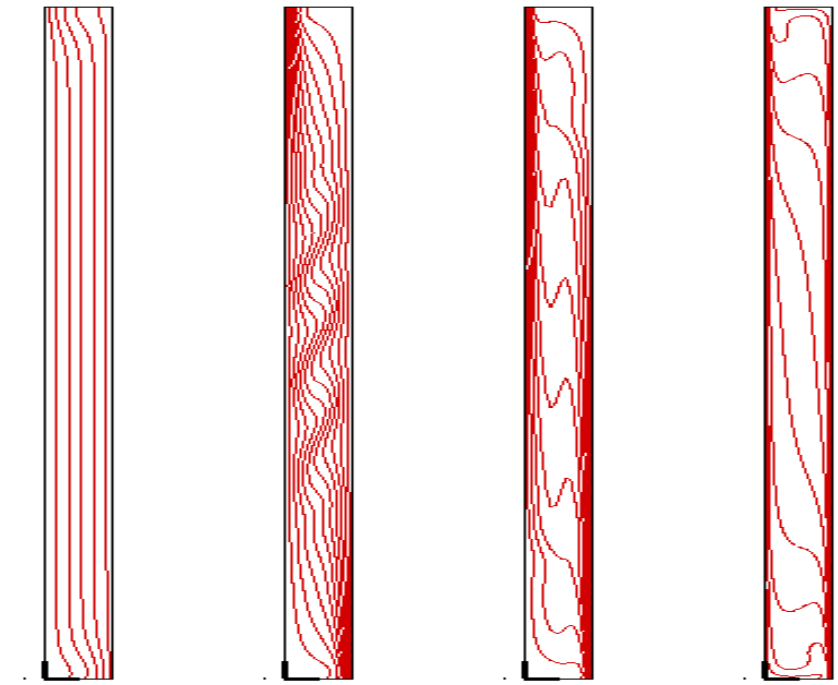

Figure 2.12: Temperatures distribution obtained for a closed enclosure with H/w=20 and different Rayleigh numbers. a)$Ra = 10^3$; b)$Ra = 10^4$, c)$Ra = 10^5$, d)$Ra = 10^6$

This treatment originates a modified set of Navier-Stokes equations, known as Reynolds Averaged Navier-Stokes equations (RANS), which introduce new unknowns to the problem. The $k - w$ turbulent model introduces algebraic empirical correlations to solve the additional transport equations arisen to compute the turbulent variables [56]. In certain cases, it is also possible to solve the original governing equations in turbulent flows directly (without models), this approach is called DNS: direct numerical simulation [57].

The numerical results agree with those reported in the literature, as it is shown in Figures 2.13 and 2.14.

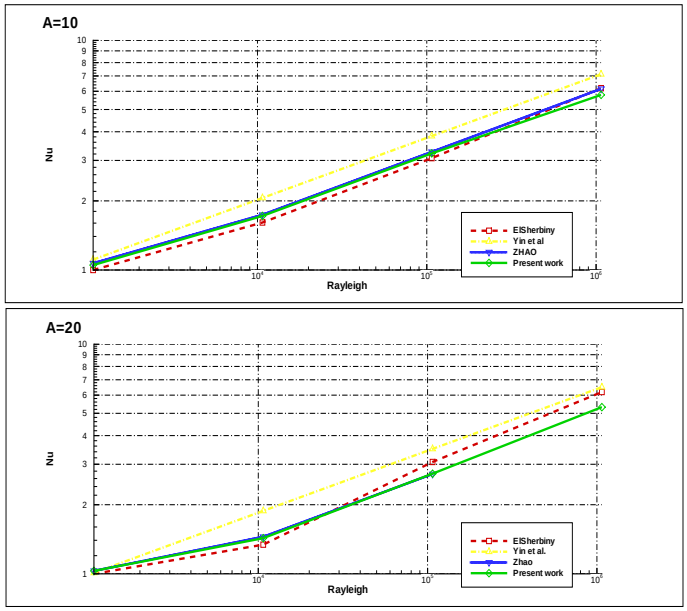

Figure 2.13: Nusselt number prediction by different authors, for a closed enclosure with aspect ratio A=10 and A=20, as a function of Rayleigh number (Ra_w)

2.8.3 Opened channel: Natural and forced convection

In the air channel, pure natural convection is produced as a result of density variations between channel air and ambient air (outdoor or indoor) and boundary conditions. In other situations, such as in *Caixa Terrassa building*, the air channel is part of the HVAC system and therefore the airflow is mainly caused by mechanical devices. Also, wind velocity may induce a flow inside the channel. In general, all these forces may coexist resulting in a mixed convection flow. Reynolds and Grashof numbers allow to determine which is the dominant flow. The relationship between both flow mechanisms may be represented by Archimedes number:

$$Ar = \frac{Gr}{Re^2} = \frac{gH\beta\Delta\vartheta}{w^2} \tag{2.89}$$

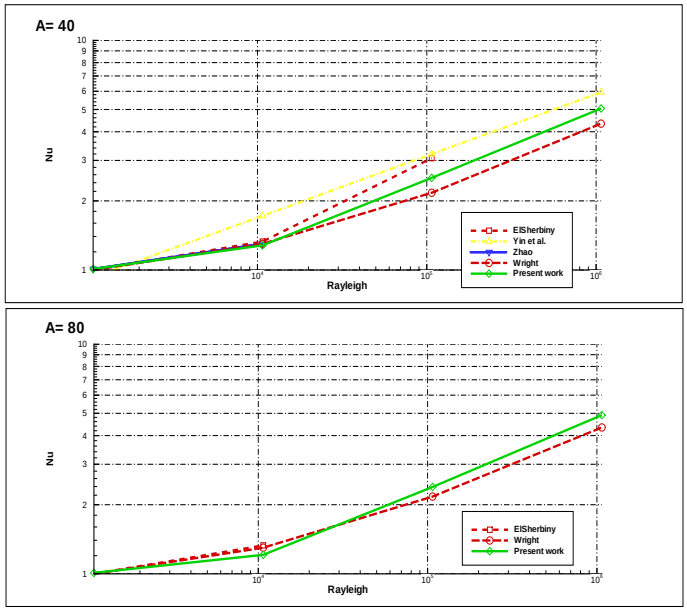

Figure 2.14: Nusselt number prediction by different authors, for a closed enclosure with aspect ratio A=40 and A=80, as a function of Rayleigh number (Ra_w)

This relationship, according to Zollner [38], allows to determine the correlation which can be used to determine the Nusselt number, according to the flow features:

$Ar \leq 0.225$	forced convection
$0.225 < Ar < 10$	mixed convection
$Ar \geq 10$	natural convection

Air flow in opened channel due to natural convection

Natural convection between parallel plates, has been studied experimentally and numerically since many years ago, due to its importance and applicability in different engineering fields, Elenbaas [58] was the first to document a detailed study of the thermal characteristics of such configuration, and his experimental results were later confirmed numerically.

Bar-Cohen and Rohsenow [48], developed correlations for fully developed flows expressing the heat transfer coefficient in terms of the ambient or inlet temperature. They obtained analytic expressions in a symmetric isothermal or isoflux channel, as well as in a channel with an insulated wall (case called asymmetric).

Isotherm plates:

$$Nu_o = \left[\frac{576}{(Ra_w \cdot w/H)^2} + \frac{2.873}{(Ra_w \cdot w/H)^{0.5}}\right]^{-0.5} \quad symmetric \tag{2.90}$$

$$Nu_o = \left[\frac{144}{(Ra_w \cdot w/H)^2} + \frac{2.873}{(Ra_w \cdot w/H)^{0.5}}\right]^{-0.5} \quad asymmetric \tag{2.91}$$

In these expressions, subindex o indicates entrance or ambient value:

$$Nu_o = \frac{q/A}{(T_w - T_o)k/w} \tag{2.92}$$

Rayleigh is calculated with w as characteristic length.

Plates with constant heat flow:

$$Nu_{o,H} = \left[\frac{48}{Ra^*} + \frac{2.51}{(Ra^*)^{0.4}}\right]^{-0.5} \quad symmetric \tag{2.93}$$

$$Nu_{o,H} = \left[\frac{24}{Ra^*} + \frac{2.51}{(Ra^*)^{0.4}}\right]^{-0.5} \quad asymmetric \tag{2.94}$$

A modified Rayleigh number is used to compute the local Nusselt:

$$Ra^* = \frac{\rho^2 g \beta c_p q^* w^5}{\lambda^2 H \mu} \tag{2.95}$$

In isoflux conditions, Nusselt is defined as:

$$Nu_{o,H} = \frac{q^*}{(T_{w,H} - T_o)k/w} \tag{2.96}$$

Where $T_{w,H}$ indicates the wall temperature at position H and q^* is the imposed heat flux [Wm^{-2}].

Figure 2.15 shows the values predicted by these correlations for the isotherm plates and the isoflux conditions.

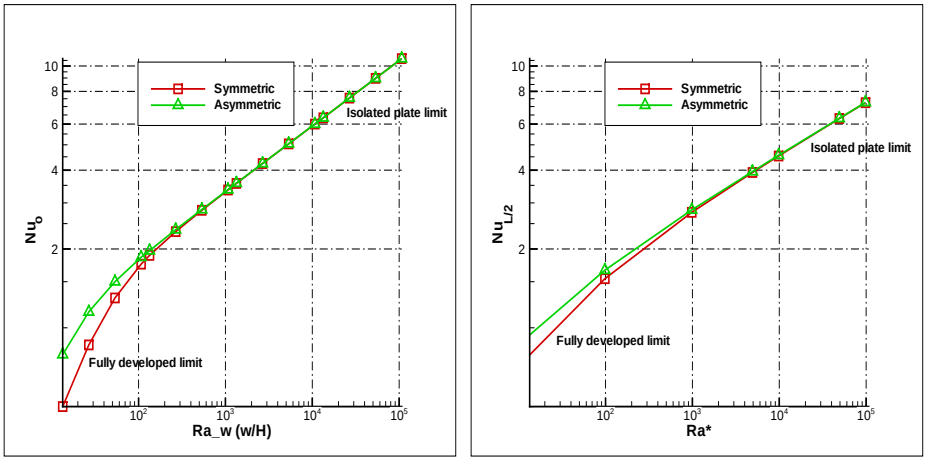

(a) (b)

Figure 2.15: Nusselt number according to Bar-Cohen [48]: a) Isotherm plates; b) Isoflux conditions

Fedorov and Viskanta [59] studied turbulent heat transfer in asymmetric heated plates (a plate is considered to present a uniform heat flux whereas the opposite wall remains adiabatic) assuming natural convection (fluid motion driven by thermal buoyancy forces). They applied a low Reynolds number $k-\epsilon$ turbulence model and compared the predictions with available experimental data. They determined the following correlation for mean Nusselt number, with a turbulence intensity at the inlet of 0%.

$$\overline{Nu_w} = 2.10[Gr_w \cdot Pr \cdot (w/H)]^{0.2} \tag{2.97}$$

Miyatake and Fujii [60] obtained the following empirical correlation for an identical physical situation but for laminar flow:

$$\overline{Nu_w} = 0.613[Gr_w \cdot Pr \cdot (w/H)]^{0.25} \tag{2.98}$$

valid for $Pr = 0.7$, for small values of $Gr \cdot Pr \cdot (w/H) < 1$, the average Nusselt number is given by:

$$\overline{Nu} = \frac{1}{12} \cdot Gr_w \cdot Pr \cdot (w/H) \tag{2.99}$$

Figure 2.16 shows the Nusselt variation according to the correlations aforementioned.

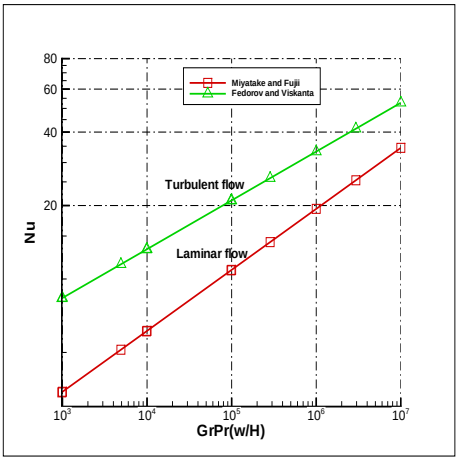

Figure 2.16: Correlations of Fedorov [59] for turbulent asymmetric heated plates and Miyatake [60] for laminar flow

Air flow in opened channel due to forced convection

In case of forced convection, for thermally and hydrodynamically developing flow, according to Rohsenow [61], the following correlations are proposed:

$$Nu = 3.78 + \frac{0.0156[Pe\frac{w}{H}]^{1.14}}{1 + 0.058[Pe\frac{w}{H}]^{0.64}Pr^{0.17}} \tag{2.100}$$

For turbulent flow (Re>2300), an expression for pipes with smooth walls may be used introducing an equivalent hydraulic diameter (d) :

$$Nu = \frac{(f_t/8)(Re - 1000)Pr}{1 + 12.7\sqrt{f_t/8}(Pr^{2/3} - 1)}[1 + (\frac{d}{H})^{2/3}] \tag{2.101}$$

The friction factor for turbulent tube flow can be calculated using the following expression [62]:

$$f_t = (1.82logRe - 1.64)^{-2} \tag{2.102}$$

Heat transfer coefficients are shown in Figure 2.17.

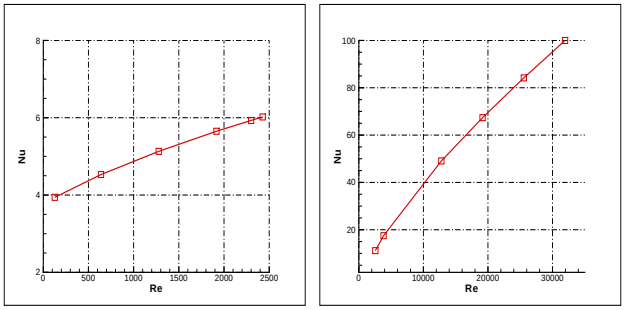

(a) (b)

Figure 2.17: Nusselt correlation for the case of forced convection in channel. a) For $Re < 2300$, expression 2.100 is used; b) For $Re > 2300$, turbulent heat transfer is expressed by expression 2.101

2.8.4 One-dimensional model used in $AGLA$ code

As aforementioned, due to computational limitations, the transient simulation of the double skin facade (typically one year simulation) may not be feasible with a two-dimensional model of the channel, for this reason the air channel integrated within the facade is modelled through a transient one-dimensional (in the vertical direction) algorithm. The parabolic structure of the flow allows to apply a step-by-step method to obtain the velocity, temperature and pressure at the outlet of each control volume from the upstream values.

The integral equations expressing mass, momentum and energy conservation are solved numerically by means of a finite volume method. The thermophysical properties are assumed to be constant. Figure 2.18 represents the finite control volume where the conservation equations are applied.

Continuity equation, considering constant cross-sectional channels, is expressed as:

$$V_{j+1} = V_j \tag{2.103}$$

Momentum equation:

$$\rho \frac{V_j - V_j^0}{\Delta t} \Delta z + 2\tau_w \frac{\Delta z}{w} + g\rho\Delta z = P_j - P_{j+1} \tag{2.104}$$

Energy equation:

$$\rho c_p \frac{T_j - T_j^0}{\Delta t} w + \frac{\dot{m} c_p}{\Delta z}(T_{j+1} - T_j) = q_{wi} + q_{wo} \tag{2.105}$$

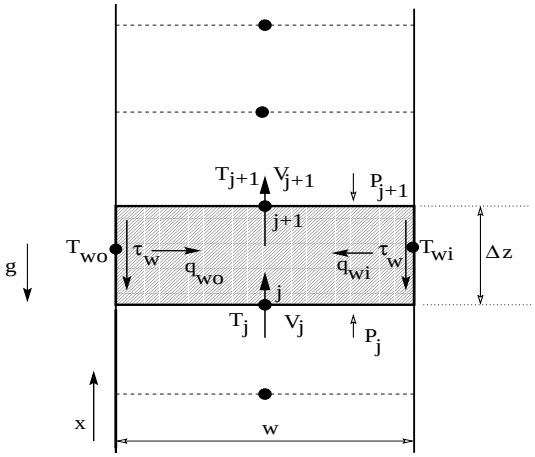

Figure 2.18: Control volume of the air channel, one-dimensional approach

Where:

$$q_{wi} + q_{wo} = h_{wi}(T_{wi} - \bar{T}_j) + h_{wo}(T_{wo} - \bar{T}_j) \tag{2.106}$$

and

$$\bar{T}_j = \frac{(T_{j+1} + T_j)}{2} \tag{2.107}$$

The air channel may contain curtains of variable height. Therefore, the modelling introduces control volumes of two types:

- Constituted by air as shown in Figure 2.18.
- Constituted by the air of both branches of the channel at each side of the channel blind.

In this last case, velocity and pressure are assumed to be equal at both branches, whereas energy is solved for each branch, obtaining a temperature at the outlet of each one. The shear stresses are affected by a coefficient to take into account additional loss of pressure.

Opened channel with forced convection flow

Assuming that input velocity is known, the step-by-step algorithm is applied to calculate the velocity, pressure and temperature for each control volume. The general algorithm has two parts:

- Momentum equation. Pressure distribution is obtained from equation 2.104. Shear stresses τ_w are evaluated as:

$$\tau_w = \frac{f}{4}\frac{\dot{m}^2}{2\rho w^2} \tag{2.108}$$

  where $\dot{m}$ is the mass flow rate per unit of channel depth and f is the friction factor calculated as a function of Reynolds number and the state of the surfaces [35]. The Boussinesq approximation is used to evaluate the gravitational forces.

- Energy equation. Temperature distribution is obtained from the convective heat tranfer coefficients h_{wi} and h_{wo}. They are assumed to be equal and they are derived from the Nusselt number.

$$h = \frac{Nu\ \ k}{w} \tag{2.109}$$

  Expressions for Nusselt number are exposed at sections 2.8.2 and 2.8.3. In the case of closed channel, expressions from ElSherbiny were used (equation 2.74). In the case that the channel is opened, correlations described by expressions 2.100 and 2.101 are used, depending on the flow regime. When very low air velocities are produced in the channel (induced by natural convection), heat transfer coefficient is calculated from a linear interpolation of the values corresponding to closed channel (expression 2.74) and those obtained for an imposed low velocity calculated from expression 2.100.

The heat flows obtained at the walls of the channel with the step-by-step algorithm are used as boundary conditions for the solid and glazed areas. Expressions 2.108, 2.100 and 2.101 were obtained for situations that were not exactly equivalent to the channel flow that is considered here. For instance, expression 2.100, for natural convection between plates, can only be applied if the temperatures of the plates are uniform. However, the validation with experimental set-ups confirms that they are appropriate for this situation.

Opened channel with natural convection flow

The step-by-step algorithm is very efficient, but only allows to evaluate the pressure, temperature and velocity distributions of the channel when their respective values at the inlet are available. This is not the case for natural convection flows, as the inlet velocity V_{in} is not imposed, but induced by the temperatures of the blind and

channel walls. Instead, the boundary conditions are the inlet pressure, P_{in}, that is a function of the inlet velocity:

$$P_{in} = -\frac{1}{2}\rho V_{in}^2 \tag{2.110}$$

and the outlet pressure P_{out}, that must agree with the ambient pressure at the top of the channel:

$$P_{out} = -\rho_o g h \tag{2.111}$$

Where ρ_o is the external air density. The relative inlet pressure is not zero because of the acceleration from an unperturbed point at the bottom of the channel, with P=0 and V=0, assuming an isentropic flow.

To solve this situation using the step-by-step algorithm, the outlet pressure must be considered as a function of the inlet velocity (and the temperature distribution at the channel walls). Then, the problem is reduced to solve the algebraic equation:

$$P_{out}(V_{in}) = -\rho_o g h \tag{2.112}$$

Where P_{out} is a function of V_{in}, that is evaluated using step-by-step algorithm. A Newton-Raphson method is used to solve this equation. To do so, the step-by-step function must be evaluated a number of times before obtaining the natural convection velocity, so the computational cost of the natural convection simulations is substantially higher.

In the present model, the effect of pressure drops due to the geometry of the inlet and outlet ports, and the effects of wind are not considered. In general, these effects are not important for forced convection, but might produce significant effects in the natural convection flow rates.

2.9 Modelling of integrated solar collector-accumulators in facades

Facades offer the possibility of using the opaque areas to increase the thermal inertia or accumulate sensible heat. This accumulation may be carried out with water. This idea has been tested and studied since several years ago, by many researchers [63], [64], [65]. Nowadays, however, more detailed models and powerful computer tools are available in order to optimize these designs.

Facades may play the role of integrated solar collectors, with the aim of getting a solar heated water flow, which may be used to provide space heating, or domestic hot water (solar combisystem). This possibility is implemented in the form of a modular integrated solar collector (as shown in Figure 2.19), which should be easily combined with the conventional elements of a facade, it could be implemented in a single or double skin facade, and must fulfill esthetics requirements. These implementations have been the objective of analysis of a CRAFT european project developed within the framework of this thesis [66].

This kind of system requires an accurate design since it works linked with other systems which may affect its performance. A first approximation to model the complexity of the whole system, is developing a numerical tool to be able to predict the performance of a facade in which an integrated liquid-based solar collector-accumulator is implemented.

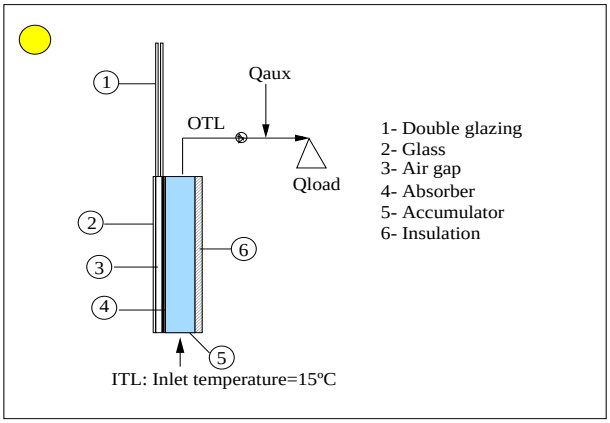

Figure 2.19: Schematic design of the facade with an integrated solar collector to produce domestic hot water.

2.9.1 Accumulator model

Thermal storage is one of the relevant aspects in any active solar system in order to foresee situations with no solar availability (nights, cloudy days, etc), to optimize thermal performance of the whole system. Thermal behaviour of water storage devices may be assessed by experimental research or numerically modelling. Numerical simulation requires the numerical resolution of differential mass, momentum and energy conservation equations. Detailed two or three dimensional simulation

allows to know the temperature and velocity fields, without necessity of empirical coefficients. Several authors have reported simulation results of internal convection in hot water tanks in laminar conditions [67], [68], [69]. Numerical simulation of heat transfer and fluid dynamics inside accumulator may requires the use of turbulence models, which increments even more the complexity of the simulation process. These features make two-dimensional models not affordable for a long period of simulation, although they give a lot of detailed information about the process. To simulate the performance of the accumulation tank for long real time periods, one dimensional models are commonly used.

A hot water accumulator subjected to ambient temperature suffers a process of stratification of the fluid in the cooling process [70], due to the cooling that the tank walls produce in a thin layer of fluid adjancent to the wall. Cooler fluid is denser than the bulk fluid, producing a movement of the cooler fluid to the bottom of tank, the fluid adjancent to the wall is then replaced by bulk fluid. In a conventional solar system, stratification is improved with the supply of hot water in the top of tank, proceeding from solar collectors. One-dimensional models cannot reproduce this stratification behaviour, for this reason, certain computational artifices are introduced in these models to provide a good approximation to the actual conditions.

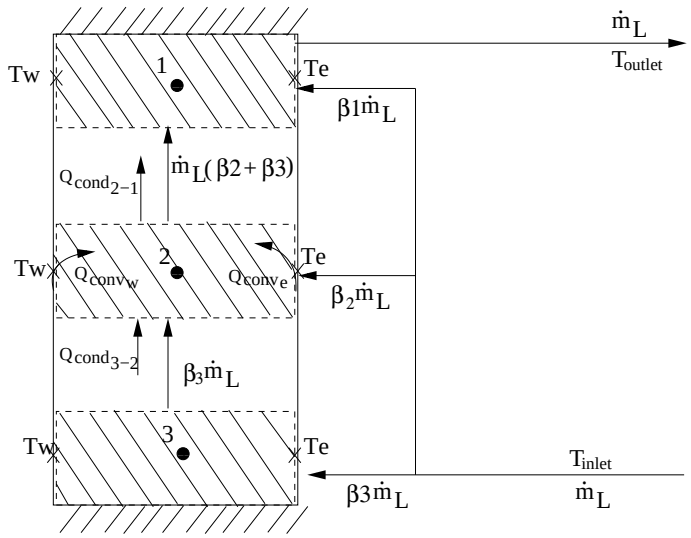

Figure 2.20: Muti-node model used to solve accumulator within the facade

One of these models is commonly known as multi-node model [15]. It consists in

modelling the accumulator with a fixed number of control volumes (N) or segments (known as nodes). The temperature is assumed uniform for each one of these volumes, the degree of stratification is determined by the choice of the number N. In any thermal storage device, stratification depends on the volume of the tank, size, location, design of inlets and outlets and the entering and leaving streams. According to Kleinbach [71] equations of multi-node model require some assumptions about how the hot water entering the tank is distributed to the nodes. For the case of facade-integrated collectors, the classical multi-node formulation is modified since an unique inlet and outlet point is assumed located at bottom and top respectively (no input from the solar collector). The idea is that load will be feed with the hotter top water (minimizing auxiliar heat consumption). The model is schematically shown in Figure 2.20 for a three nodes tank. It has been considered that there are no heat losses through top and bottom areas of the tank. Return water (for the space heating application), or inlet water proceeding from the local network (for the domestic hot water application), will be located at the closest and lower temperature node, by means of a control function within the algorithm calculated at each particular instant. This control function will be $\beta_i = 1$ if returning fluid enters node i, otherwise 0, according to equation 2.113:

$$\beta_i = \begin{cases} 1 & \text{if } i = N \text{ and } T_{inlet} < T_N, \\ 1 & \text{if } T_{i-1} \geq T_{inlet} > T_i, \\ 0 & \text{otherwise} \end{cases} \tag{2.113}$$

For any instant, the net flow between nodes (γ_i) depends on load flow rates and the control function β_i, it represents the net flow into node i from node $i-1$, it is calculated according to expression 2.114.

$$\gamma_i = \begin{cases} 0 & \text{if } i = 1, \\ \dot{m}_L \sum_{j=i}^{N} \beta_j & \text{for } i = 2 \text{ to } N, \\ 0 & \text{if } i = N+1 \end{cases} \tag{2.114}$$

The energy balance in an intermediate node of the tank will be:

$$\rho c_p V_i \frac{T_i - T_i^0}{\Delta\tau} = h_w(T_w - T_i)Sw_i + h_e(T_e - T_i)Se_i + \lambda(T_{i+1} - T_i)S_b/z_i + \\ + \lambda(T_i - T_{i-1})S_t/z_i + \beta_i \dot{m}_L c_p(T_{inlet} - T_i) - \gamma_{i+1} c_p(T_{i+1} - T_i) \tag{2.115}$$

Boundary conditions are given by the bounding temperatures (T_w and T_e) and the heat transfer coeffcients from these surfaces (h_w and h_e):

$$Q_{conv_{westi}} = h_w(T_w - T_i)Sw_i \tag{2.116}$$
$$Q_{conv_{easti}} = h_e(T_e - T_i)Se_i \tag{2.117}$$

When there is no water draw, equation 2.115 becomes reduced, and heat balance will be:

Heat delivered from bounding walls = Heat stored in water

$$h_w(T_w - T_i)Sw_i + h_e(T_e - T_i)Se_i = \rho c_p V_i \frac{T_i - T_i^0}{\Delta\tau} \tag{2.118}$$

Equation 2.115 is solved numerically with a Thomas algorithm [12]. Water thermophysical properties are calculated for each iteration at the mean fluid temperature. Multinode model has the disadvantage that stratification in the accumulator is determined by the choice of the number of nodes, the algorithm requires the combination with computational artifices, such as interchanging the volumes to assure the highest temperature, at any given time, to be located at the top of the tank [72]. However, its results are very proximate to those obtained with a two-dimensional model contrasted experimentally, as reported by Oliveski [67], and it is a suitable methodology to assess the long-term performance of solar water heating systems.

2.9.2 Heat transfer coefficients from bounding walls

Convective heat transfer within accumulation tank has been computed according to empirical expressions of Nusselt number as a function of Rayleigh, taking total height H as length scale. Hsieh and Yang [73] performed experimental studies in a differentially heated water rectangular enclosure with aspect ratios $H/w = 20$ at high Rayleigh numbers. They deduced the following correlations, for aspect ratio $A_H = 20$. For laminar flow regime:

$$Nu = 0.224Ra^{0.257}Pr^{0.056} \qquad 1.54 \times 10^8 \leq Ra \leq 1.58 \times 10^9 \tag{2.119}$$

For turbulent flow regime:

$$Nu = 0.059Ra^{0.315}Pr^{0.056} \qquad 1.58 \times 10^9 \leq Ra \leq 1.48 \times 10^{10} \tag{2.120}$$

Similar correlations were proposed by Seki [74], for laminar flow:

$$Nu = 0.36Ra^{0.25}Pr^{0.051}A_H^{-0.11} \qquad 10^7 < Ra < 10^9 \quad 6 < A_H < 30 \tag{2.121}$$

For turbulent flow:

$$Nu = 0.096 Ra^{0.3} Pr^{0.051} \qquad 10^{10} < Ra < 10^{11} \qquad 6 < A_H < 30 \tag{2.122}$$

According to Hsieh and Yang [73], transition of a boundary layer regime occurs at $Ra = 3 \times 10^9$ to bifurcate the laminar and turbulent flow. In the expression cited above, the overall temperature difference between hot and cold wall of the enclosure is used in Rayleigh determination. Convective heat transfer coefficient is deduced from:

$$Nu = \frac{hH}{k} \tag{2.123}$$

In this work, both expressions were implemented, obtaining similar output results.

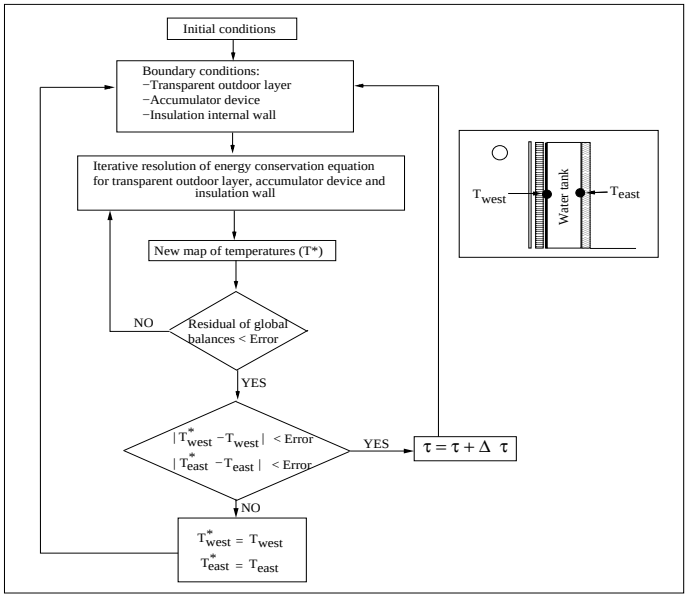

Figure 2.21: Flow chart scheme of the resolution of integrated facades-collectors-accumulators

2.9.3 Insulation model

One dimensional and transient heat conduction is solved through the different layers which form the back of the accumulator by means of an implicit formulation. Thermal properties are considered to remain constant.

$$\frac{\partial T}{\partial \tau} = \frac{k}{\rho c_p} \frac{\partial^2 T}{\partial x^2} \tag{2.124}$$

2.9.4 Algorithm description

The algorithm used to solve the collector-accumulator integrated in the facade is summarized in Figure 2.21. For a given instant, the algorithm consists in an iterative proceeding as follows:

1. Imposition of boundary conditions for transparent outdoor layer (which may include a TIM layer), accumulator device and opaque internal insulation. These conditions correspond to external meteorological data, internal room air and walls temperatures (to account for internal convective and radiative heat exchange).

2. Iterative resolution of energy conservation equations for: i) Transparent outdoor layer (Eq 2.5.1) ii) Accumulator device (Eq. 2.115) iii)Opaque internal insulation (Eq. 2.124) Iterations proceed until the maximum residual and increment of temperatures is lower than a certain value ($1x10^{-6}$).

3. Point 1 is repeated until the change of bounding accumulator temperatures is lower than an imposed error value ($1x10^{-5}$). When this occurs, the global balance of the facade is performed and a new time step is solved.

2.10 Global building algorithm

For each time step, once the indoor and outdoor boundary conditions have been determined, an iterative algorithm begins to solve for the non-linear system of discrete equations governing the problem. Several methods are combined to do so. For the air channel, the step-by-step method (see Section 2.8.4) allows to calculate the velocity, temperature and pressure distributions and the heat flows at each wall.

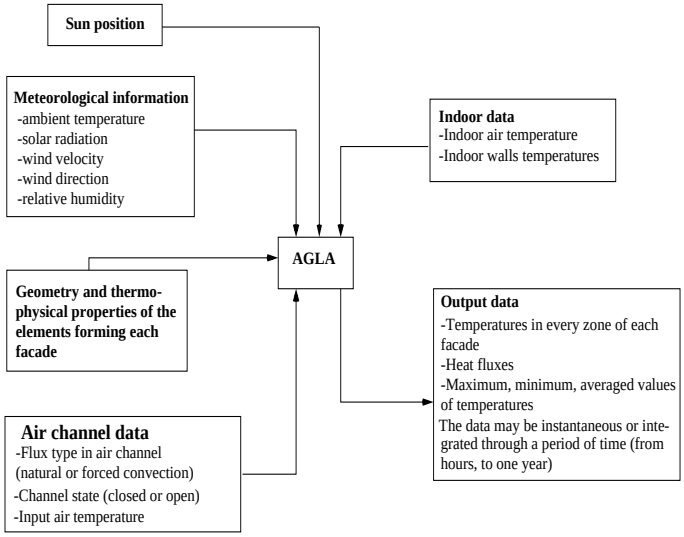

Figure 2.22: Main inputs and outputs of AGLA code

All the zones conforming the facade are coupled by the presence of the air channel, they are solved applying the different algorithms described in previous sections according to their constitution. A number of iterations are carried out before proceeding to the next zone. Once all the zones have been visited, an overall analysis is made of the energy balance. Depending on the imbalance, the iterative process either goes on or the calculation proceeds to the next facade of the building. Figure 2.23 represents the flow diagram of the numerical implementation carried out in the numerical code. Figure 2.22 stands for the main inputs and outputs obtained from a numerical simulation.

2.11 Overall balances

Once the discrete equations for each zone of the facade have been solved for, the global heat fluxes are calculated. Figure 4.3 represents the main heat fluxes and temperatures involved in the global balance of a facade. Table 2.1 gives a description of the acronyms used for the variables involved in the global balance.

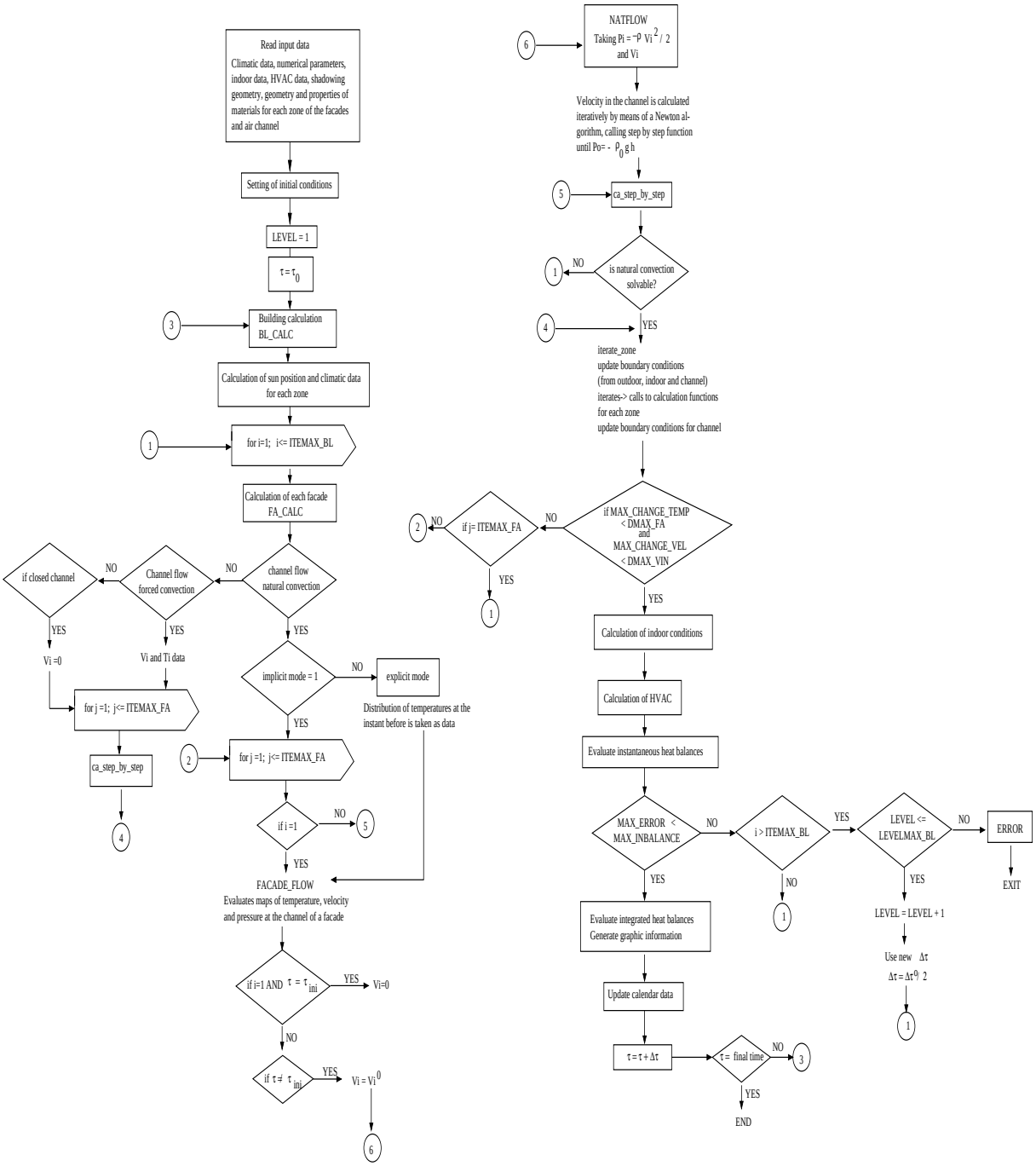

Figure 2.23: Flow diagram of *AGLA* code for the determination of thermal behaviour of advanced facades

Table 2.1: Description of the facade balance variables.

Variable	Description
ISR	Incident Solar Radiation
NSR	Net Solar Radiation (Incident - Reflected)
RSR	Reflected Solar Radiation
TSR	Transmitted Solar Radiation
OTR	Outdoor Thermal Radiation
OCC	Outdoor convective-conductive gains
AEG	Air Enthalpic Gains
ASE	Air Stored Energy
ICC	Indoor convective-conductive gains
ITR	Indoor Thermal Radiation
SSE	Solids Stored Energy
TSE	Total Stored Energy
FOG	Facade Outdoor Gains
FIG	Facade Indoor Gains
PFIG	Positive Facade Indoor Gains
NFIG	Negative Facade Indoor Gains

NSR represents the net solar radiation over the surface of the facade (incident minus reflected), OCC is the outdoor conduction-convection heat flux and OTR is the outdoor thermal radiation. FOG represents the total facade outdoor gains, calculated as

$$FOG = NSR + OCC + OTR \tag{2.125}$$

where

$$NSR = I(1 - R_s) \tag{2.126}$$

$$OCC = h_o(T_a - T_{wo}) \tag{2.127}$$

$$OTR = \epsilon_o(\sigma(F_{f-g}(\epsilon_g T_g^4 + (1-\epsilon_g)T_{sky}^4) + (1 - F_{f-g})T_{sky}^4) - \sigma T_{wo}^4) \tag{2.128}$$

TSE stands for the total stored energy, made up of the energy accumulated in the solid elements of the facade (SSE) and in the air of the channel (ASE)

$$TSE = SSE + ASE \tag{2.129}$$

$$SSE = SSE_{sensible} + SSE_{latent} \tag{2.130}$$

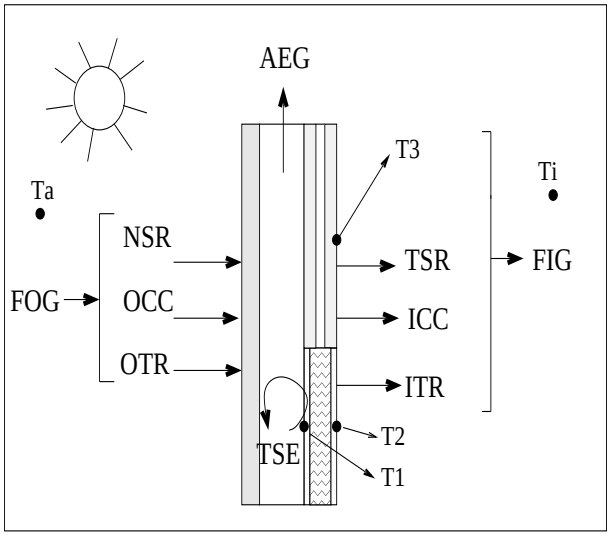

Figure 2.24: Heat fluxes through a standard geometry case

where

$$SSE_{sensible} = \sum_{j=1}^{j=CV} \rho_j c_{pj}((T_j - T_m) - (T_j^0 - T_m))\frac{\Delta x}{\Delta t} \tag{2.131}$$

$$SSE_{latent} = \sum_{j=1}^{j=CV} (\lambda_j \rho_j L - \lambda_j^0 \rho_j^0 L)\frac{\Delta x}{\Delta t} \tag{2.132}$$

and

$$ASE = \sum_{j=1}^{j=CV} (\bar{T_j} - \bar{T_j^0})\frac{w_j \rho_{air} c_p}{\Delta t} \tag{2.133}$$

in which $\bar{T_j}$ is:

$$\bar{T_j} = \frac{(T_{j+1} + T_j)}{2} \tag{2.134}$$

AEG represents the air channel enthalpic gain:

$$AEG = \sum_{j=1}^{j=CV} \dot{m} c_p (T_{j+1} - T_j) \tag{2.135}$$

where c_p is the air specific heat.

TSR stands for the transmitted solar radiation, ICC is the indoor conduction-convection gains and ITR represents the indoor thermal radiation. The following balance must be verified:

$$FIG = TSR + ICC + ITR \tag{2.136}$$

where

$$FIG = I\ T_s + h_i(T_{wi} - T_i) + \epsilon_i\sigma(T_{wi}^4 - T_{walls}^4) \tag{2.137}$$

The global balance of the facade is given by:

$$\begin{aligned} I(1-R_s) + h_o(T_a - T_{wo}) + \epsilon_o(\sigma(F_{f-g}(\epsilon_g T_g^4 + (1-\epsilon_g)T_{sky}^4) + (1-F_{f-g})T_{sky}^4) - \sigma T_{wo}^4) = \\ I\ T_s + h_i(T_{wi} - T_i) + \epsilon_i\sigma(T_{wi}^4 - T_{walls}^4) + \sum_{j=1}^{j=CV} \dot{m}c_p(T_{j+1} - T_j) + \sum_{j=1}^{j=CV} (\bar{T_j} - \bar{T_j^0})\frac{w_j\rho_{air}c_p}{\Delta t} \\ \sum_{j=1}^{j=CV} \rho_j c_{pj}((T_j - T_m) - (T_j^0 - T_m))\frac{\Delta x}{\Delta t} + \sum_{j=1}^{j=CV} (\lambda_j\rho_j L - \lambda_j^0\rho_j^0 L)\frac{\Delta x}{\Delta t} \end{aligned} \tag{2.138}$$

which may be expressed as:

$$FOG = FIG + AEG + TSE \tag{2.139}$$

Thus, the outdoor gains are equal to the indoor gains plus the air enthalpic gains and the total energy stored in the facades. Each one of the above heat flux terms is expressed in W/m^2 in reference to the vertical plane.

All these values can be integrated over the period of simulation (one day, month or year), in the following way:

$$\overline{VAR} = \int_{t=0}^{t=t_{end}} VAR\ \ dt \tag{2.140}$$

Where VAR represents any of the variables mentioned above.

2.11.1 Performance coefficients

Global heat transfer coefficients, such as overall heat transfer coefficient (U_0) and solar heat gain coefficient ($SHGC_0$), are commonly studied to determine the thermal behaviour of facades. Heat transfer through the facade may be determined by:

$$q = U_0(T_a - T_i) + SHGC_0\ I \quad [W/m^2] \tag{2.141}$$

Standard coefficients assume steady state and one-directional heat flow and this can not be directly applied to ventilated facades. Within this thesis, two thermal coefficients are introduced to describe the overall performance of facades. They represent the ratio of net indoor gains, and the ratio of enthalpic gains to the incident solar radiation.

Net internal gains performance coefficient:

$$\eta_i = \frac{\int_{t=0}^{t=t_{end}} [I\ T_s + h_i(T_{wi} - T_i) + \epsilon_i \sigma (T_{wi}^4 - T_{walls}^4)] dt}{\overline{I}} \tag{2.142}$$

Enthalpic gains performance coefficient:

$$\eta_c = \frac{\int_{t=0}^{t=t_{end}} [\sum_{j=1}^{j=CV} \dot{m} c_p (T_{j+1} - T_j)] dt}{\overline{I}} \tag{2.143}$$

In mediterranean climates, the main aim behind using ventilated facades is to reduce indoor gains (avoid overheating). Consequently, a lower η_i value would represent a better facade performance. Since $\overline{FIG}$ is the net heat flux moving indoors, it has both positive and negative components (internal heat gains and heat losses respectively):

$$\overline{FIG} = \overline{PFIG} - \overline{NFIG} \tag{2.144}$$

It is possible to define the indoor gains using a fraction η_{ip}.

Positve internal gains performance coefficient:

$$\eta_{ip} = \frac{\int_{t=0}^{t=t_{end}} \left[I\ T_s + h_i(T_{wi} - T_i) + \epsilon_i \sigma (T_{wi}^4 - T_{walls}^4) \right]^+ dt}{\overline{I}} \tag{2.145}$$

which represents the total heat input inside the building with respect to the total incident solar radiation. In expression 2.145, the $+$ superindex indicates that only positive terms should be taken into account.

2.12 Conclusions

A one-dimensional and transient numerical code for the simulation of double and single skin facades including advanced technological elements, like phase change

materials, transparent insulation and facade integrated collectors-accumulators has been developed. The features of the physic and mathematical models implemented have been described and instantaneous or integrated performance parameters of facade performance have been defined. The main objective of the developed numerical code is to simulate advanced facades in order to assess a long term performance, and to account with a virtual tool to test passive designs.

NOMENCLATURE

A_H	aspect ratio
c_p	specific heat (J kg^{-1} $^\circ K^{-1}$)
g	incoming radiosity
G	incident radiation
h	heat transfer coefficient (W m^{-2} $^\circ K^{-1}$)
H	height (m)
I	solar radiation, radiation intensity
j	outgoing radiosity
k	thermal conductivity (W m^{-1} $^\circ K^{-1}$)
L	latent heat (J kg^{-1})
$\dot{m}$	flow rate (kg s^{-1})
Nu	Nusselt number
P	Pressure(Nw m^{-2})
Pe	Peclet number
Pr	Prandtl number
Q	heat flux (W m^{-2})
Ra	Rayleigh number
R_s	total solar reflectance
S	surface (m^2)
T	temperature
u, v	velocity components (ms^{-1})
V	volume of control volume
w	width (m)
T_s	total solar transmittance
t	time (s)
x	space coordinate (m)
z	control volume height (m)

Greek letters:

α	absorptivity
β	extinction coefficient, $\beta_\eta = \kappa_\eta + \sigma_{s\eta}$
β	fraction of mass flow
Δ	change
ϵ	thermal emissivity
η	spectral band, ratio of gains to incident solar radiation
λ	fluid conductivity (W m$^{-1}K^{-1}$)
γ	mixed flow rate
κ	absorption coefficient
μ	direction cosine of polar angle (cos θ)
ω	associated weight
Ω	solid angle
Φ	phase function
ρ	reflectivity, density (kg m^{-3})
σ	scattering coefficient, Stephan-Boltzmann constant (5.67x10^{-8} W m^{-2}K^{-4})
τ	transmissivity, optical path, shear stress
$\hat{}$	unit vector

Subindexes:

a	ambient
b	black body
c	channel
e	east
f	facade
g	ground
i	index of control volume
inl	inlet
j	index of control volume
L	liquid
m	melting
n	negative component
nl	total number of layers
N	number of directions, total number of points
o	outdoors

out	outlet
p	black plate, positive component
$\vec{q_r}$	radiative heat flux (W m^{-2})
Q	heat flux (W m^{-2})
$\vec{r}$	position
rt	thermal radiation
S	solid, direction coordinate
S_η	source function
SN	number of directions
T, t	temperature (K,C), top
TI_1	air-TIM
w	wall
W	weight factor
$walls$	inner building walls, facing the facade
wi	indoor wall
w	west
wo	outdoor wall

Superindex:

0	value at the previous time
$+$	positive direction
$-$	negative direction
$*$	generic

Acronyms:

$AGLA$	Advanced Glazed Facade Simulation Code
DOM	Discrete Ordinate Method
PCM	Phase Change Material
TDMA	Tri-Diagonal Matrix Algorithm
TIM	Transparent Insulation Material
$SHGC_o$	Overall Solar Heat Gain Coefficient
U_0	Overall Heat Transfer Coefficient

References

[1] D. Saelens. Energy Performance Assessments of Single Storey Multiple-Skin Facades. PhD Thesis. Laboratory for Building Physics, Department of Civil Engineering. Catholic University of Leuven, Belgium, 2002.

[2] A.María León Crespo. History of the Double Skin Facade. In BuildingEnvelopes.org.

[3] P.H. Baker and M. McEvoy. Test cell analysis of the use of a supply air window as a passive solar component. *Solar Energy*, 69(2):113–130, 2000.

[4] X. Fang and Y. Li. Numerical simulation and sensitivity analysis of lattice passive solar heating walls. *Solar Energy*, 69(1):55–66, 2000.

[5] S.N.G. Lo, C.R. Deal, and B. Norton. A school building reclad with thermosyphoning air panels. *Solar Energy*, 52(1):49–58, 1994.

[6] H. Manz, P. W. Egolf, P. Suter, and A. Goetzberger. TIM-PCM External Wall system for solar space heating and daylighting. *Solar Energy*, 61(6):369–379, 1997.

[7] F. Mootz and J.J. Bezian. Numerical study of a ventilated facade panel. *Solar Energy*, 57(1):29–36, 1996.

[8] E. Vartiainen, K. Peippo, and P. Lund. Daylight optimization of multifunctional solar facades. *Solar Energy*, 68(3):223–235, 2000.

[9] M. Costa, O. Aceves, F. Sen, W. Platzer, A. Haller, M. Indetzki, and T. Ojanen. Analysis of multi-functional ventilated facades. an European Joule Project. pages 1–9, 2000.

[10] H. Schweiger, M. Soria, A. Oliva, and M. Costa. A software for the numerical simulation of glazed facades with ventilation channels. In *Proceedings of the Third World Conference in Applied Computational Fluid Dynamics*, volume 27, pages 61–69, 1996.

[11] A. Oliva, M. Costa, C.D. Pérez-Segarra, and R. Alba. Numerical experiments on the thermal behaviour of a trombe wall. In *Proceedings of the ISES Solar World Congress 1993*, volume 6, pages 165–170, 1993.

[12] S. V. Patankar. *Numerical heat transfer and fluid flow*. Hemisphere Publishing Corporation, 1980.

[13] M. Collares-Pereira and A. Rabl. The average distribution of solar radiation: correlations between diffuse and hemispherical and between daily and hourly insolation values. *Solar Energy*, 22:155–164, 1979.

[14] B. Y. H. Liu and R. C. Jordan. Daily insolation on surfaces tilted toward the equator. *ASHRAE Journal*, 3(10 (53)), 1962.

[15] J.A. Duffie and W.A. Beckman. *Solar engineering of thermal processes*. John Wiley and Sons Inc., 1991.

[16] W.M. Rohsenow, J.P. Hartnett, and E.N. Ganic. *Handbook of Heat Transfer Fundamentals*. McGraw-Hill, 1985.

[17] A. Mills. *Heat Transfer*. Irwing, 1992.

[18] D.Faggembauu, M. Costa and M.Soria. AGLA Technical Manual. Centre Tecnològic de Transferència de Calor (CTTC). Universitat Politècnica de Catalunya, 2005.

[19] M. Jakob. *Heat Transfer. Vol 1*. John Wiley and Sons Inc., 1957.

[20] R. Siegel and J.R. Howell. *Thermal radiation heat transfer*. Taylor and Francis, 2001.

[21] H. Schweiger, A. Oliva, M. Costa, and C.D. Pérez-Segarra. Optimisation of total energy transmittance and heat transfer in a solar collector with honeycomb glazing. a numerical study. In *Proceedings of the Sixth International Meeting on Transparent Insulation Technology*, volume 3, pages 66–69, 1993.

[22] A. Ghoneim. Performance optimization of solar collector equipped with different arrangements of square-celled honeycomb. *International Journal of Thermal Sciences*, 44:95–105, 2005.

[23] W.J. Platzer. Directional-hemispherical solar transmittance data for plastic honeycomb-type structures. *Solar Energy*, 49(5):359–369, 1992.

[24] W.J. Platzer. Total Heat Transport Data for Plastic Honeycomb-type structures. *Solar Energy*, 49(5):351–358, 1992.

[25] G. Liersch and F.U. Dill. A ventilated transparent insulation system for wall applications. In *Proceedings of the Sixth International Meeting on Transparent Insulation Technology*, pages 18–21, 1993.

[26] A.K. Athienitis and M. Santamouris. *Themal analysis and Design of Passive Solar Buildings*. James and James, 2002.

[27] N. D. Kaushika and K. Sumathy. Solar transparent insulation materials: a review. *Renewable and Sustainable Energy Reviews*, 7:317–351, 2003.

[28] K.D. Reddy and N.D Kaushika. Comparative study of transparent insulation materials cover systems for integrated-collector-storage solar water heaters. *Solar Energy Materials and Solar Cells*, 58:431–446, 1999.

[29] D. Faggembauu, M. Soria, A. Oliva, and J. Cadafalch. Advanced solar facades with integrated collector-accumulators for domestic hot water and space heating applications. In *Proceedings of the 5th ISES Europe Solar Conference (EUROSUN 2004)*, 2004.

[30] K.G.T. Hollands and K. Iynkaran. Analytical model for the thermal conductance of compound honeycomb transparent insulation, with experimental validation. *Solar Energy*, 51(3):223–227, 1993.

[31] J. E. Y. Hum, K. G. T. Holland, and J. L. Wright. Analytical model for the thermal conductance of double-compound honeycomb transparent insulation, with validation. *Solar Energy*, 76:85–91, 2004.

[32] M.F. Modest. *Radiative heat transfer*. McGraw-Hill, 1993.

[33] S. Chandrasekhar. *Radiative Transfer*. Dover Publications, 1960.

[34] E. Saatdjian. *Transport Phenomena. Equations and Numerical Solutions.* John Wiley and Sons Inc., 2000.

[35] H.Y. Wong. *Heat Transfer for Engineers*. Longman, 1977.

[36] V. Alexiades and A.D. Solomon. *Mathematical Modelling of Melting and Freezing Processes*. Hemisphere Publishing Corporation, 1993.

[37] M. Costa. *Desenvolupament de criteris numèrics per a la resolució de la transferència de calor en medis amb conducció, convecció i canvi de fase sòlid-líquid. Contrastació experimental.* Doctoral thesis. Centre Tecnològic de Transferència de Calor. Universitat Politècnica de Catalunya. 1993.

[38] A. Zöllner, E.R.F. Winter, and R. Viskanta. Experimental studies of combined heat transfer in turbulent mixed convection fluid flows in double-skin-facades. *International Journal of Heat and Mass Transfer*, 45:4401–4408, 2002.

[39] A. Pica, G. Rodonò, and R. Volpes. An experimental investigation on natual convection of air in a vertical channel. *International Journal of Heat and Mass Transfer*, 36(3):611–616, 1993.

[40] J. Xamán, G. Álvarez, L. Lira, and C. Estrada. Numerical study of heat transfer by laminar and turbulent natural convection in tall cavities of facade elements. *Energy and Buildings*, 37:787–794, 2005.

[41] H. Manz. Numerical simulation of heat transfer by natural convection in cavities of facade elements. *Energy and Buildings*, 35:305–311, 2003.

[42] H. Manz. Total solar energy transmittance of glass double facades with free convection. *Energy and Buildings*, 36:127–136, 2004.

[43] J. Cadafalch, A. Oliva, G. Van Der Graaf, and X. Albets. Natural convection in a large, inclined channel with asymmetric heating and surface radiation. *Journal of Heat Transfer*, 125(5):812–820, 2003.

[44] H. Schweiger, A. Oliva, M. Costa, and C.D. Pérez-Segarra. Numerical experiments on laminar natural convection in rectangular cavities with and without honeycomb structures. *International Journal for Numerical Methods for Heat and Fluid Flow*, 5(5):423–443, 1995.

[45] ElSherbiny S.M., Raithby G.D., and Hollands K.G.T. Heat Transfer by Natural Convection Across Vertical and Inclined Air Layers. *Journal of Heat Transfer*, 104:96–102, 1982.

[46] Y. Zhao, Curcija, Dragan, Goss, and P. William. Convective heat transfer correlations for fenestration glazing cavities: A review. *ASHRAE Transactions*, 105(Part 2), 1999.

[47] S. H. Yin, T.Y. Wung, and K. Chen. Natural convection in an air layer enclosed within rectangular cavities. *International Journal of Heat and Mass Transfer*, 21:307–315, 1978.

[48] A. Bar-Cohen and W.M. Rohsenow. Thermally optimum spacing of vertical, natural convection cooled, parallel plates. *Journal of Heat Transfer*, 106:116–123, 1984.

[49] S. Ostrach. Natural Convection in Enclosures. *Journal of Heat Transfer*, 110:1175–1190, 1988.

[50] G. K. Batchelor. Heat Transfer by free convection across a closed cavity between vertical boundaries at different temperatures. *Quarterly Applied Mathematics*, 12:209–233, 1953.

[51] E.R.G. Eckert and W.O. Carlson. Natural Convection in an Air-Layer Enclosed Between Two Vertical Plates with Different Temperatures. *International Journal of Heat and Mass Transfer*, 2:106–120, 1961.

[52] I. Catton. Natural convection in enclosures. In *Proceedings of the 6th International Heat Transfer Conference*, pages 13–31, 1978.

[53] K.G.T. Hollands, Unny T.E., Raithby G.D., and Konicek L. Free Convective Heat Transfer Across Inclined Air Layers. *International Journal of Heat and Mass Transfer*, 98:189–193, 1976.

[54] J. Wright and W Shyy. Numerical simulation of unsteady convective intrusions in a thermohaline stratification. *International Journal of Heat and Mass Transfer*, 39(6):1183–1201, 1996.

[55] J. L. Wright, H. Jin, K.G.T. Hollands, and D. Naylor. Flow visualization of natural convection in a tall, air-filled vertical cavity. *International Journal of Heat and Mass Transfer*, 49:889–904, 2006.

[56] D.C. Wilcox. *Turbulence modeling for CFD*. DCW Industries, Inc. CA, 1998.

[57] M. Soria, F.X. Trias, C.D. Pérez-Segarra, and A. Oliva. Direct numerical simulation of a three-dimensional natural convection flow in a differentially heated cavity of aspect ratio 4. *Numerical Heat Transfer, Part A*, 45:649-673, 2004.

[58] W. Elenbaas. Heat Dissipation of Parallel Plates by Free Convection. *Physica*, 9(1), 1942.

[59] A.G. Fedorov and R. Viskanta. Turbulent natural convection heat transfer in an asymmetrically heated, vertical parallel-plate channel. *International Journal of Heat and Mass Transfer*, 40(16):3849–3860, 1997.

[60] O. Miyatake and T. Fujii. Free convection heat transfer between vertical parallel plates-one plate isothermally heated and the other plate insulated. *Heat Transfer-Japanese Research*, 2(4):30–38, 1973.

[61] W.M. Rohsenow, J.P. Hartnett, and Y.I. Cho. *Handbook of Heat Transfer Fundamentals*. McGraw-Hill, 1998.

[62] G.K. Filonenko. "Hydraulic resistance in pipes", in Heat Exchanger Design Handbook, Teploenergetika, vol. 1. Hemisphere Publishing Corporation, pp. 40-44, 1954.

[63] J. D. Balcomb, R. Jones, C. Kosiewicz, G. Lazarus, R. McFarland, W. Wray, S. C. Kaushik, and M. A. S. Malik. *Passive Solar Design Handbook*. American Solar Energy Society, Inc., 1983.

[64] C. Dharuman, J. H. Arakeri, and K. Srinivasan. Performance evaluation of an integrated solar water heater as an option for building energy conservation. *Energy and Buildings*, 38:214–219, 2006.

[65] R.S. Chauhan and V. Kadambi. Performance of a collector-cum-storage type of solar water heater. *Solar Energy*, 18:327–335, 1976.

[66] D. Faggembauu, M. Costa, and A. Oliva. Advanced Solar Facades with Integrated Collectors-accumulators for domestic hot water and space heating applications (ASFIC). Publishable Final Report. Technical report, 2003.

[67] R.C. Oliveski, A. Krenzinger, and H.A. Vielmo. Cooling of cylindrical vertical tanks submitted to natural internal convection. *International Journal of Heat and Mass Transfer*, 46:2015–2026, 2003.

[68] A. Ivancic, A. Oliva, C.D. Pérez-Segarra, and M. Costa. Heat transfer simulation in vertical cylindrical enclosures for super-critic rayleigh number and arbitrary side-wall conductivity. *International Journal of Heat and Mass Transfer*, 42(2):323–343, 1999.

[69] W. Lin and S.W. Armfield. Direct simulation of natural convection cooling in a vertical circular cylinder. *International Journal of Heat and Mass Transfer*, 42:4117–4130, 1999.

[70] R.C. Oliveski, A. Krenzinger, and H.A. Vielmo. Comparison between models for the simulation of hot water storage tanks. *Solar Energy*, 75:121–134, 2003.

[71] E.M. Kleinbach, W.A. Beckman, and S.A. Klein. Performance study of one-dimensional models for stratified thermal storage tanks. *Solar Energy*, 50(2):155–166, 1993.

[72] R. Franke. Object-oriented modeling of solar heating systems. *Solar Energy*, 60:171–180, 1997.

[73] Shou-Shing Hsieh and Shyh-Shyan Yang. Flow structure and temperature measurements in a 3-D vertical free convective enclosure at high Rayleigh numbers. *International Journal of Heat and Mass Transfer*, 40(6):1467–1480, 1997.

[74] N. Seki, S. Fukusako, and H. Inaba. Visual observation of natural convection flow in a narrow vertical cavity. *Journal of Fluid Mechanics*, 84:695–704, 1978.

Chapter 3

Validation of the numerical code

3.1 Introduction

In this chapter the work carried out to ensure that the code predicts accurately the behaviour of ventilated facades is presented. Recent works define two different steps in this process: verification which consists in checking that the equations describing the phenomena are correctly solved and validation which consists in checking that the models are a suitable representation of the physical process. However, here the term validation is used in a global sense to refer to both.

Thus, the methodology used to validate the code is based on three basic branches:

- Comparison of the results of sub-models with analytical solutions.
- Comparison with reference situations.
- Comparison with experimental results obtained in real-scale test facade facilities in Northern, Central and Southern Europe.

  Each one of these branches will be detailed in the following paragraphs.

3.2 Comparison with analytical solutions

The general heat transfer mathematical models numerically implemented, have no analytical solution for the situations considered in the numerical code. However, the code should be able to reproduce simplified situations with analytical solutions with a good degree of accuracy. To do so, some numerical implementations have been compared with its analytical solution, for the case of phase change materials and transparent insulation.

3.2.1 Phase change materials

The predictions of the PCM model are compared with the analytical solution of the Stefan problem to give an example of a method that uses analytical solutions to validate the results of each sub model. The following simplifying hypothesis are considered: heat transfer is assumed to occur only by conduction, latent heat and phase change temperature are constant, the phases are separated by a sharp inter-phase of zero thickness, thermo-physical properties are assumed to be constant in each phase and density is considered constant (negligible convection within the liquid phase), no internal heating sources are present in the material.

The two-phase Stefan problem on a semi-infinite slab has an explicit solution [2]. In this problem, a semi-infinite slab $0 \leq x < \infty$, initially solid at a uniform temperature $T_S \leq T_m$ is melted by imposing a constant temperature $T_L > T_m$ on the face $x = 0$. Thermophysical properties are all constant.

This problem was solved using $AGLA$ and by imposing null solar and thermal radiation, infinite convective heat transfer coefficients and a large, PCM-impregnated wall to achieve semi-infinite geometry. The case tested took the following data into account: initial temperature $T_o = 25°C$ (solid state), melting temperature $T_m = 32°C$, latent heat $L = 251210J/kg$, $\rho = 1460kg/m^3$, $c_p = 1760J/kgK$, $k = 2.16W/mK$ (equal properties for both phases). The face of the wall was warmed suddenly to a temperature of $T = 90°C$. The analytical solution was obtained using the Neumann similarity solution [3] which gives the interface location and the temperature distribution.

The temperature distribution $T(x,t)$ and the interface funtion $X(t)$ must accomplish the following conditions.

Energy conservation equation in the liquid region:

$$\frac{\partial T}{\partial t} = \frac{k_L}{\rho c_L}\frac{\partial^2 T}{\partial x^2} \qquad 0 < x < X(t) \qquad t > 0. \tag{3.1}$$

Energy conservation equation in the solid region:

$$\frac{\partial T}{\partial t} = \frac{k_S}{\rho c_S}\frac{\partial^2 T}{\partial x^2} \qquad x > X(t) \qquad t > 0. \tag{3.2}$$

Interface temperature:

$$T(X(t),t) = T_m \qquad t > 0. \tag{3.3}$$

Stefan condition:

$$\rho L\frac{dX(t)}{t} = -k_L\frac{\partial T}{\partial x} + k_S\frac{\partial T}{\partial x} \qquad t > 0. \tag{3.4}$$

Boundary conditions:

$$T = T_L > T_m \qquad x = 0 \qquad t > 0, \tag{3.5}$$

$$T = T_m \qquad x = X(t) \qquad t > 0 \qquad \text{interface}, \tag{3.6}$$

$$T = T_S \qquad t = 0 \qquad x \to \infty. \tag{3.7}$$

The interface location is given by:

$$X(t) = 2\lambda\sqrt{\frac{k_L}{\rho c_L}t} \qquad t > 0. \tag{3.8}$$

The temperature in the liquid region is obtained from the following expression:

$$T(x,t) = T_L - (T_L - T_m)\frac{erf\left(\frac{x}{2\sqrt{\alpha_L t}}\right)}{erf(\lambda)} \qquad \text{Liquid region}, \tag{3.9}$$

$$T(x,t) = T_S + (T_m - T_S)\frac{erfc\left(\frac{x}{2\sqrt{\alpha_S t}}\right)}{erfc(\lambda\sqrt{\alpha_L/\alpha_S})} \qquad \text{Solid region}, \tag{3.10}$$

where λ is the solution of the trascendental equation:

$$\lambda\sqrt{\pi} = \frac{St_L}{exp(\lambda^2)erf(\lambda)} - \frac{St_S}{\sqrt{\frac{\alpha_L}{\alpha_S}}exp(\frac{\alpha_L}{\alpha_S}\lambda^2)erfc(\sqrt{\frac{\alpha_L}{\alpha_S}}\lambda)} \tag{3.11}$$

and

$$St_L = \frac{c_L(T_L - T_m)}{L} \qquad St_S = \frac{c_S(T_m - T_S)}{L} \tag{3.12}$$

$$\alpha_L = \frac{k_L}{\rho c_L} \qquad \alpha_S = \frac{k_S}{\rho c_S}. \tag{3.13}$$

The evolution of the temperature for three different instants as a function of the position (x) is shown in Figure 3.1(a) and as a function of time in Figure 3.1(b). A mesh of 400 control volumes, in a ten-metre-long slab, was used.

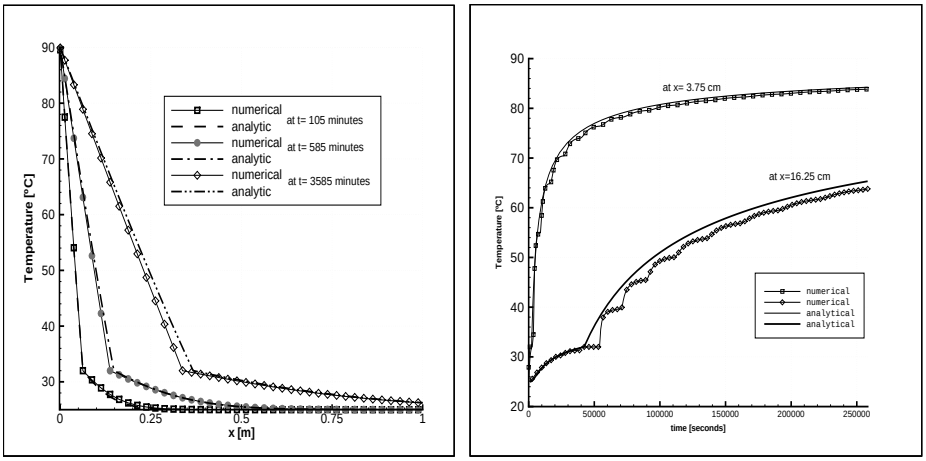

(a) (b)

Figure 3.1: Analytical and numerical comparison of the evolution of the temperature of a semi-infinite solid PCM wall initially at 25 $^{\circ}C$ and exposed suddenly to a temperature of 90 $^{\circ}C$ at $x = 0$.

The change in the slope of the temperature at T_m can be noted at the location of the interface. After approximately 60 hours, the interface front was at 0.35 meters. In Figure 3.1(b) it is observed that the phase change duration is slightly larger at $x = 0.1625$m for the numerical solution. As expected, there was a good agreement between the numeric and analytic solutions. The errors tended towards zero as the mesh size and time increment was refined.

3.2.2 Transparent insulation materials

As discussed in Section 2.6, there are very few exact analytical solutions of general radiation transfer equation 2.11 and they are limited to simple situations. Even in these cases, the analytical final expression normally needs to be evaluated numerically, because of its mathematical complexity. The simplest case is constituted by a one-dimensional plane-parallel grey medium at radiative equilibrium (radiation is the only heat transfer mode present) or with a known temperature field. This is a very useful situation to test numerical solutions.

Heaslet and Warming [4], [5] were the first who originally solved analytically radiative heat transfer through a grey plane parallel medium. This case is addressed in detail in [6]. The main hypothesis are that the plates are assumed isothermal

and isotropic (thermal properties and temperatures do not vary across each plate). Medium radiative properties show directional dependence on polar angle θ but not on azimuthal angle ψ (azimuthal symmetry). Temperature and radiative properties of the medium vary only in the direction perpendicular to the plates. This means that radiative source and radiative intensity both depend only on a single space coordinate plus a single direction coordinate.

The case with no-scattering has been analysed considering black and grey bounding surfaces (diffuse emitter and reflector). The problem is reduced to solve the following expressions for the non-dimensional temperatures $\Phi_b(\tau)$ and heat fluxes $\psi_b(\tau)$:

$$\Phi_b(\tau) = \frac{1}{2}E_2(\tau) + \frac{1}{2}\int_0^{\tau_L} \Phi_b(\tau')E_1(|\tau - \tau'|)d\tau' \tag{3.14}$$

$$\psi_b = 1 - 2\int_0^{\tau_L} \Phi_b(\tau')E_2(\tau')d\tau' \tag{3.15}$$

Non-dimensional temperature is defined as:

$$\Phi(\tau) = \frac{T^4(\tau) - T_2^4}{T_1^4 - T_2^4} = \frac{\Phi_b(\tau) + (1/\epsilon_{t2} - 1)\psi_b}{1 + \psi_b(1/\epsilon_{t1} + 1/\epsilon_{t2} - 2)} \tag{3.16}$$

and non-dimensional heat flux is:

$$\psi = \frac{q}{\sigma(T_1^4 - T_2^4)} = \frac{\psi_b}{1 + \psi_b(1/\epsilon_{t1} + 1/\epsilon_{t2} - 2)} \tag{3.17}$$

Subscripts 1 and 2 refer to the limiting walls. As stated by Coelho [7], both $\Phi_b(\tau)$ and ψ_b are independent of the emissivity and temperature of the walls. Moreover, $\Phi(\tau)$ and ψ depend only on the emissivity of the walls. In the case of black walls, $\Phi(\tau) = \Phi_b(\tau)$ and $\psi = \psi_b$.

The numerical prediction of non-dimensional temperature field is shown in Figure 3.2 for a range of optical thicknesses, as a function of the distance x between the walls. L is the total width of the medium. The calculations were carried out with a grid of 24 nodes. It is observed that the gradient of temperatures becomes smaller as the optical thickness decreases. In the limit case of transparent medium ($\tau_L = 0$), temperature of the medium would be constant ($\Phi_b = 0.5$), and the temperature would be the semi sum of the walls temperatures, in case of $\tau_L \to \infty$ the non-dimensional temperature would decrease from 1 at $x = 0$ to 0 at $x = L$.

Since in this case radiative equilibrium prevails $dq/d\tau = 0$, the heat flux does not vary across the medium. Non-dimensional heat fluxes are given in Table 3.1 for different optical thicknesses.

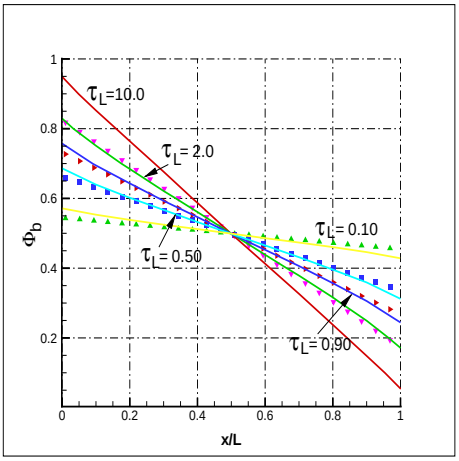

Figure 3.2: Non-dimensional temperature prediction for different values of optical thickness. Continuous lines are the analytical solutions for each optical thickness, as published by Heaslet and Warming [5]. Points represent numerical solutions.

Table 3.1: Non-dimensional heat flux ψ_b for radiative equilibrium between parallel black plates. Exact solution from Heaslet and Warming [4]. Numerical solution from $AGLA$ with DOM method for two grids: 24 and 48 nodes. Error computed as absolute relative error.

Optical thickness τ_L	$\psi_b AGLA$ 24 nodes	$\psi_b AGLA$ 48 nodes	Exact	Absolute error 24 nodes	Absolute error 48 nodes
0.00	1.000	1.000	1.0000	$5.50\,x10^{-5}$	$1.85\,x10^{-6}$
0.10	0.898	0.903	0.9157	$1.90\,x10^{-2}$	$1.40\,x10^{-2}$
0.20	0.821	0.823	0.8491	$3.34\,x10^{-2}$	$3.11\,x10^{-2}$
0.30	0.756	0.759	0.7934	$4.76\,x10^{-2}$	$4.30\,x10^{-2}$
0.40	0.700	0.704	0.7458	$6.14\,x10^{-2}$	$5.57\,x10^{-2}$
0.50	0.652	0.657	0.7040	$7.37\,x10^{-2}$	$6.72\,x10^{-2}$
0.60	0.610	0.615	0.6672	$8.54\,x10^{-2}$	$7.81\,x10^{-2}$
0.80	0.541	0.546	0.6046	$1.05\,x10^{-1}$	$9.71\,x10^{-2}$
1.00	0.486	0.491	0.5532	$1.22\,x10^{-1}$	$1.13\,x10^{-1}$
1.50	0.387	0.392	0.4572	$1.54\,x10^{-1}$	$1.43\,x10^{-1}$
2.00	0.322	0.326	0.3900	$1.76\,x10^{-1}$	$1.64\,x10^{-1}$

2.50	0.275	0.279	0.3401	$1.91\,\text{x}10^{-1}$	$1.79\,\text{x}10^{-1}$
3.00	0.216	0.220	0.3016	$2.85\,\text{x}10^{-1}$	$2.71\,\text{x}10^{-1}$
5.00	0.143	0.146	0.2077	$3.10\,\text{x}10^{-1}$	$2.96\,\text{x}10^{-1}$

For the case in which the walls are not black, but are gray, diffuse emitters and reflectors, the results obtained for different combinations of wall emissivities are shown in Table 3.2 for different optical thicknesses. Both tables show a good agreement between the numerical results and the exact solution.

Table 3.2: Non-dimensional radiative heat flux ψ for radiative equilibrium between parallel plates with different thermal emissivities. Exact solution from Heaslet and Warming [4]. Numerical solution from $AGLA$ with DOM method for a grid of 24 nodes.

ϵ_{t1}	ϵ_{t2}	τ_L	$\psi AGLA$	Exact	Absolute error
0.8	1	0.1	0.7340	0.7451	$1.49\,\text{x}10^{-2}$
		0.5	0.5693	0.5986	$4.90\,\text{x}10^{-2}$
		1	0.4483	0.4860	$7.77\,\text{x}10^{-2}$
		5	0.1634	0.1975	$1.73\,\text{x}10^{-1}$
0.8	0.5	0.1	0.4218	0.4270	$1.21\,\text{x}10^{-2}$
		0.5	0.3618	0.3745	$3.39\,\text{x}10^{-2}$
		1	0.3089	0.3271	$5.58\,\text{x}10^{-2}$
		5	0.1383	0.1649	$1.61\,\text{x}10^{-1}$
0.8	0.1	0.1	0.0959	0.0967	$8.28\,\text{x}10^{-3}$
		0.5	0.0924	0.0937	$1.37\,\text{x}10^{-2}$
		1	0.0885	0.0904	$2.06\,\text{x}10^{-2}$
		5	0.0619	0.0711	$1.29\,\text{x}10^{-1}$

3.3 Comparison with reference situations

3.3.1 One-dimensional performance parameters

Another step to validate the numerical implementations, has consisted in compare the heat fluxes predicted numerically, with those obtained from the application of standard performance coefficients of fixed architectonic elements in specific conditions. According to ASHRAE [8], for a given temperature difference, the values of the Center-of-Glass overall heat transfer coefficient U_0 Factor and the overall solar heat gain coefficient $SHGC_0$ at normal incidence are tabulated for different facade compositions. These coefficients were calculated by imposing constant conditions for the indoor and outdoor air temperatures and the solar radiation. The steady

indoor heat flux can be computed as:

$$q = U_0(T_a - T_i) + SHGC_0\ I \quad [W/m^2] \tag{3.18}$$

U_0 coefficients were calculated by keeping to the numerical code conditions for winter based on ASHRAE data: outdoor temperature $T_a = -18°$C, indoor air temperature $T_i = 21°$C and null solar radiation. The outdoor convective heat transfer coefficient was taken to be h_0 = 29 W/m^{2}K, which corresponds to a 24 km/h wind velocity and an indoor coefficient of h_i = 8.29 W/m^{2}K. All the glass layers were 3.2 mm wide, and corresponded to the features of a standard reference glazing unit (τ = 0.86, ρ = 0.08, α = 0.06 at normal incidence). When considering multi-layered glazing units, each layer corresponds to standard reference glazing with an air gap of 12.7 mm.

In order to calculate $SHGC_0$, the indoor and outdoor temperatures were equalised and a constant solar radiation, $I = 800W/m^2$, was assumed. The solar heat gain coefficient was calculated as:

$$SHGC_0 = \frac{q}{I} \tag{3.19}$$

The standard subroutines implemented in $AGLA$ were used to address the heat fluxes that occurred in the facade. Tabulated coefficients were compared with the quantities predicted by the numerical code in Table 3.3.

Table 3.3: U_0 (W/m^2 K) and $SHGC_0$ Factors

CASE	ASHRAE		*AGLA*	
	U_0	$SHGC_0$	U_0	$SHGC_0$
Single clear glass	5.91	0.86	6.3	0.87
Double glazing	2.73	0.75	2.79	0.78
Double glazing, ϵ = 0.2 on Surface 2	1.99	0.65	1.91	0.78
Triple glazing	1.76	0.67	1.81	0.71
20 cm brick (k = 1.21) plus 10 cm of polystyrene (k = 0.029)	0.26	0.015	0.26	0.015

In the case of multi-glazing systems, ordinary uncoated glass with a emittance of 0.84 was considered. The case of double glazing with reduced emissivity on surface 2 does not produce changes in $SHGC_0$ values and the low emissivity is associated with a reduction in the value of U_0.

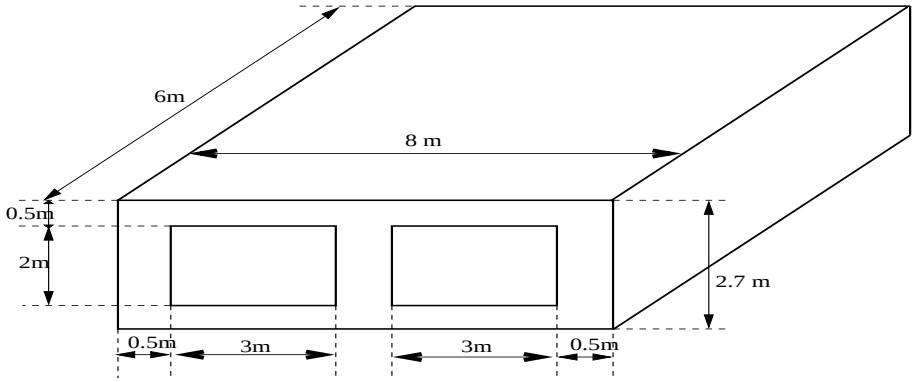

Figure 3.3: Basic geometry to test building codes within BESTEST

3.3.2 Building Energy Simulation Test (BESTEST)

The International Energy Agency has supported a project to help validating building energy simulation programs called the IEA Building Energy Simulation Test (BESTEST) and Diagnostic Method produced at the National Renewable Energy Laboratory [10]. This testing procedure allows a user to compare the results of any building simulation program against the average results of several "reference" programs for a series of tests, primarily related to the building envelope. The test cases are not representative of a realistic building. They are designed to isolate individual aspects of building energy dynamic simulation. In a real building, the individual tested effects would interact making it difficult to determine the cause of any errors. The numerical analysis is carried out over a given "shoe box" geometry, with specific meteorological data and thermo-physical properties. The tests are designed to evaluate a range of model effects like thermal mass, direct gain solar systems, shading devices, internal gains, infiltration rates and thermostat control, among others. The basic structure is modified by adding transparent layers with different orientations, changing the wall properties, adding shading, etc. There are eight programs which were originally used to conduct these tests. These programs were ESP, BLAST, DOE2, SRES/SUN, SERIRES, S3PAS, TRNSYS and TASE. The recorded results for these programs include the total annual heating and cooling load for each test as well as the maximum heating and cooling demands along with the time at which they occurred in the year.

We have adapted some of the tests designed within BESTEST to test $AGLA$ [9]. All the cases described in the procedure were not originally foreseen in the numerical

code, some features were adopted as implemented in $AGLA$ without modification, such as the heat transfer superficial coefficients which are not considered constant but they are instantaneously calculated. The tested cases have been the low mass series 195 to 300. The features of these tests are described in [10].

Table 3.4 shows the comparative results of the annual and peak heating load of the performed tests. In this Table, the cases denoted with the letter 'b' are the obtained as mean of the different code predictions.

Table 3.4: Annual and peak heating load of the tested cases. Cases denoted with 'b' are the mean of the different code predictions. Cases denoted only by a number are the predicted by $AGLA$.

Case	Heating load [MW-h]	Peak heating load [kW]
195	4.3506	2.1049
195b	4.9990	2.2249
200	6.2855	3.2845
200b	6.4010	3.0036
210	6.2626	3.3188
210b	6.6780	3.0128
215	9.2646	4.5871
215b	7.0730	3.2961
220	9.4241	4.6798
220b	7.6660	3.4025
230	12.9051	6.2184
230b	11.1850	5.0117
240	8.1444	4.4798
240b	6.3960	3.2145
250	7.6552	4.6798
250b	6.0310	3.4020
270	5.2077	3.3186
270b	5.2070	3.4197
280	5.9125	3.3186
280b	5.4810	3.4197
290	5.2118	3.3186
290b	5.2600	3.4185
300	5.1465	3.2920
300b	5.4380	3.4837

The instant of the peak heating load agrees among the cases tested. The annual transmitted solar radiation for different facade orientations and the rate between transmitted and incident radiation has been also compared. The predicted numerical values fall within the acceptable range for each test.

3.4 Comparison with experimental results

The results predicted by the numerical code were compared with experimental data obtained from ad-hoc built experimental set-ups in the framework of a European Joule Project [11], [12]. Within the scope of this project, several modular facades that had different features suitable for each climatic condition (North, Central and South of Europe) were studied. The project involved eight double-skin facade prototypes, which incorporated honeycomb-type transparent insulation, phase change materials and partially opaque inner areas. Temperatures at different surfaces, heat fluxes and flow rates were measured in several modules. Those measurements were carried out over different periods of time and climatic conditions, and even addressed various work regimes for the facade(closed, open channel, forced and natural convection).

The constructive and measurement treatments are described in detail in [13] and [11]. In all the cases, measured boundary conditions such as meteorological data, including solar radiation impinging on the facade surface and ambient temperatures were used to feed the numerical code.

The main difficulties that arose from the experimental validation were associated with the following uncertainties and limitations:

- Evaluation of heat transfer coefficients for the air channel and indoor and outdoor surfaces.
- Non-constant channel sections.
- The one dimensional models

A good degree of agreement can be observed between the final numerical and experimental results, in spite of the presence of the aforementioned uncertainties. The agreement was quantified by using the root mean square parameter (ϵ_{rms}), which is given as:

$$\epsilon_{rms} = \sqrt{\frac{1}{N}\sum_{i=1}^{N}(\frac{n_i - e_i}{e_i})^2} \tag{3.20}$$

where N is the total number of points analysed, and e_i and n_i represent, respectively, the values obtained experimentally and numerically. The results obtained

from the experimental validation in which ϵ_{rms} fell within the range 0.014 to 0.11 allow one to conclude that despite the uncertainties mentioned above, the accuracy of the models is sufficient and that they can be used to simulate the thermal behaviour of ventilated facades.

3.4.1 Comparison with experimental results from the Southern Europe test site

The numerical results for a modular facade with a partially opaque inner area (as in Figure 3.4(a)) were compared with experimental data in Figures 3.5 and 3.6 in the case of closed channel. Figure 3.4(b) shows a general view of the prototye analyzed.

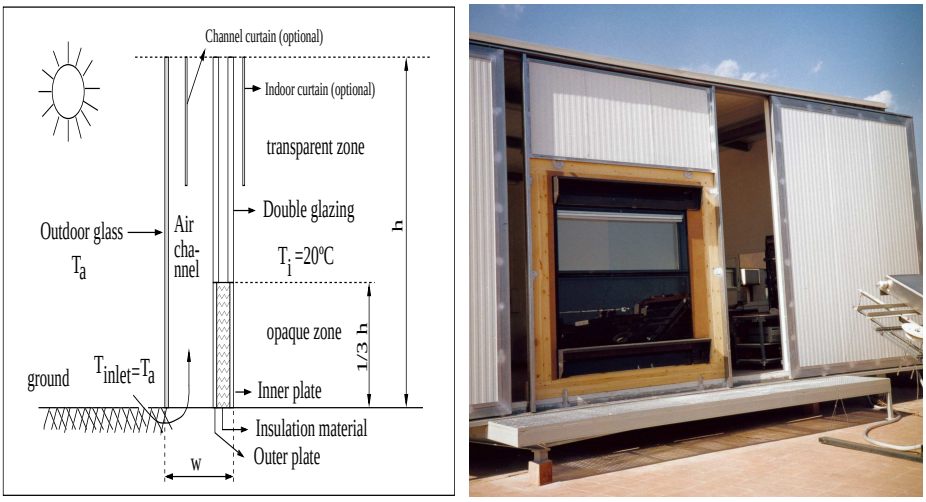

(a) (b)

Figure 3.4: South prototype: a)Schematic geometry of the module for the southern Europe climate. It is formed by an external glass and an internal layer constituted by a double-glazed area at the top and an opaque zone at bottom. b)General view of the prototype tested for southern Europe climatic conditions, mounted in CTTC installations at the Universitat Politcnica de Catalunya.

Figure 3.5 represents the temperature of the inner opaque surface of the channel and Figure 3.6 represents the temperature of the internal opaque wall at the indoor surface.

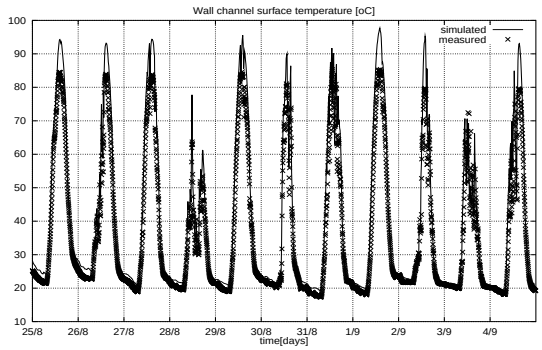

Figure 3.5: Surface temperature of the opaque indoor wall of a double-skin prototype facade facing air channel. Closed air channel. Experimental data obtained by Costa et al. [13] and [11]. $\epsilon_{rms} = 0.11$

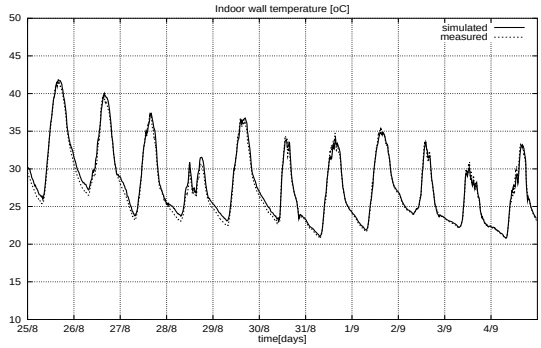

Figure 3.6: Indoor surface temperature of the opaque indoor wall of a double-skin prototype facade. Closed air channel. Experimental data obtained by Costa et al. [13] and [11]. $\epsilon_{rms} = 0.018$

3.4.2 Comparison with experimental results of the Northern Europe test-site

A double-skin prototype formed by an external opaque layer and an internal opaque wood frame wall, as schematically shown in Figure 3.7, was tested experimentally by Ojanen [14]. The ventilation air flow rate was maintained constant and measured continuously during the test periods. Numerical data obtained from the simulation

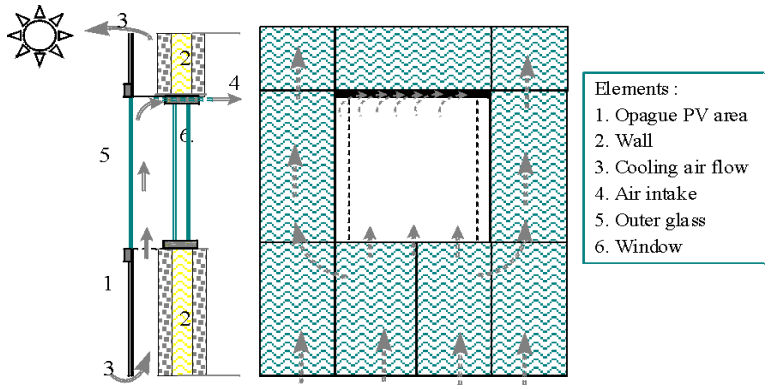

Figure 3.7: Schematic design of the double skin prototype tested in northern european conditions, by VTT Technical Research Centre of Finland, Espoo.

of these prototypes were compared with experimental data. Some of the results of these comparisons are shown in Figures 3.8, 3.9 and 3.10, which represent temperatures and heat fluxes at different surfaces and time periods.

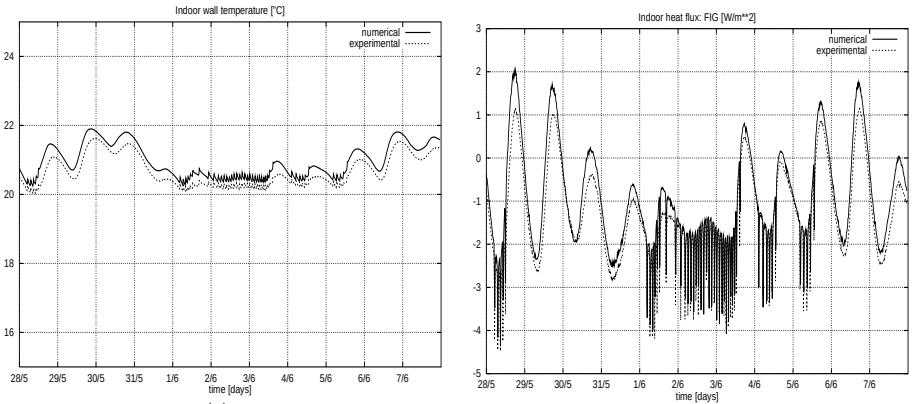

Figure 3.8: Experimental and numerical data for the northern prototype: a)Indoor surface temperature of the opaque indoor wall $\epsilon_{rms} = 0.014$; b)Indoor heat flux $\epsilon_{rms} = 0.011$. Open-air channel with forced convection. Experimental data obtained by Ojanen [14].

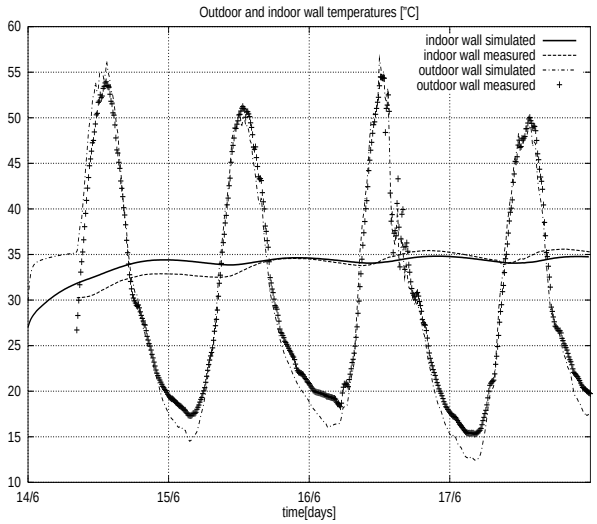

Figure 3.9: Experimental and numerical data for the northern prototype: Outdoor and indoor surface wall temperatures. Experimental data obtained by Ojanen [14].

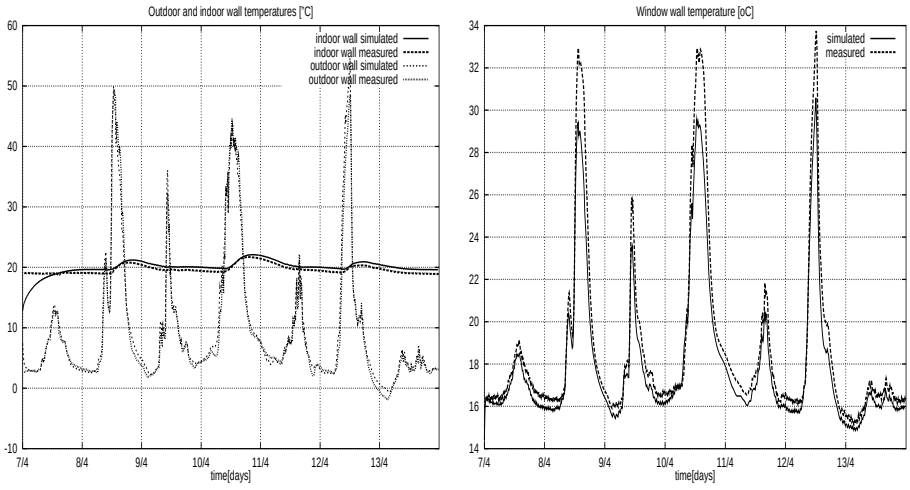

Figure 3.10: Experimental and numerical data for the northern prototype: a) Outdoor and indoor surface wall temperatures; b) Window internal surface temperature. Experimental data obtained by Ojanen [14].

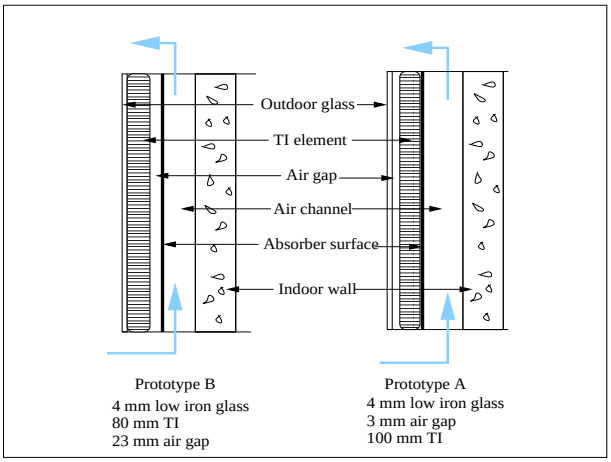

Figure 3.11: Scheme of prototypes measured in real climatic conditions to validate numerical code

3.4.3 Experimental validation of facades modules including transparent insulation

The prototypes tested are a double skin module formed by an outdoor layer made of glass, TIM wall, and an absorber, as indicated in Figure 3.11. The internal layer was constituted by a 24cm indoor wall. An air channel separates both layers. Air channel may work with closed inlet and outlet gaps (as a thermal enclosure). Furthermore, in the case of opened gaps, external air circulates through the channel induced by natural convection.

This facade design was initially conceived for the renovation of buildings, including an external TIM wall which would produce both a combination of insulation plus convective additional air gains (through the facade channel).

The experimental facility and data are described in [15] and [16]. Two prototypes (Figure 3.11) were equipped with two types of absorber surfaces and in one case an air gap between absorber and TIM was included (Prototype B). These prototypes were tested in actual outdoor climatic conditions corresponding to Freiburg city. Figure 3.12 shows the values of ambient air temperature and incident solar radiation measured for a succession of days. Meteorological data and temperatures at different zones of the prototypes were measured. They were compared with the numerical data obtained running the numerical code with the same meteorological input data. Some of the results are shown in Figures 3.13 and 3.14.

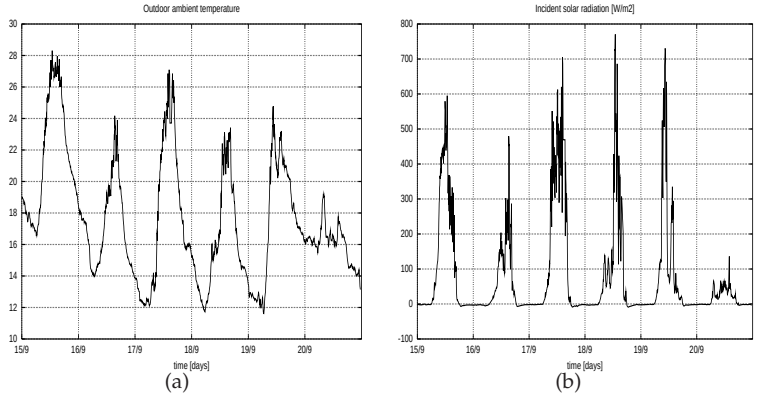

Figure 3.12: Ambient air temperature and incident solar radiation measured over modules surface from September 15th to 20th

Figure 3.13 shows the values of temperatures in different surfaces of the facade. The configuration of the facade corresponds to prototype A (Figure 3.11) with 4mm glass, 3mm air gap, 100 mm TIM and an absorber surface constituted by fibre cement plate ($\alpha_s = 0.72$, $\epsilon_t = 0.90$). Figure 3.13(a) shows the temperature of absorber surface for a succession of six days, in a case with the air channel closed. Figure 3.13(b) shows the temperature of the indoor wall (internal surface of internal skin). In Figures 3.13(b), 3.13(c) and 3.13(d), the dotted curve corresponds to the numerical prediction, it has been compared with several values of measured temperatures which were acquired at different positions. In Figure 3.13(c) the values of indoor wall temperature (at the surface limiting the air channel) are shown. Figure 3.13(d) shows the absorber surface temperature, in the case with the air channel opened and with external air circulation.

Figure 3.14(a) shows the temperatures of the indoor wall (at the surface limiting the air channel) for the case with the air channel opened. Figures 3.14(b), 3.14(c) and 3.14(d) correspond to the prototype B (Figure 3.11) with 4mm glass, 80 mm TIM, 23 mm air gap and an absorber selective surface ($\alpha_s = 0.95$, $\epsilon_t = 0.10$ and 0.42 in the opposite surface.) Figures 3.14(b) and 3.14(c) show the values of absorber temperature, and indoor wall surface temperature (at the surface limiting the channel) for the case with the air channel closed. Figure 3.14(d) shows the temperature of the internal surface of the indoor wall in the case when the air channel is opened.

For the cases in which several experimental measures are shown, the root mean square is the mean value obtained from the comparison of the numerical prediction

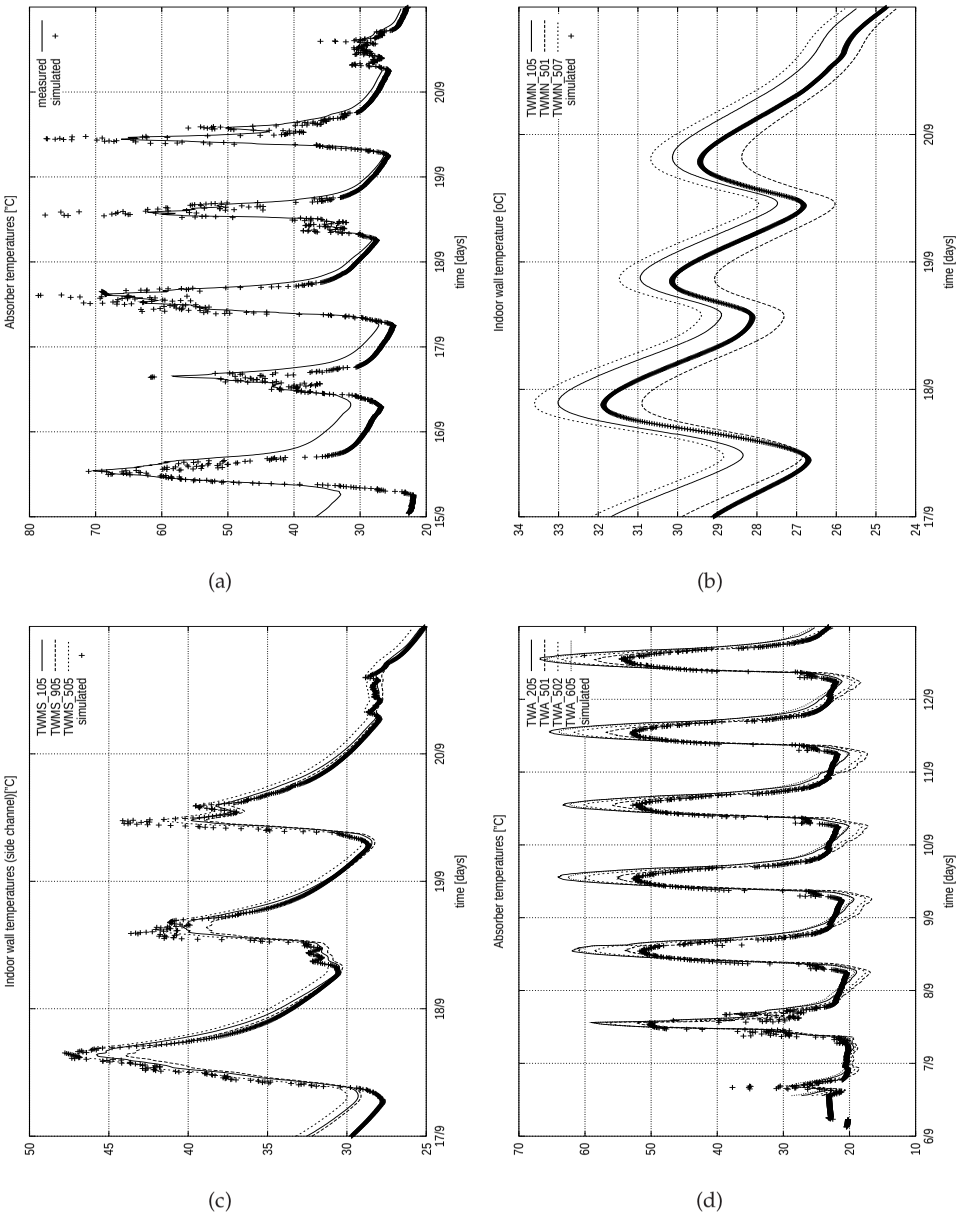

Figure 3.13: Surfaces temperatures at modular prototype A. a)Absorber surface temperature with closed air channel, $\epsilon_{rms} = 0.13$; b)Indoor wall surface temperature with closed air channel, $\epsilon_{rms} = 0.09$; c)Indoor wall temperature in the surface facing channel, closed channel, $\epsilon_{rms} = 0.11$; d)Absorber surface temperature with opened air channel, $\epsilon_{rms} = 0.14$

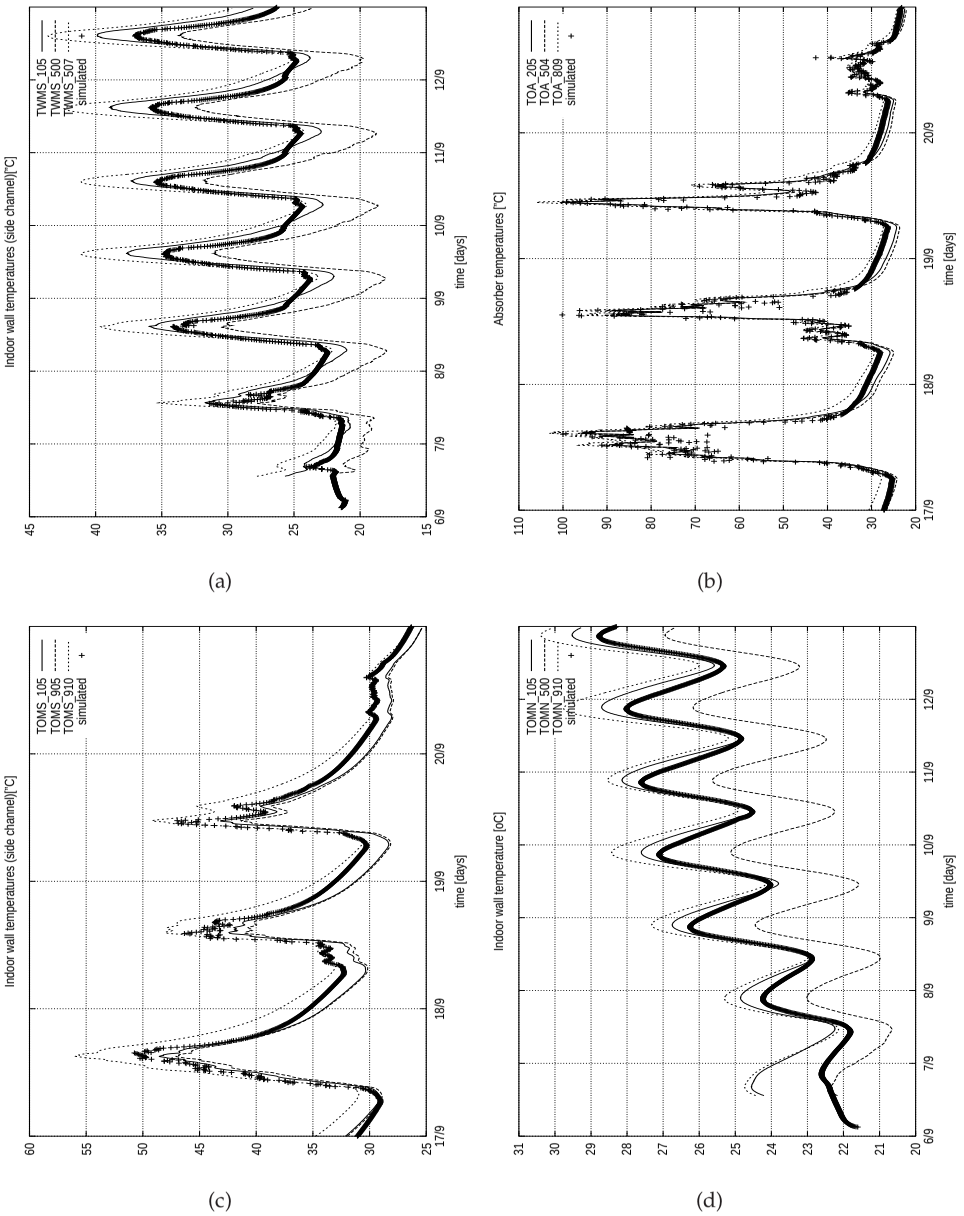

Figure 3.14: a-Indoor wall temperature in the surface facing channel for the case with opened channel,$\epsilon_{rms} = 0.11$; b-Absorber surface temperature with closed air channel for the prototype B, $\epsilon_{rms} = 0.12$; c-Indoor wall temperature in the surface facing channel,closed channel for prototype B, $\epsilon_{rms} = 0.11$; d-Indoor wall surface temperature, opened channel for prototype B, $\epsilon_{rms} = 0.05$

with each experimental curve. The model predicts accurately the behaviour during day and night. Thermal peaks, which are produced in accordance with the solar radiation peaks are correctly foreseen. Temperatures measured at different positions on a surface show a two-dimensional behaviour, numerical prediction falls among the several experimental values, which indicates that the one-dimensional approximation produces an acceptable prediction of the actual-multidimensional measured behaviour. It should be remarked that this comparison does not only validate the use of transparent insulation in the facade, but also the natural convection flow induced in channel which is approximated with a one-dimensional model as described in chapter 2 [17].

In the results obtained from the experimental validation, the errors (ϵ_{rms}) have fallen within the range from 0.05 to 0.14. These results together with the verification of the numerical reproduction of analytical known solutions allow to conclude that the accuracy of the numerical models is sufficient to permit a long-term prediction of thermal behaviour of facades containing transparent insulation materials.

3.4.4 Experimental results for facade-integrated collector-accumulator

A facade-integrated solar collector was built and tested in different facades with double and single skin. It was installed in the solar test cell facility of the Centre Tecnològic de Transferència de Calor, as it is shown in Figure 3.15.

(a) (b) (c)

Figure 3.15: Pictures of collector-integrated facade a)Mounted collector-accumulator; b)Inside view from complete prototype; c)Outside view

In the case of a double facade, the collector-accumulator was part of the internal skin. In the single skin case, the same facade was tested without the external glass.

Figure 3.16 shows a scheme of the prototype tested.

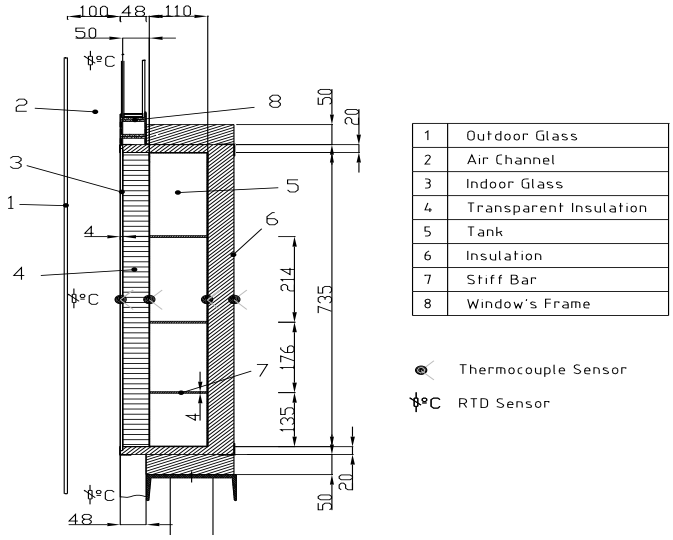

Figure 3.16: Schematic design of the collector-accumulator integrated in the facade.

The experimental set-up was equipped with thermocouples to measure temperatures at different facade zones, as schematically shown in Figure 3.17. Meteorological conditions were also recorded. Experimental work covered a period of approximately one year to test both facade designs (double and single skin). Both cases were considered with transparent insulation between glass and absorber surface. No water draw was considered in the cases shown here.

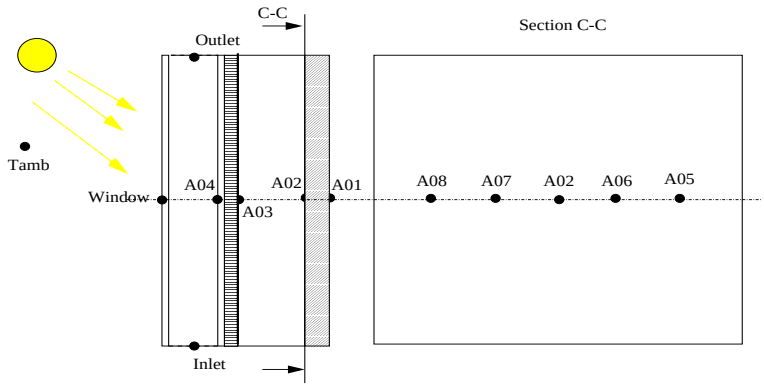

Figure 3.17: Schematic view of the position of thermocouples in prototype

Comparison of experimental and numerical results

The prototype is formed by an external layer made of glass, and an internal layer constituted by glass, transparent insulation (TIM), an absorber surface, a water accumulator (a tank), and insulation. The air channel between both layers was kept closed during these tests. The following sensors have been used:

- A01 : Temperature at the indoor wall surface
- A02 : Temperature at the surface of the tank, at the indoor side (see Figure 3.17)
- A03 : Temperature at the surface of the tank, at the outdoor side (see Figure 3.17), it is the absorber temperature.
- A04 : Temperature of the indoor glass, which is in contact with the transparent insulation.
- Window outdoor surface temperature: Temperature of the outdoor external glass

Some illustrative results of the validation process are shown in Figures 3.18, 3.19, 3.20, 3.21, 3.22 and 3.23. In this first stage, only punctual measurements of water temperature were carried out, in order to prepare the following stage of experimentation.

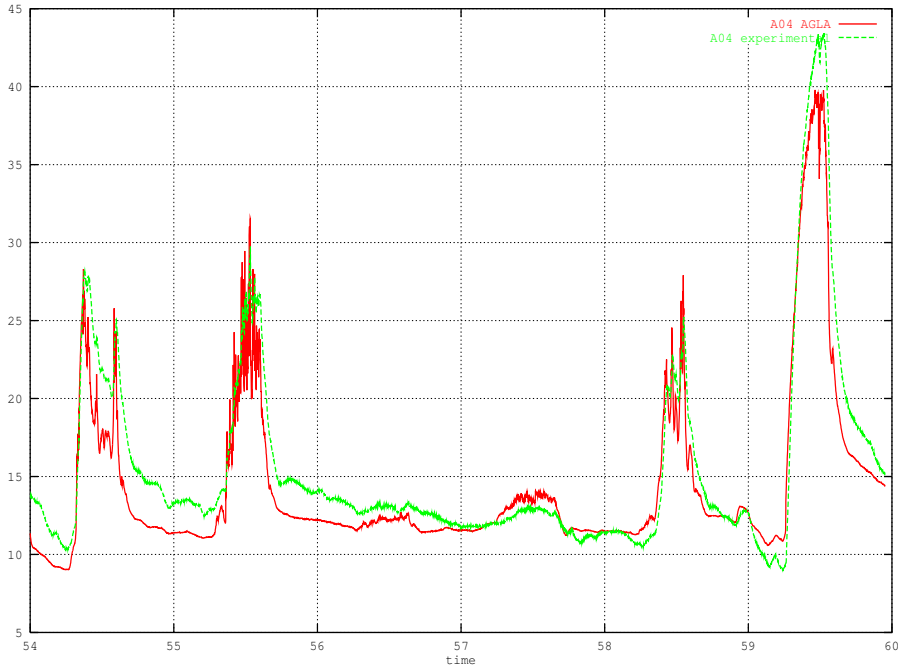

(a)

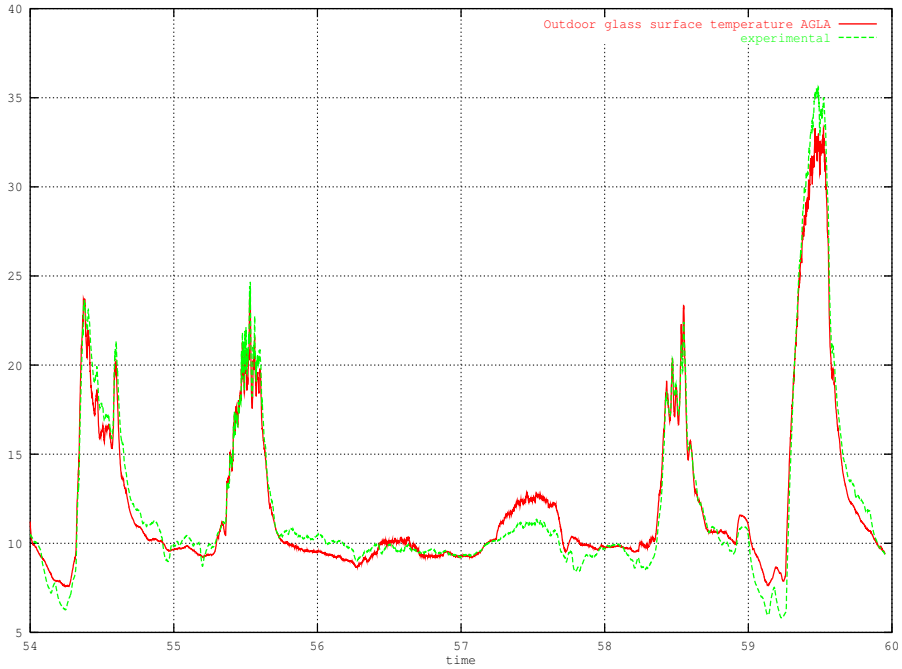

(b)

Figure 3.18: Period from February 23rd to 28th: a)Surface temperature at the TIM glass (A04), side water tank, $\epsilon_{rms} = 0.12$; b) Window outdoor surface temperature, $\epsilon_{rms} = 0.08$.

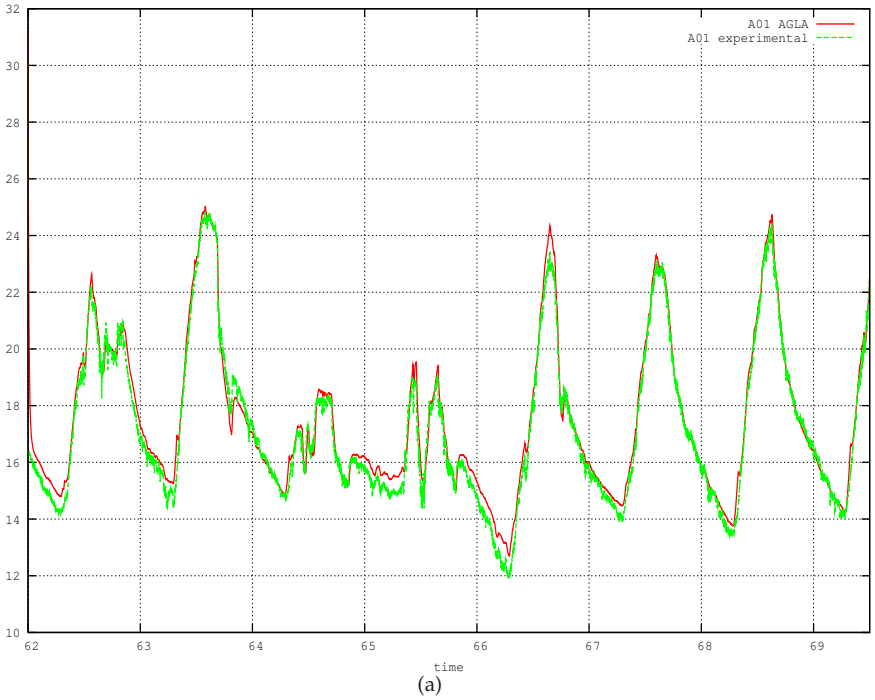

(a)

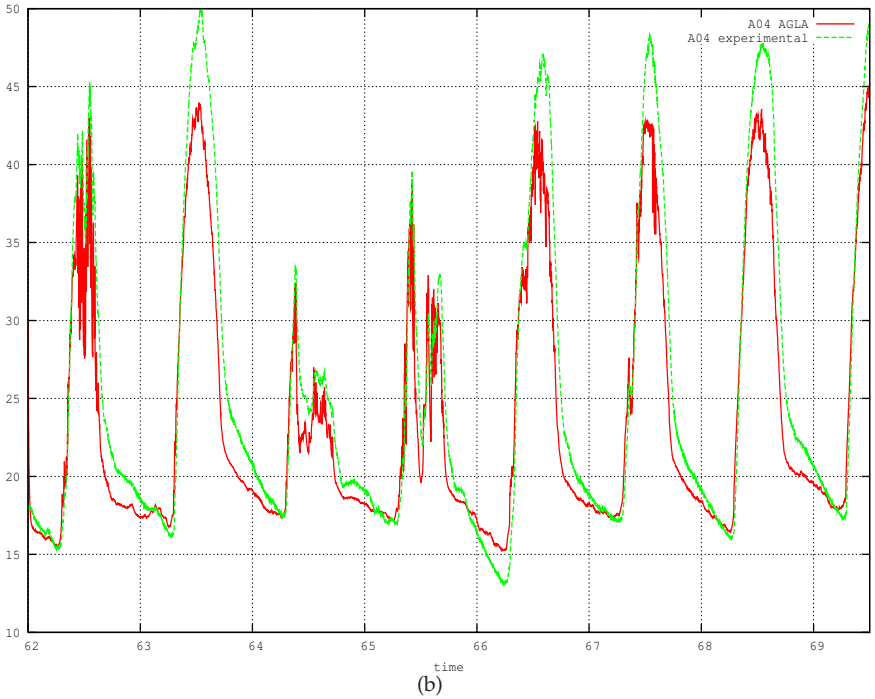

(b)

Figure 3.19: Period from March 3rd to 10th: a) Indoor wall surface temperature (A01), $\epsilon_{rms} = 0.03$; b) Surface temperature at the TIM glass (A04) $\epsilon_{rms} = 0.11$.

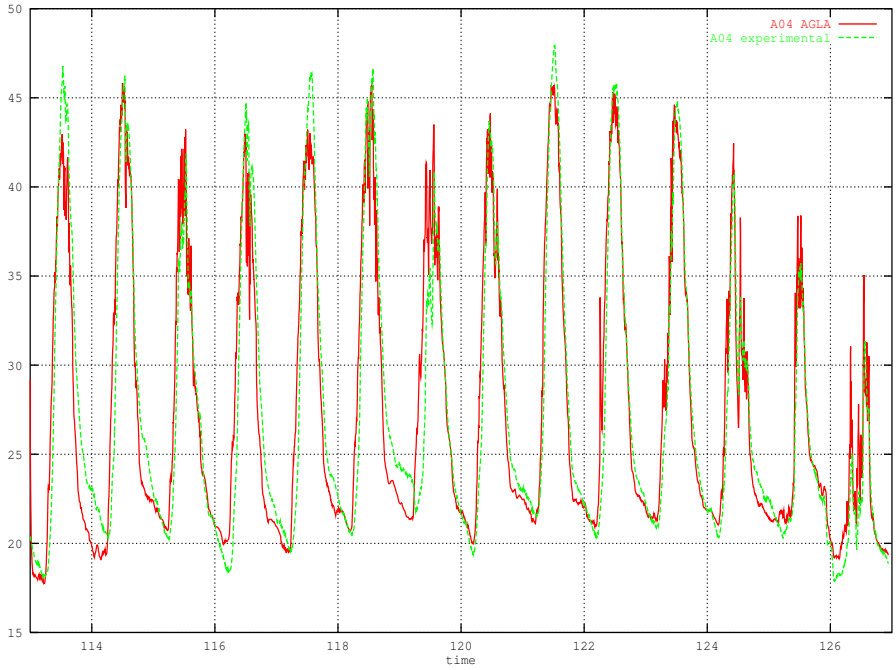

(a)

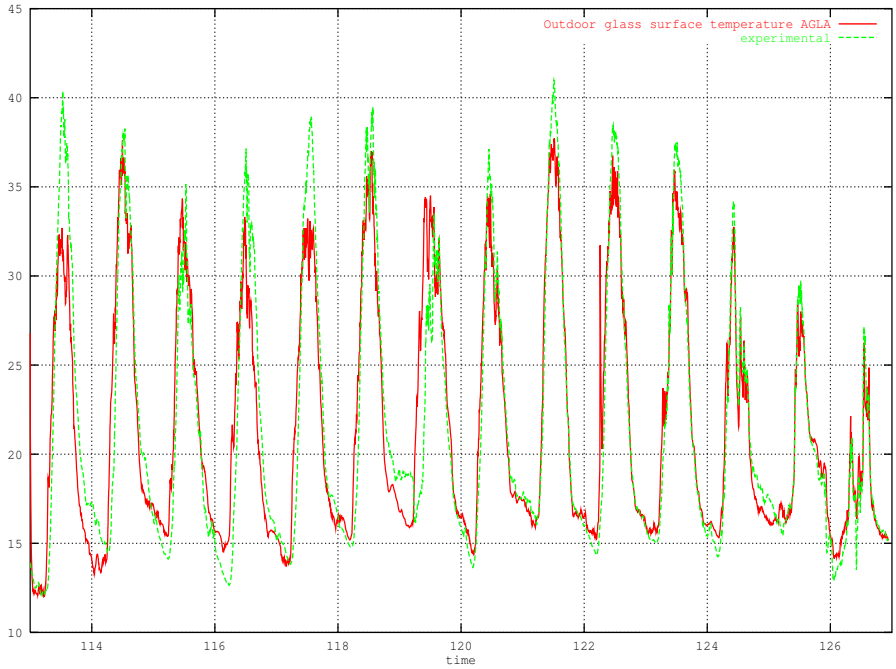

(b)

Figure 3.20: Period from April 22nd to May 7th: a)Surface temperature at the TIM glass (A04), $\epsilon_{rms} = 0.09$; b)Window outdoor surface temperature, $\epsilon_{rms} = 0.11$.

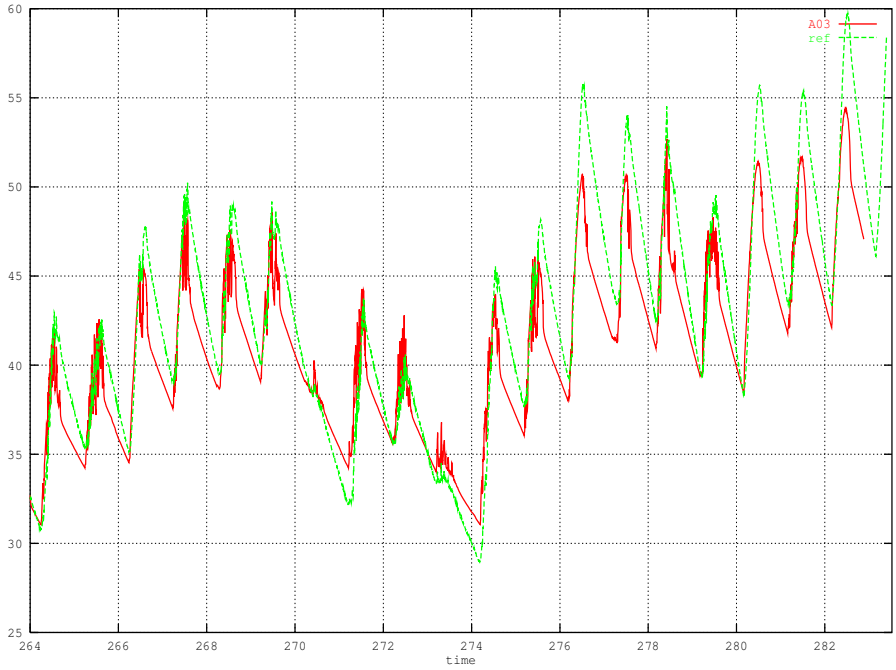

(a)

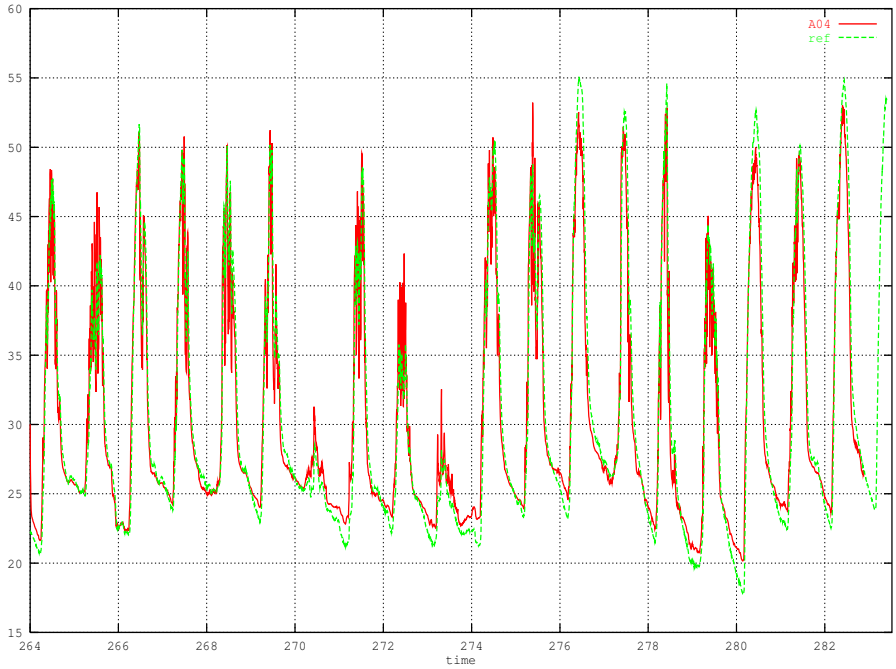

(b)

Figure 3.21: Period from September 21st to October 9th: a)Absorber surface temperature (A03), $\epsilon_{rms} = 0.059$; b)Surface temperature at the TIM glass (A04), $\epsilon_{rms} = 0.058$.

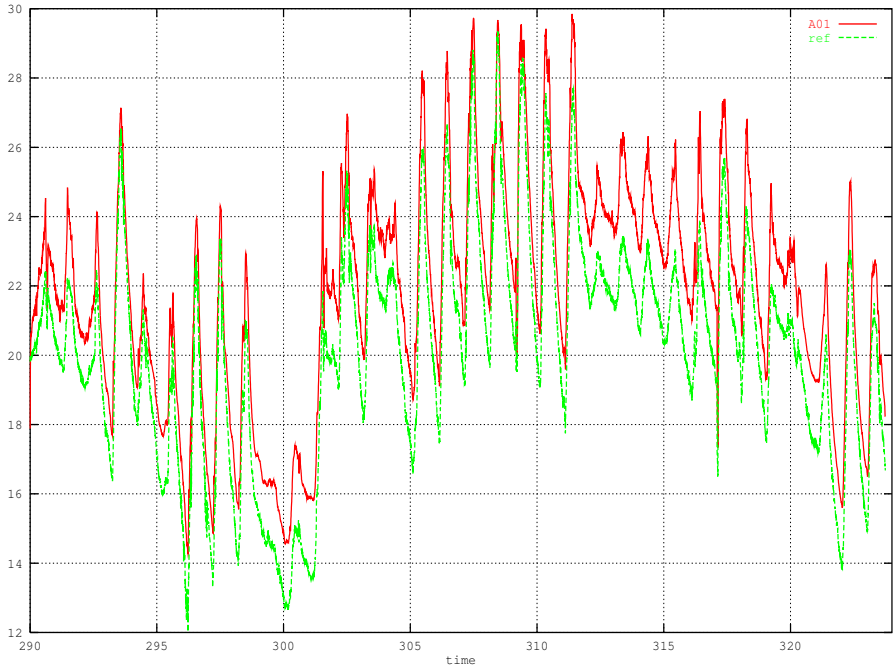

(a)

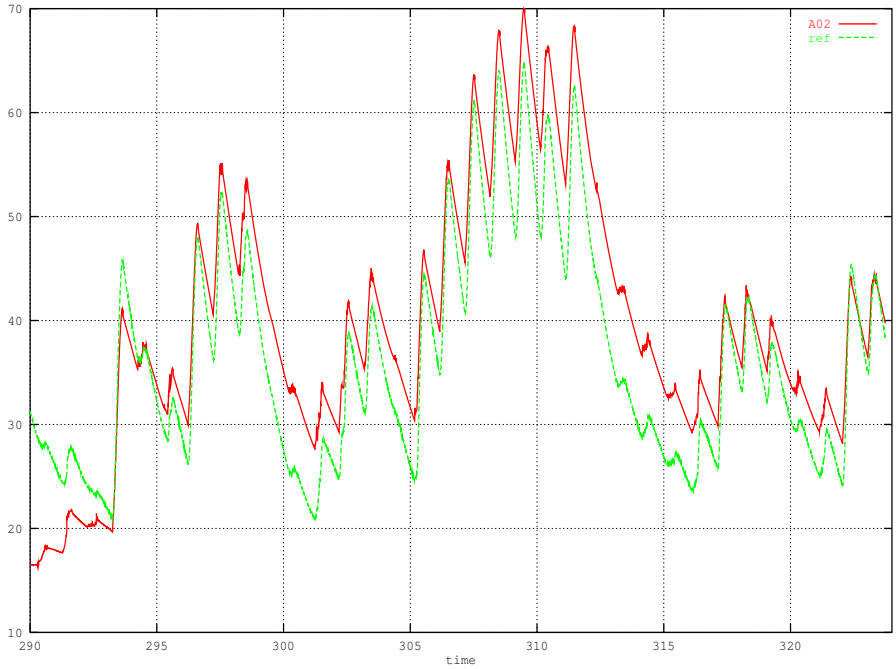

(b)

Figure 3.22: Period from October 17th to November 19th: a) Indoor wall surface temperature (A01), $\epsilon_{rms} = 0.09$; b)Indoor wall surface temperature, side water tank (A02), $\epsilon_{rms} = 0.16$;

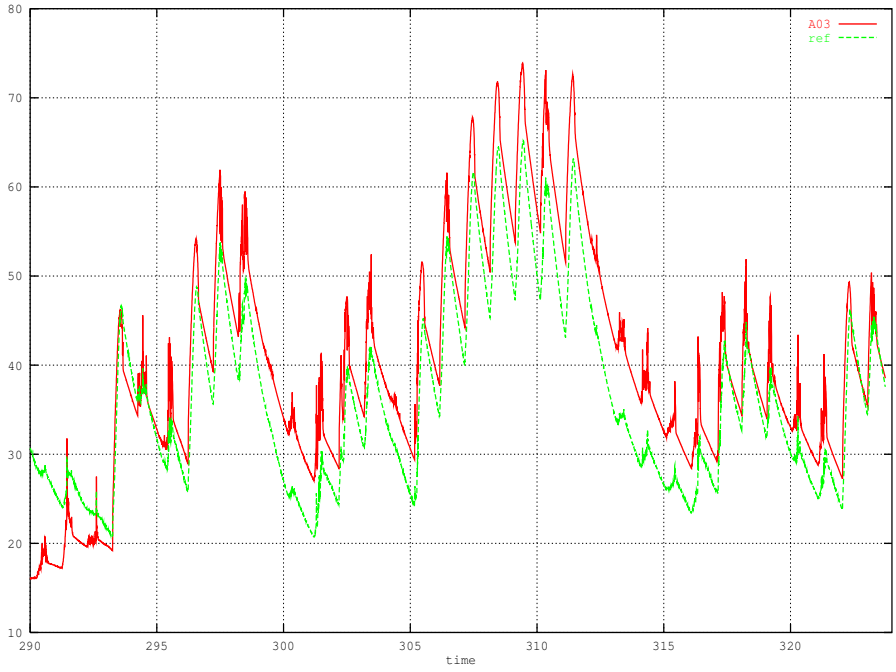

(a)

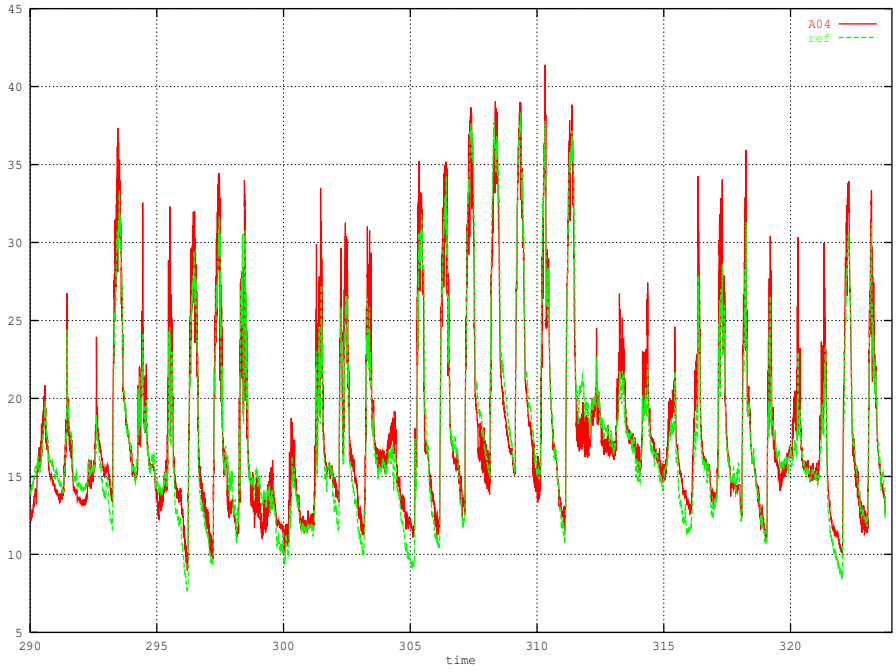

(b)

Figure 3.23: Period from October 17th to November 19th: a)Absorber surface temperature (A03), $\epsilon_{rms} = 0.17$; b)Surface temperature at the TIM glass (A04) $\epsilon_{rms} = 0.089$.

From the comparison of the experimental results with those obtained numerically, it is observed that for the different periods, the degree of agreement is quite similar. The numerical prediction is able to predict the peaks obtained during the experiment in accordance with peaks of solar radiation. The behaviour during night hours is also quite well predicted, although the experimental values are a bit lower than the numerical ones during night, indicating a large term of heat losses.

Uncertainties analysis

The validation has consisted in comparing the experimental versus the numerical results. When a large deviation is found, it may be an indication of either a bug in the code or the use of a poor or inappropriate model. The validation process is used also to guess some unknown physical property.

Table 3.5 shows the values of the errors computed (ϵ_{rms}) for five different periods:

Table 3.5: Root mean square error (ϵ_{rms})

Variable	Periods:				
	1/6 to 9/6	6/7 to 12/7	13/7 to 2/8	21/9 to 9/10	17/10 to 19/11
A01	0.028	0.029	0.034	0.026	0.090
A02	0.075	0.058	0.10	0.055	0.16
A03	0.082	0.069	0.11	0.057	0.17
A04	0.086	0.097	0.093	0.061	0.089
Window	0.089	0.099	0.056	0.056	–

In order to carry on a robust quantification of the differences between numerical and experimental data, a root mean square approach has been chosen. The main advantage of this approach consists in producing always positive values and being the largest error estimator. Other ones, like the mean relative, mean absolute, or mean error deviation, predict lower values. The root mean square ϵ_{rms} works like an integral accuracy index.

From the analysis of the main discrepancies, it may be observed that the temperatures at both tank walls (A02 and A03) are the variables which show a higher error level. This is probably due to the difficulty in the evaluation of heat transfer coefficients from these walls. However, a good degree of agreement has been found between experimental and numerical variables, in the different periods and configurations analyzed. For these reasons, it is possible to afirm that the algorithm implemented is able to predict quite well the temperatures at the facade integrated with water-based solar collectors.

3.5 Conclusions

The numerical simulation models have been submitted to a validation process in different forms. The numerical code was verified at the first stage by comparing the numerical results with those obtained for simplified situation with analytical solutions. In the second stage, a comparison with tabulated global performance coefficients of simple facade configurations was carried out. An analysis based on BESTEST strategies was also begun, these tests will continue in the future, with the implementation of other calculation rutines.

The experimental research has been carried out in test cells situated at different geographical locations, thus they were subjected to different climatic conditions. It has been focused on measures of temperatures and heat fluxes at the surfaces of the facade. This task has produced good results. The velocities and temperatures inside the air channel were not measured within this work, since the one-dimensional approach of channel model is not able to reproduce the actual two-dimensional behaviour. However, we have taken punctual measurements of air temperatures inside the channel and the water accumulator (in the case of the solar collector integrated facade) to compare them with the mean values predicted by the code obtaining a good agreement.

Summarizing, the experimental research carried out allow to conclude that the numerical tool is able to predict the thermal performance of these advanced facades, although it is unable to predict accurately the air channel behaviour, due to its one-dimensional limitation. Future work will focus on obtaining suitable correlations for each particular situation and linking this numerical tool with a CFD tool to carry out more detailed predictions of heat transfer within the channel, at least for short periods of time.

NOMENCLATURE

c	specific heat (J kg^{-1} $^{\circ}K^{-1}$)
e	experimental
E_1, E_2	exponential integral equation of first and second order respectively
I	radiation intensity
k	thermal conductivity (W m^{-1} $^{\circ}K^{-1}$)
L	latent heat (J kg^{-1}), total width (m)
n	numerical
N	total number of points
q	heat flux (W m^{-2})

T	temperature
t	time
x	space coordinate (m)

Greek symbols:

ϵ_t	thermal emissivity
ϵ_{rms}	error computed as root mean square
Φ	adimensional temperature
ρ	density (kg m^{-3})
ψ	adimensional heat flux
τ	optical path

Subscripts:

a	ambient
b	black body
i	internal
L	liquid
m	melting
S	solid

Acronyms:

AGLA	Advanced Glazed Facade Simulation Code
DOM	Discrete Ordinate Method
$SHGC_o$	Overall Solar Heat Gain Coefficient
TIM	Transparent Insulation Material
U_0	Overall Heat Transfer Coefficient

References

[1] V. Alexiades and A.D. Solomon. *Mathematical Modelling of Melting and Freezing Processes*. Hemisphere Publishing Corporation, 1993.

[2] H. S. Carslaw and J. C. Jaeger. *Conduction of Heat in solids*. Oxford University Press, 1959.

[3] L. Rubinstein. *The Stephan Problem*. American Mathematical Society, 1971.

[4] Max A. Heaslet and R. F. Warming. Radiative Transport and Wall Temperature Slip in an Absorbing Planar Medium. *International Journal of Heat and Mass Transfer*, 8:979–994, 1965.

[5] Max A. Heaslet and R. F. Warming. Radiative Transport in an absorbing planar medium II. Predictions of Radiative Source Functions. *International Journal of Heat and Mass Transfer*, 10:1413–1427, 1967.

[6] M.F. Modest. *Radiative heat transfer*. McGraw-Hill, 1993.

[7] P.J. Coelho. Fundamentals of a new method for the solution of the radiative transfer equation. *International Journal of Thermal Sciences*, 44:809–821, 2005.

[8] ASHRAE. *ASHRAE HANDBOOK Fundamentals*. 1997.

[9] Aguilà Usart P. Disseny termoenergètic de façanes, simulació numèrica i interfície de tractament de dades. Projecte de fi de carrera., 2006.

[10] R. Judkoff and J. Neymark. Building Energy Simulation Test and Diagnostic Method (BESTEST). Technical report, National Renewable Energy Laboratory, 1995.

[11] M. Costa, A. Oliva, M. Soria, and D. Faggembauu. Final Report -Publishable-. Technical report, 2000.

[12] M. Soria, D. Faggembauu, M. Costa, T. Ojanen, I. Heimonen, and C. Simonson. PV-Panel siding for renovation of walls- part II: numerical analysis. pages 1–8, 2000.

[13] M. Costa, O. Aceves, F. Sen, W. Platzer, A. Haller, M. Indetzki, and T. Ojanen. Analysis of multi-functional ventilated facades. an European Joule Project. pages 1–9, 2000.

[14] T. Ojanen, I. Heimonen, and C. Simonson. PV-Panel siding for renovation of walls- part I: Thermal performance experiments in northern climate conditions. In *Proceedings of the 3rd ISES Europe Solar Conference (EUROSUN 2000)*, 2000.

[15] A. Haller, H. J. Althaus, W. Platzer, and W. Goerdt. Gain Control for solar wall heating with transparent insulation (TI) requirements for cost effective application of natural ventilation in multifunctional and ventilated facades (MFVF). In *Proceedings of the 3rd ISES Europe Solar Conference (EUROSUN 2000)*, 2000.

[16] W. Platzer and W. Goerdt. Solar walls with ventilated transparent insulation. Performance, properties, problems and prospects. In *Proceedings of the 3rd ISES Europe Solar Conference (EUROSUN 2000)*, 2000.

[17] D. Faggembauu, M. Costa, M. Soria, and A. Oliva. Numerical analysis of the thermal behaviour of glazed ventilated facades in mediterranean climates. Part I: Development and validation of a numerical model. *Solar Energy*, 75(3):217–228, 2003.

Chapter 4

Thermal analysis of facades designs

4.1 Introduction

In this chapter, a *standard* ventilated facade is introduced, its behaviour is numerically studied and compared with other conventional facades and a parametric study of different design variants for ventilated and single skin facades is carried out. Additionally, a facade including transparent insulation is numerically studied and subjected to a parametric analysis in single and double skin configurations. Finally, facades including integrated collector-accumulator devices contributing to provide heating and domestic hot water wil be considered. From this study, it will be possible to provide some design suggestions for double skin envelopes in different climatic conditions, including advanced materials and innovative designs.

4.2 Definition of a standard reference case

What will be considered in this work to be the schematic of a standard ventilated facade is shown in Figure 4.1. It was selected because of its frequent use in high-end buildings in Southern Europe. It is made up of a single outdoor glass layer, an air channel and an indoor layer that comprises two zones: a double-glazed area at the top and an insulated panel at the base. This standard case has neither a channel curtain nor an indoor curtain. Table 4.1 shows the geometry and property data of the elements that make up the facade module.

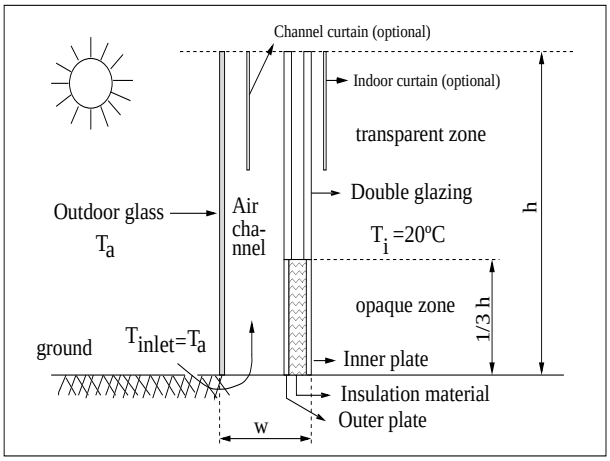

Figure 4.1: Schematic geometry of the standard analyzed case. It is made up by an external absorptive glass layer and an internal layer formed by a double-glazed area at the top and an opaque zone at its base

Table 4.1: Geometry and properties considered. Units in SI

	Thickness	α	τ	ϵ	ρ	c_p	k
Outdoor glass	0.006	0.49	0.42	0.84	2500	795	1.16
Air channel	0.10						
The imposed air flow is 0.36 m^3/s (forced convection)							
Indoor layer, transparent zone:							
First pane	0.004	0.08	0.85	0.84	2500	795	1.16
Air gap	0.012						
Second pane	0.004	0.08	0.85	0.84	2500	795	1.16
Indoor layer, opaque zone:							
Outer plate	0.0005	0.37	–	0.9	7900	477	14.9
Insulation material	0.040	–	–	–	55	1210	0.027
Inner plate	0.0005	–	–	0.9	7900	477	14.9

Total height h: 1.65 m, total width w: 0.147 m, total depth: 1.8 m.

To approximate outdoor conditions, instantaneous meteorological information corresponding to the city of Barcelona [1] was generated using monthly averaged meteorological data, as described in Chapter 2. These included the total daily radiation over a horizontal surface (Figure 4.2(a)), the daily maximum and minimum

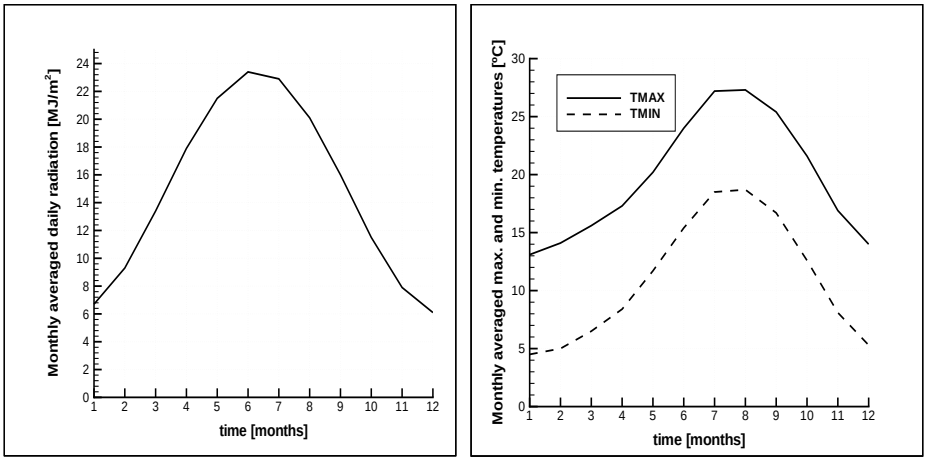

(a) (b)

Figure 4.2: Typical climatic data for Barcelona: a) Solar radiation over horizontal surface; b) Maximum and minimum temperatures

temperatures (Figure 4.2(b)), the wind velocity and the relative humidity. The instantaneous information generated consists in sky, ground and ambient temperatures, solar azimuth and altitude, direct and diffuse radiation over the surface of the facade, wind velocity and direction, and relative humidity. The ground thermal emissivity was considered equal 0.96 and the solar reflectivity 0.2. The facade-ground view factor was set equal to 0.5. The indoor air temperature was considered to be constant and equal to 20°C. The thermal radiation that emanates from the indoor walls of the facade was considered to be originated at a uniform black body at 20°C. A constant velocity of 2 m/s was imposed in the air channel, and the air input temperature was considered to be equal to the outdoor ambient temperature.

4.3 Numerical results for the standard case

4.3.1 Integrated heat fluxes

As described in chapter 2, the following variables determine the overall balance of the facade (Equation 2.125):

$$FOG = FIG + AEG + TSE \tag{4.1}$$

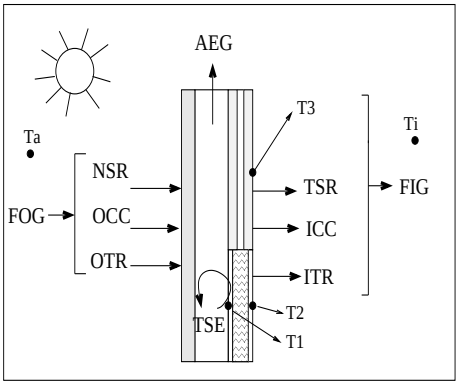

Figure 4.3: Heat fluxes through a standard geometry case

These variables are shown in MJ/m^2 in Table 4.2 for the standard case presented and schematically in Figure 4.3. The values in the table were integrated for a summer month (July), a winter month (January) and for the whole year. Table 4.3 shows the heat fluxes conforming the indoor and outdoor heat gains.

$$FIG = TSR + ICC + ITR \tag{4.2}$$

$$FOG = NSR + OCC + OTR \tag{4.3}$$

Table 4.2: Standard case global heat fluxes (MJ/m^2)

Variable	July	January	Annual
$\overline{FIG}$	87.4	19.4	655.6
$\overline{FOG}$	184.5	141.1	2031.6
$\overline{TSE}$	3.1	-2.0	5.2
$\overline{AEG}$	94.1	123.6	1370.8

Table 4.3: Standard case indoor and outdoor heat gains(MJ/m^2)

Variable	July	January	Annual	Variable	July	January	Annual
$\overline{TSR}$	66.2	71.5	858.4	$\overline{OTR}$	-46.8	-132.5	-1111.2
$\overline{ITR}$	15.6	-36.9	-144.7	$\overline{OCC}$	-44.4	-24.4	-433.6
$\overline{ICC}$	5.6	-15.1	-58.1	$\overline{NSR}$	275.7	297.9	3576.5

In summer, the indoor heat gains ($\overline{FIG}$) make up approximately 47% of the total outdoor gains ($\overline{FOG}$), while air channel enthalpic gains ($\overline{AEG}$) make up about 51%

of the outdoor gains (Table 4.2). The indoor heat gains are reduced in winter (they represent 14% of the $\overline{FOG}$).

Accumulated energy is negligible because it is integrated over a long period of time. According to Table 4.3, the convective and radiative terms ($\overline{ICC}$ and $\overline{ITR}$) have opposite signs in summer and winter. In summer, they represent a gain and in winter a loss. The most important contributor to indoor heat gains is the transmitted solar radiation ($\overline{TSR}$), followed in summer by the term that represents thermal radiation.

Regarding the balance of outdoor heat gains (Table 4.3), the only positive term is that of solar radiation ($\overline{NSR}$). The remaining terms that contribute to $\overline{FOG}$ are negative in winter and summer, which represents a convective and radiative heat loss.

4.3.2 Instantaneous heat fluxes and temperatures

The instantaneous values for the variables involved in the overall balance are shown in Figure 4.4 for a sample summer and winter day, while Figure 4.5 shows the instantaneous temperatures corresponding to the same two days.

As it can be observed in Figure 4.4, the maximum values of the variables are quite similar in summer and winter. This is due to the greater amount of solar radiation available in winter over the vertical surface of the facade. The heat fluxes entering the facade (FIG) represent about one third of the outdoor gains (FOG) at noon. Although the integrated value $\overline{FIG}$ is always positive for this climate (Table 4.2), there are some thermal losses at night in winter.

On the other hand, as concerns the instantaneous temperatures, it can be observed in Figure 4.5 that the scales of temperatures for summer and winter days are quite different. The temperature of the surface of the opaque zone facing the channel (T1), reaches values of 30°C in summer and 16°C in winter. Indoor surface wall temperatures are shown for the glazing zone (T3) and the opaque zone (T2). While temperature variations are insignificant for the opaque zone (between 21°C and 19°C), for the transparent zone, variations are larger. For an average day in summer, the highest value of T3 is 25°C, which is when the ambient temperature (Ta) is 27°C. For an average day in winter, the lowest value of T3 is 14 °C, which is when the ambient temperature is around 4°C.

Indoor surfaces temperatures tend to be closer to indoor ambient temperatures for ventilated facades than for conventional glazed facades. This feature becomes particularly evident during summer if there are curtains inside the air channel (rather than indoors). This reduces the thermal discomfort caused by thermal radiation heat transfer at the areas nearest the facade.

The monthly integrated values of the net (η_i) and positive fraction (η_{ip}) of indoor

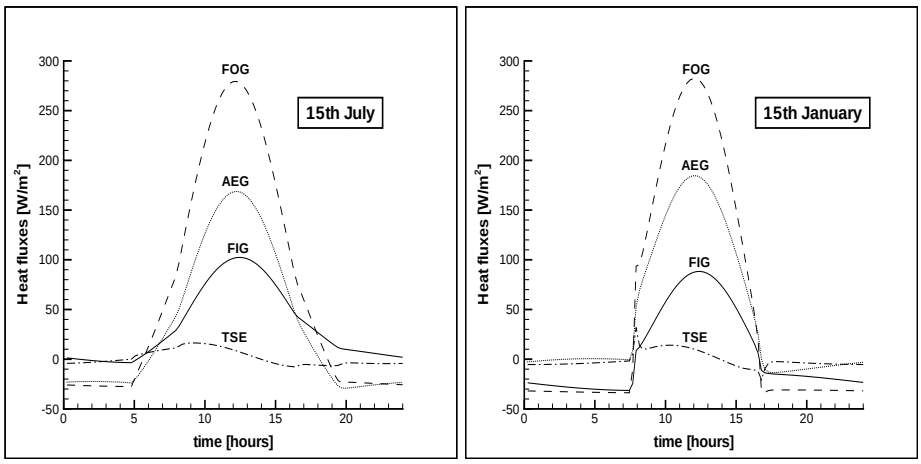

Figure 4.4: Instantaneous values of heat fluxes on 15th July and 15th January. FOG: Facade Outdoor Gains, FIG: Facade Indoor Gains, AEG: Air Enthalpic Gains and TSE: Total Stored Energy

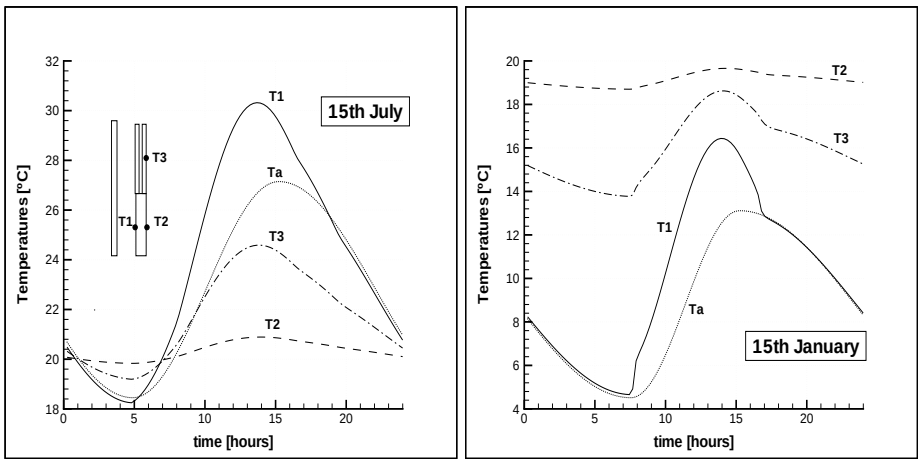

Figure 4.5: Instantaneous values of temperatures on 15th July and 15th January. T1: Temperature of the opaque surface facing the channel, T2: Temperature of the opaque surface facing indoors, T3: Temperature of the surface of the glazing zone facing indoors, Ta: ambient temperature

and enthalpic gains (η_c), defined in Chapter 2 are shown in Figure 4.6 for this facade module.

During the summer months, as η_i is higher, approximately 27% of the available solar radiation is translated into net indoor gains (thermal gains minus thermal losses). Nevertheless, in winter, only 6% of solar radiation translates into net indoor gains. During summer, the net proportion and the positive proportion of indoor gains are almost equal, which indicates that in this period no heat losses are produced. During the rest of the year, the positive fraction of indoor gains is higher. The channel efficiency shows an inverse trend; its values are lower in summer, and higher in winter (about 35% of solar radiation becomes enthalpic gains). Variations in the fraction of enthalpic gains are not so strong.

The values for indoor and air channel efficiency shown in Figure 4.6 can be summarized by looking at the annual average values of these coefficients:

Table 4.4: Annual values of the proportions of net and positive indoor gains and enthalpic gains for the case defined as standard

	$\eta_{i,annual}$	$\eta_{ip,annual}$	$\eta_{c,annual}$
Whole standard case	0.16	0.21	0.33
Opaque zone	−0.015	0	–
Transparent zone	0.24	0.31	–

4.4 Numerical results of non-ventilated facades

The performance of four conventional (non-ventilated) facades was subjected to numerical analysis. The cases that were analyzed are the following:

(a)- Double-glazed facade without ventilated channel (Figure 4.7(a)). Keeping the geometry constant, the indoor double glazing was used as the external facade. Both layers of glass had the following parameters: $\alpha = 0.08$, $\tau = 0.85$ and $\epsilon = 0.84$.

(b)- Double-glazed facade with a high absorptive external glass (Figure 4.7(b)). The outdoor layer of glass was the one used as the "external skin" as defined in the standard reference case ($\alpha = 0.49$, $\tau = 0.42$), whereas the internal glass is one of the common types of glass described in the previous item.

(c)- Conventional facade (Figure 4.7(c)). This facade is made up of the "indoor skin" as defined as standard reference case.

(d)- Standard reference case with closed channel (Figure 4.7(d)).

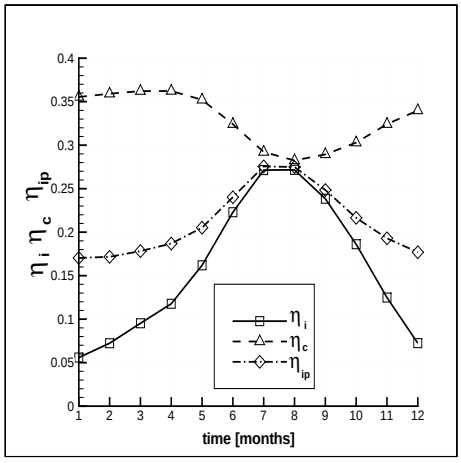

Figure 4.6: Monthly performance of the standard case as described by the positive proportion of indoor gains η_{ip}, the net proportion of indoor gains η_i and the proportion of enthalpic gains η_c.

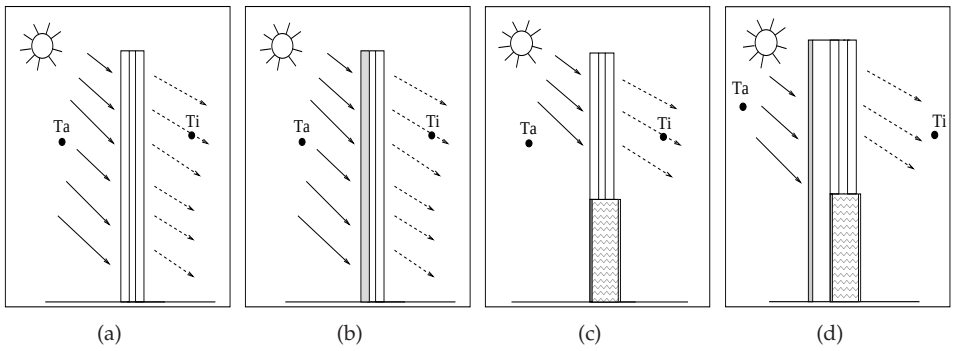

Figure 4.7: Non-ventilated cases. a) Double glazing; b) Double glazing with high absorptive external glass; c) Transparent plus opaque; d) Standard with closed channel

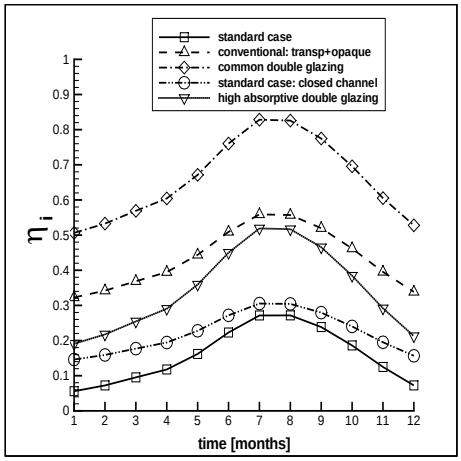

Figure 4.8: Fraction of net indoor gains η_i of the analyzed standard case and non-ventilated cases

The monthly proportion of net indoor heat gains for these facades, η_i, is shown in Figure 4.8. η_c is equal to zero for these options since no enthalpic gains are possible.

It may be noted that for a completely glazed facade comprised of double glazing without special features, the net indoor heat gains are 80% of the solar radiation over the surface of the facade. This means that a large amount of solar radiation enters inside the room and it will be absorbed and then delivered to the internal zones in the form of convective and radiative transfer, contributing to an increment of indoor temperatures and air-conditioning consumption. For a conventional facade the maximum value of net indoor gain is 55% of the solar irradiation. A double-glazed facade that uses special glasses allows to reduce the net proportion of indoor gains: a maximum of 0.50 is obtained. The differences between the ventilated standard case and the case with a closed channel occur mainly in winter. During this period, the indoor proportion for the ventilated facade is lower, because of the proportion of solar energy that becomes enthalpic gain. In general, the use of an external glazed skin in these highly transparent facades reduces the indoor heat gains even if the air channel is closed. The use of ventilated facades notably improves the thermal behaviour of facades whose glazing is entirely external. The average values for the coefficients representing indoor heat gains over the course of one year are the following:

Common double glazing: $\eta_{i,annual} = 0.66$

High absorptive double glazing facade:	$\eta_{i,annual} = 0.35$
Conventional transparent plus opaque facade:	$\eta_{i,annual} = 0.43$
Standard case with closed channel:	$\eta_{i,annual} = 0.22$

4.5 Parametric analysis of the ventilated facades

The standard case presented in Figure 4.1 was modified by changing only one parameter at a time. In each case, transient simulations were performed for one year. The cases analyzed were the following:

Va- Curtain in the air channel: here, a curtain covering half of the transparent area (length equal to $1/3$ h, see Figure 4.1) was modelled by treating it as a layer of glass in which $\alpha = 0.65$, $\tau = 0.10$, $\epsilon = 0.82$, 1 mm thickness, $\rho = 2500$ kg/m^3, $c_p = 795$ J/kg K and $k = 1.16$ W/m K.

Vb- Curtain in the indoor side: in this case, the same curtain described previously was placed in the indoor part of the building and extended to cover half of the transparent area (Figure 4.1).

Vc- Use of high inertial materials in opaque zone: here, the opaque layer of the facade was replaced with a wall impregnated with a phase change material. This wall was 0.050 m thick and was contained between two steel layers as in the standard case (see Figure 4.1). The following properties of the impregnated wall (solid and PCM) were assumed to hold: $\rho = 608$ kg/m^3, $c_p = 1423$ J/kg K and $k = 0.22$ W/m K for both phases, $T_m = 19.5$°C and $L = 42000$ J/kg.

Vd- Natural convection in the air channel: here, the flow rate in the air channel is due to natural convection. The expressions applied do not consider there to be any obstacles at the inlet or at the outlet of the channel.

Ve- Use of a low emissivity pane: in this case a low emissivity coating was used on the inner air gap surface of the double glazing (see Figure 4.1). Emissivity was reduced to $\epsilon = 0.10$.

The remaining parameters and boundary conditions were assumed to be the same as in the standard case.

4.5.1 Ventilated cases a and b: Curtain analysis

Table 4.5: Overall heat fluxes of the standard reference case and ventilated cases (Va and Vb) with curtains (MJ/m^2)

	Standard			Case Va			Case Vb		
Variable	July	Jan.	Annual	July	Jan.	Annual	July	Jan.	Annual
$\overline{FIG}$	87.4	19.4	655.6	55.3	−14.6	244.1	75.4	12.9	542.6
$\overline{FOG}$	184.5	141.1	2031.6	180.1	138.0	1985.4	179.9	136.9	1977.5
$\overline{TSE}$	3.1	−2.0	5.2	3.1	−2.0	5.3	3.1	−2.0	5.2
$\overline{AEG}$	94.1	123.6	1370.8	121.7	154.7	1736.9	101.4	126.0	1429.7

Compared to the standard case, the presence of a curtain provokes a reduction in the indoor heat gains $\overline{FIG}$ (Table 5.5). This reduction is much higher (approximately 37%) when curtains are located inside the air channel. In this case, the air has greater enthalpic gains due to the heating of the curtain. The maximum curtain temperature is approximately 30°C when it is in the air channel, and around 32°C when it is in the indoor zone. In Figure 4.9, the monthly values of η_i are shown. In the summer period, the net proportion of indoor gains for the channel curtain reduces from 27% to 17%. Negative efficiency values (of η_i) are achieved in winter for the channel curtain. This represents a net heat loss (from indoor to channel).

4.5.2 Ventilated case c: Use of high inertia materials

Table 4.6: Overall heat fluxes of the standard reference case and ventilated case (Vc) with a PCM opaque wall (MJ/m^2)

	Standard			Case Vc		
Variable	July	January	Annual	July	January	Annual
$\overline{FIG}$	87.4	19.4	655.6	93.4	2.9	588.7
$\overline{FOG}$	184.5	141.1	2031.6	185.3	139.2	2024.6
$\overline{TSE}$	3.1	−2.0	5.2	3.1	−2.0	5.3
$\overline{AEG}$	94.1	123.6	1370.8	88.7	138.4	1430.5

The replacement of the insulated opaque wall with a PCM wall produces the main heat fluxes shown in Table 4.6. According to this table, the main difference with regard to the standard case is the reduction in the $\overline{FIG}$ value in winter. However, these differences are not due to the use of PCM itself, but rather to the higher conductivity of the PCM wall. One must keep in mind that the gains through the

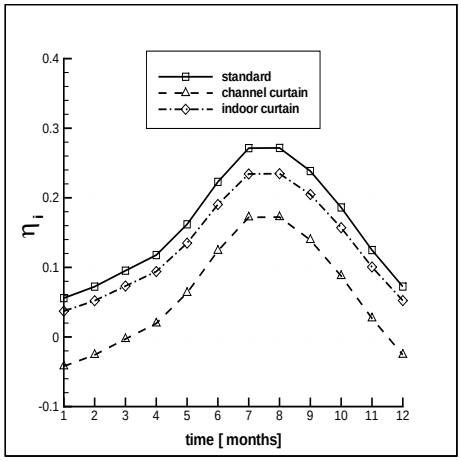

Figure 4.9: Comparison of the monthly performance of the facade module with curtains and the standard case

transparent zone are much greater than the gains through the opaque zone. Therefore, the presence of the PCM in the opaque zone is much less noticeable when the total gains are taken into account.

In order to analyze the actual effect of the PCM, a comparison was made between a situation in which there was a solid opaque wall filled with PCM and a situation characterised by a conventional wall with the same properties (Figure 4.10). As can be observed in Figure 4.10(a), the positive heat gains in the case of the wall with PCM are lower, and they only occur in the summer months. In Figure 4.10(b), the heat losses ($\overline{NFIG}$) can be seen to be almost equal during the winter months, and the differences between both walls become greater for the rest of the year. Consequently, if Figures 4.10(a) and 4.10(b) were combined to obtain the net results of the heat gains ($\overline{FIG}$), no appreciable differences between the two walls would be observed. Therefore, the effect of introducing PCM is a reduction in heat gains and losses, as the net gains remain unchanged [2].

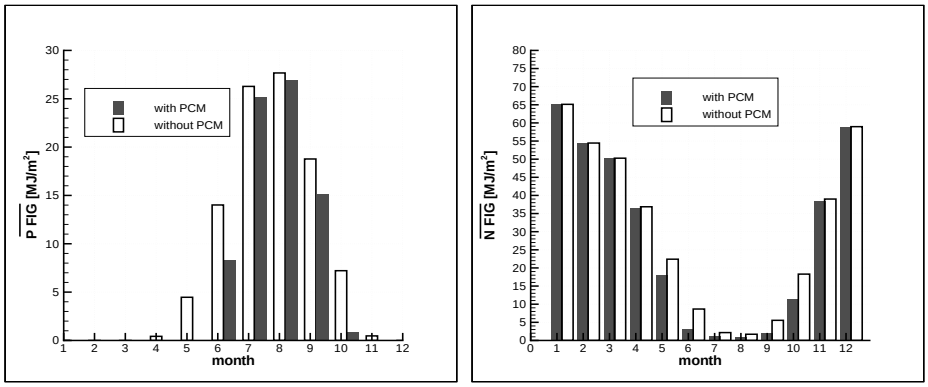

(a) (b)

Figure 4.10: a) Monthly heat gains $\overline{PFIG}$ through the PCM wall and a conventional wall with the same properties; b)Monthly heat losses $\overline{NFIG}$ through the PCM wall and a conventional wall with the same properties

4.5.3 Ventilated case d: Use of natural convection flow in channel

The standard case has been simulated assuming that the flow rate in the air channel is now due to natural convection.

No special devices for introducing or expelling air were modelled in the inlet or outlet of the channel. It was assumed that air entered at either the outdoor ambient temperature or the indoor temperature. Inside the channel, air movement was caused by natural or forced convection. Forced convection was assumed to hold for the standard reference case, whose flow rate was fixed to be $0.36m^3/s$. Forced convection ensures appropriate flow rates as defined by the design objectives. For instance, in summer, the air channel is able to function with air proceeding from the indoor zone of the building in order to either cool the facade surface or to renew inside air as required. When natural convection is the driving mechanism, the flow rate is considerably lower and therefore the enthalpic gains ($\overline{AEG}$) decrease (Table 4.7). The reduction is higher in winter when the flow rate induced in the channel is very low. However, it has to be taken into consideration that the natural convection flow rate is highly dependent on the total height, and the test case was only one storey high.

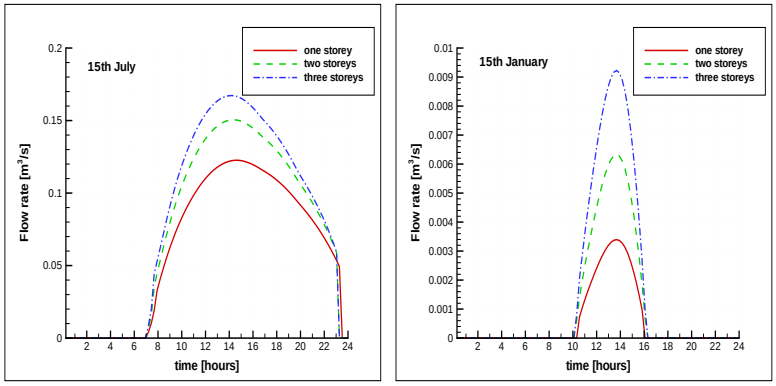

(a) (b)

Figure 4.11: Instantaneous flow rate induced over the course of one day in one, two and three-storey facades. Air flow originated outdoors. a)15th July; b)15th January.

Table 4.7: Overall heat fluxes in the standard reference case and in ventilated case with natural convection flow (MJ/m^2)

	Standard case:			With natural convection:		
Variable	July	January	Annual	July	January	Annual
$\overline{FIG}$	87.4	19.4	655.6	89.8	50.2	867.6
$\overline{FOG}$	184.5	141.1	2031.6	157.6	56.7	1272.5
$\overline{TSE}$	3.1	−2.0	5.2	3.0	−0.7	11.3
$\overline{AEG}$	94.1	123.6	1370.8	64.7	7.1	393.7

Channel height

Figure 4.11 shows the natural flow rates that were induced in the channel on an average summer and an average winter day, for a channel at the same height as in the standard case (one storey) and two and three-storey channels (each storey having the configuration of the standard case).

Comparing both figures, it can be seen that the values obtained in winter are very low for all the heights and that they are restricted to a few hours over the course of a day. Here, it is assumed that the air enters at outdoor ambient temperature. The air flow rates produced in the case in which the air proceeded from the indoor room are shown in Figure 4.12. In this case, as the air temperature was 20 $^{\circ}C$, greater flow

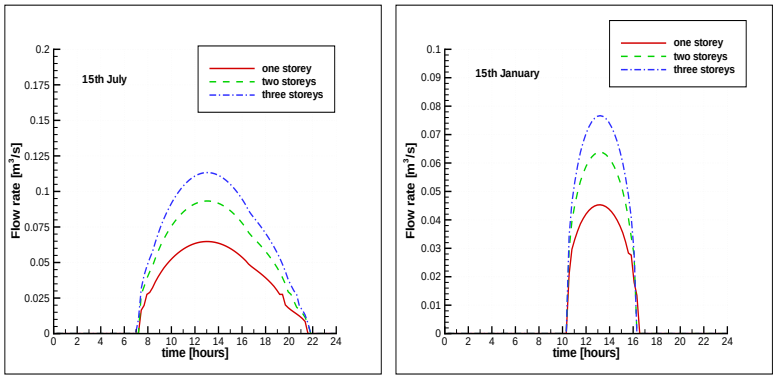

(a) (b)

Figure 4.12: Instantaneous flow rate induced over the course of one day in one, two and three-storey facades. Air flow originated indoors. a)15th July; b)15th January.

rates were produced in winter. The differences in the summer were not important as during these months the outdoor air is hotter than the indoor air.

Figure 4.13 shows the performance of the ventilated facade with natural convection in the channel. The coefficient of net indoor heat gains increased 8% during winter in the case of natural convection. The remarkable variation with respect to the standard case is that of the enthalpic performance. In winter, it is nearly zero with natural convection due to the low induced mass flow.

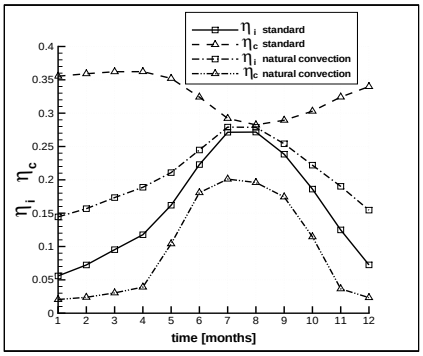

Figure 4.13: Comparison of the monthly performance of the facade module with natural convection and the standard case

Table 4.8 shows the values of the performance coefficients when considering different facade heights. Larger heights produce an increment in enthalpic gains, however, this increment does not result in outstanding differences in annual performance coefficients.

Table 4.8: Performance coefficients and overall net, positive indoor gains and enthalpic fluxes for different facade height (MJ/m^2). Natural convection, channel width $w = 0.10$m

Height	Annual variables:					
	$\overline{FIG}$	$\overline{PFIG}$	$\overline{AEG}$	η_i	η_{ip}	η_c
1.65	867.58	1050.28	393.74	0.208	0.251	0.094
3.3	864.47	1047.23	420.85	0.207	0.251	0.101
4.95	862.99	1045.81	438.29	0.207	0.250	0.105

Channel width

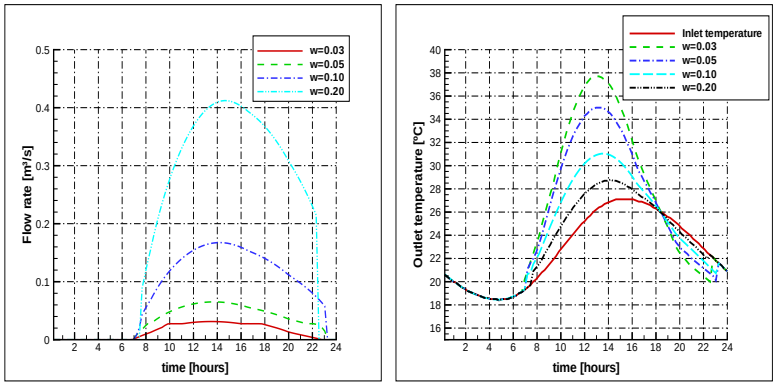

(a) (b)

Figure 4.14: a)Instantaneous flow rate induced over the course of one day (15th July) in a three-storey facade. b)Inlet and outlet temperature of channel air

When the channel width is varied (assuming natural convection flow), the air flow rate increases, as shown in Figure 4.14(a), and the outlet temperature obtained in the channel is larger (Figure 4.14(b)).

Thus, air enthalpic gains are larger, as observed in Figure 4.15(a), this increment does not alter in a remarkable manner the internal heat gains (Figure 4.15(b)). In

this case, it is due to the fact that internal gains are due mainly to solar radiation which is not altered by the channel, convective and radiative internal heat gains become slightly reduced with the increment of channel width because internal surface temperature is lower (Figure 4.15(c)).

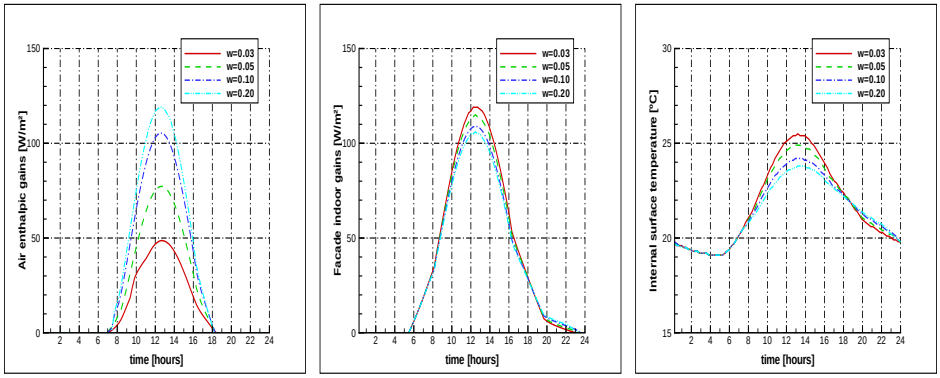

(a) (b) (c)

Figure 4.15: 15th July a)Variation of enthalpic gains obtained in channel with different width. b)Internal heat gains, c)Internal surface temperature

For the values analyzed here, from $w = 0.10$m, an additional increment in channel width does not produce outstanding effects neither in enthalpic nor in internal gains. The increment of width leads to a smaller aspect ratio H/w, this geometry according to the CFD analysis produces larger stratification in channel, thus, enthalpic gains are not modified from certain width value. Table 4.9 shows the values of the annual performance coefficients when considering different channel widths, for a configuration of three-storey facade.

Table 4.9: Annual performance coefficients and overall net, positive indoor gains and enthalpic fluxes for different channel widths (MJ/m^2). Natural convection in a three-storey facade.

Width	$\overline{FIG}$	$\overline{PFIG}$	$\overline{AEG}$	η_i	η_{ip}	η_c
0.03	874.13	1058.99	268.82	0.213	0.258	0.066
0.05	854.15	1039	372.42	0.208	0.254	0.091
0.1	841.83	1024.07	430.36	0.205	0.250	0.105
0.2	843.94	1022.63	406.96	0.206	0.250	0.099

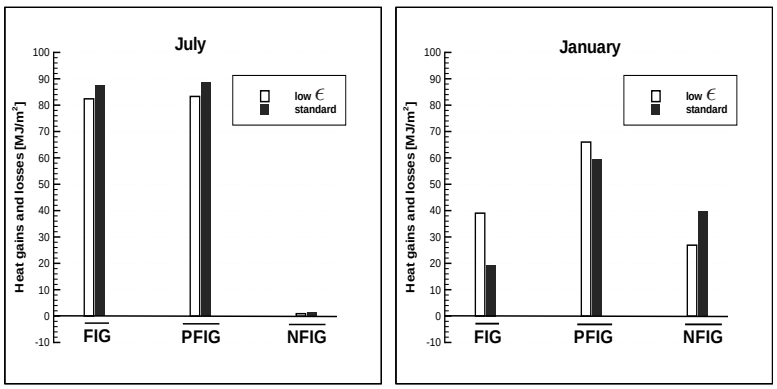

Figure 4.16: Monthly integrated heat gains and losses for the case with low-ϵ coating. a)July; b)January.

4.5.4 Ventilated case e: Use of a low-ϵ glass pane

Table 4.10: Overall heat fluxes of the case with low-ϵ coating in double glazing ($\mathrm{MJ/m^2}$)

	Standard			Case Vd		
Variable	July	January	Annual	July	January	Annual
$\overline{FIG}$	87.4	19.4	655.6	82.4	39.0	750.8
$\overline{FOG}$	184.5	141.1	2031.6	184.1	142.5	2038.7
$\overline{TSE}$	3.1	−2.0	5.2	3.1	−2.0	5.2
$\overline{AEG}$	94.1	123.6	1370.8	98.6	105.5	1282.7

The main effect of using a low-ϵ coating ($\epsilon = 0.1$) on the double glazing is a large increase in the $\overline{FIG}$ value in winter, which translates into an increase in the annual value (Table 4.10).

Figure 4.16 shows the decomposition of $\overline{FIG}$ in its two values $\overline{PFIG}$ and $\overline{NFIG}$ for summer and winter. In summer, there are no outstanding differences between the standard case and the low-ϵ case. In winter, the increase in the value of $\overline{FIG}$ is due to the increase in the heat gains and the reduction in heat losses.

Figure 4.17 shows the monthly performance of this facade. The proportion of net indoor gains, η_i, is higher in winter when compared with the standard case, and it is slightly lower in the summer period. The fraction of enthalpic gains η_c remains

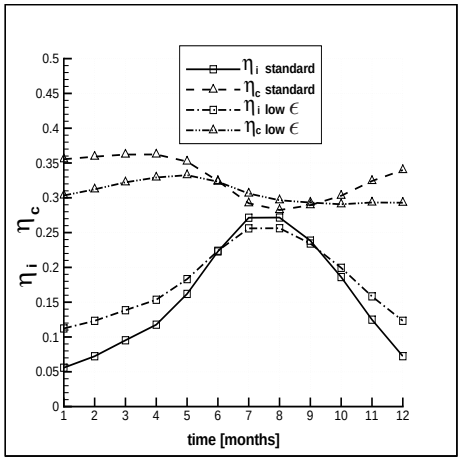

Figure 4.17: Comparison of the monthly performance of the facade module with low-ϵ coating and the standard case

scarcely changed over the course of the year, for a mean value of around 30%, which was slightly lower than for the standard case.

4.6 Numerical analysis of facades including TIM elements

The objective of this section is to compare the heating demand of a 110 m^3 room with a $2m^2$ aperture, which is occupied with different types of fenestration systems, as shown in Figure 4.18.

1. A low thermal emissivity double glazed window, with the properties indicated in Table 4.11.

Table 4.11: Geometry and properties of double window facade. Units in SI

	Thickness	α	τ	ϵ	ρ	c_p	k
Outdoor glass	0.006	0.11	0.82	0.84	2500	795	1.16
Air gap	0.012						
Indoor glass	0.004	0.08	0.85	0.10	2500	795	1.16

Total height h: 2 m, total width w: 0.022 m, total depth: 1 m.

2. The same window with a 5 cm TIM element between both glass layers and a 0.006m air gap between internal glass and TIM. The properties of TIM-ambient have been considered $\rho_t = 0.2$, $\rho_s = 0.01$ assumed to be the same at both sides of TIM, volumetric absorptivity [m^{-1}] $\kappa_t = 150$, $\kappa_s = 1.0$, thermal conductivity $k = 0.065$

3. A double skin facade similar to the bottom zone of standard defined case (Figure 4.1) formed by an external layer constituted by glass, air gap, 5cm TIM and an opaque absorber. Internal layer is formed by opaque insulation. An air channel separates external layer from internal insulation skin. Air movement in channel is produced by natural buoyancy forces, it is considered to enter at outside air temperature. Properties and geometric features are described in Table 4.12.

Table 4.12: Geometry and properties considered. Units in SI

	Thickness	α	τ	ϵ	ρ	c_p	k
Outdoor glass	0.006	0.11	0.82	0.84	2500	795	1.16
Air gap	0.008						
TIM element	0.050	–	–	–	–	–	0.065
Absorber plate	0.006	0.72	–	0.90	–	–	–
Air channel	0.040						
Indoor layer:							
First plate	0.005	–	–	0.90	2000	840	1.40
Insulation	0.050	–	–	0.90	150	300	0.027
Second plate	0.005	–	–	0.90	2000	840	1.40

Total height h: 2 m, total width w: 0.17 m, total depth: 1 m.

The properties of TIM-ambient have been considered $\rho_t = 0.2$, $\rho_s = 0.1$ assumed to be the same at both sides of TIM, volumetric absorptivities [m^{-1}]: $\kappa_t = 150$, $\kappa_s = 2.0$.

4. A single skin facade constituted by the same insulation wall considered as indoor layer of the previous case.

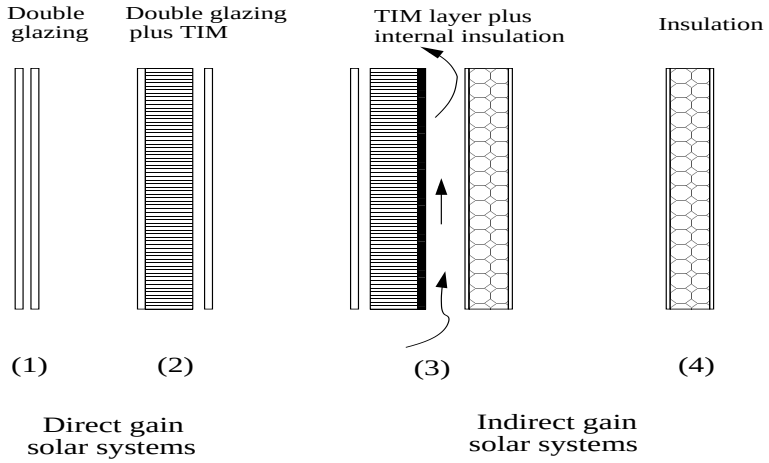

Figure 4.18: Configuration of facades analyzed. For each implementation, the external layer is at left.

4.6.1 Steady state analysis of facades including TIM

A steady state analysis has been carried out in order to calculate the values of both the overall heat transfer coefficient U_0 and the overall solar heat gain coefficient $SHGC_0$ of each of the configurations analyzed. This analysis has been carried out by imposing constant conditions for the indoor and outdoor air temperatures and the solar radiation [3]. Thus, the steady indoor heat flux can be computed as:

$$q = U_0(T_a - T_i) + SHGC_0\ I \qquad [W/m^2] \tag{4.4}$$

For a given temperature difference, the values of the U_0 Factor and $SHGC_0$ at normal incidence are tabulated for the facade compositions mentioned in section 4.6 in Table 4.13.

Table 4.13: U_0 (W/m^2 K) and $SHGC_0$ Factors

	U_0	$SHGC_0$
Double glazing	1.92	0.75
Double glazing plus TIM	1.23	0.70
TIM layer plus internal insulation	0.51	0.015
Insulation	0.35	0.013

U_0 coefficients were calculated by keeping to the numerical code conditions for winter based on ASHRAE data: outdoor temperature $T_a = -18$°C, indoor air temperature $T_i = 21$°C and null solar radiation. The outdoor convective heat transfer

coefficient was taken to be h_0 = 29 W/m^{2}K, which corresponds to a 24 km/h wind velocity and an indoor coefficient of h_i = 8.29 W/m^{2}K. In order to calculate $SHGC_0$, the indoor and outdoor temperatures were maintained equal and a constant solar radiation, $I = 800W/m^2$, was assumed. The standard subroutines implemented in $AGLA$ were used to address the heat fluxes that occurred in the facade.

4.6.2 Transient analysis of facades including TIM

A transient analysis has been performed for months from January to May, considering monthly climatic data of Geneve city [4]. This climatic condition has been chosen as representative of a central european climate, where the use of transparent insulation is applicable. In all the cases, indoor temperature is allowed to vary between 20 and 25°C, heating system is assumed to have a capacity of 2000 W. No internal generated gains have been foreseen, and a rate of air renovation has been fixed to 0.1 renovations per hour. Heat is transferred only in the fenestration wall, the rest of walls are considered adiabatic. The first two cases shown in Figure 4.18 have in common that they are direct gain solar systems, they allow the entrance of similar solar gains but the heat losses will be reduced with the use of TIM. Figure 4.19 shows the heat losses due to convection and radiative heat transfer in both transparent facade cases, also the heating demands are shown for the period from January to May.

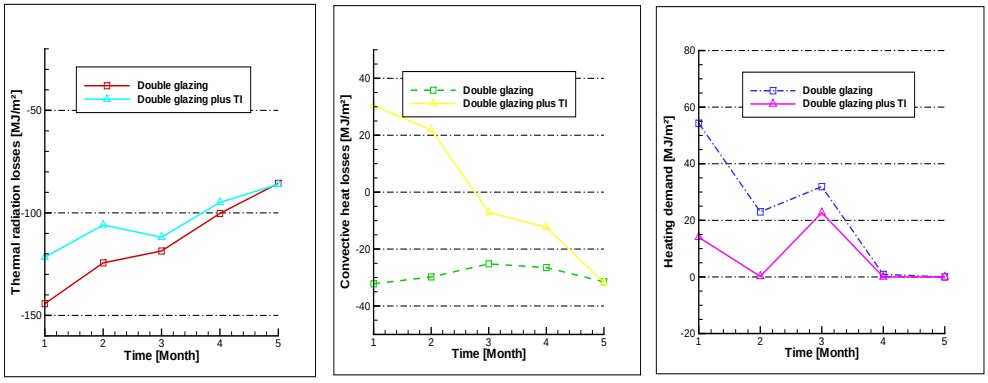

Figure 4.19: Thermal radiation losses, convective heat losses and heating demand for a double window with low-ϵ and a double window plus TIM, in MJ/m^2 for climatic conditions corresponding to Geneve city. Monthly integrated values.

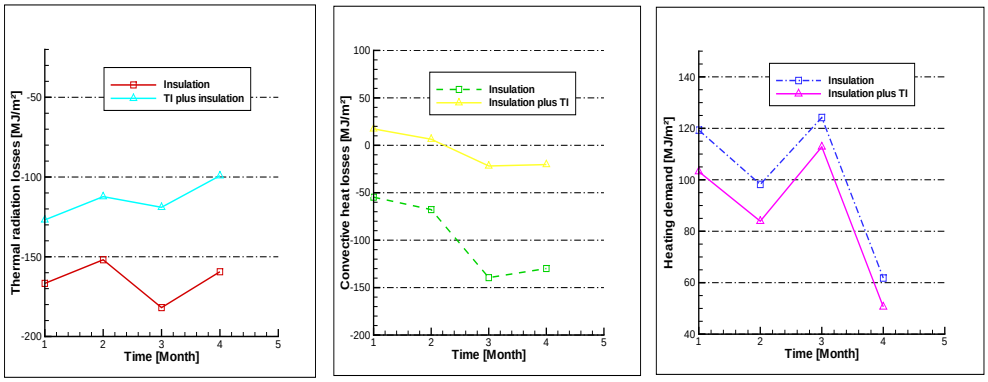

Figure 4.20: Thermal radiation losses, convective heat losses and heating demand for an insulation wall and a double skin including glass with TIM, air channel and insulation in MJ/m^2 for climatic conditions corresponding to Geneve city. Monthly integrated values.

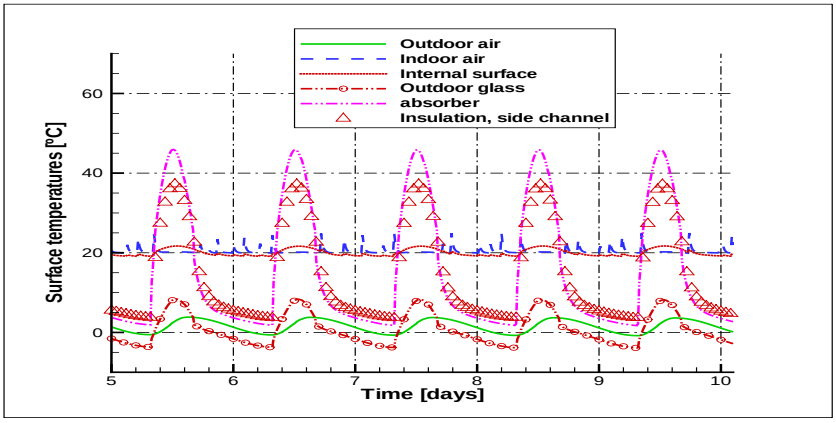

Figure 4.21: Outdoor, indoor air and surface temperatures at different elements of the TIM-insulation double skin facade for five January days.

In the case of opaque facades, the reduction of heat losses is even more noticeable since the effect of internal solar gains is not present. They are represented in Figure 4.20.

The presence of TIM allows to reduce heating demand from 54 to 14 MJ/m^2, for January month and almost totally for February in the case of direct gain systems. In the indirect systems the reduction is less remarkable (from 120 to 103 MJ/m^2 in January), since the no existence of direct solar gains produces a larger heating demand.

Figure 4.21 shows the evolution of temperatures at different surfaces of the double skin facade: outdoor glass, absorber and internal insulation (at both sides) for five January consecutive days. Outdoor air mean temperature is 1.4°C, while absorber temperature rises 45°C. Internal wall surface temperature is 22°C and indoor air temperature is maintained around 20.5°C. Peak incident solar radiation during these days is around 280 W/m^2, total daily radiation is around $6.4MJ/m^2$ ($1.7kW-h/m^2$).

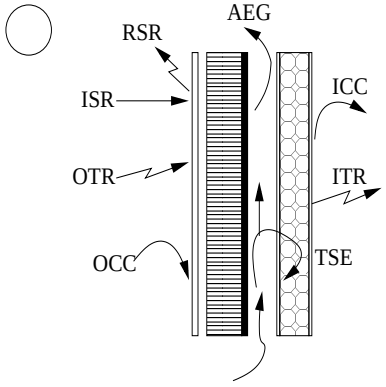

Figure 4.22: Global heat fluxes in a double skin facade

Figure 4.22 shows the global heat fluxes which determinate the thermal behaviour in any double skin facade.

As stated in Chapter 2, the energetic balance at the external skin is determined by equation 4.5.

$$FOG = OTR + OCC + I - RSR \tag{4.5}$$

$$FOG = \epsilon_o(\sigma(F_{f-g}(\epsilon_g T_g^4 + (1-\epsilon_g)T_{sky}^4) + (1-F_{f-g})T_{sky}^4) - \sigma T_{wo}^4) + h_o(T_a - T_{wo}) + I(1-R_s). \tag{4.6}$$

In the internal skin, the following balance must be accomplished:

$$FIG = ICC + ITR. \tag{4.7}$$

$$FIG = h_i(T_{wi} - T_i) + \epsilon_i\sigma(T_{wi}^4 - T_{walls}^4). \tag{4.8}$$

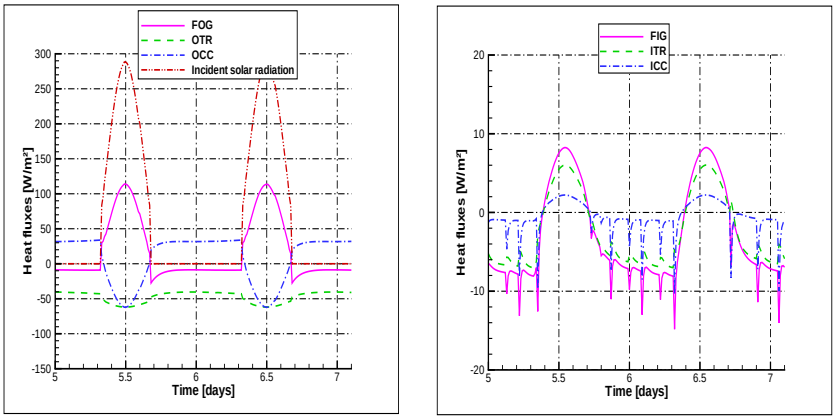

Figure 4.23: Main heat fluxes produced in the TIM-insulation double skin facade. At left, total outdoor heat flux FOG, and external heat fluxes due to thermal radiation (OTR) and convection (OCC). At right, total indoor heat flux FIG, and internal heat fluxes due to thermal radiation (ITR) and convection (ICC) for two January days.

.

The main heat fluxes conforming the outdoor and indoor gains produced during two January days for the case of the double skin facade including TIM plus insulation are shown in Figure 4.23.

The global heat balance of the facade will be:

$$FOG = FIG + AEG + TSE. \tag{4.9}$$

Variables of Equation 4.9 are shown in Figure 4.24.

The storage of energy in these facades (TSE) is produced only in the insulation wall and in air channel. No effects of accumulation are taken into account in the TIM layer. During nights, no air circulation is predicted in channel, and enthalpic gains (AEG) remain null. Air movement is induced by solar radiation and it begins in correspondence with the deflaction of stored energy. Internal heat gains (FIG) remain low as the combination of daily positive radiative (ITR), and convective (ICC) fluxes produced during the isolation hours (Figure 4.23) and heat losses during night.

It is possible to characterize these facades in function of a heat losses coefficient which may be defined as the ratio of total external heat losses $\overline{OTR} + \overline{OCC}$ to the incident solar radiation (Eq. 4.12). All these quantities integrated over a period of

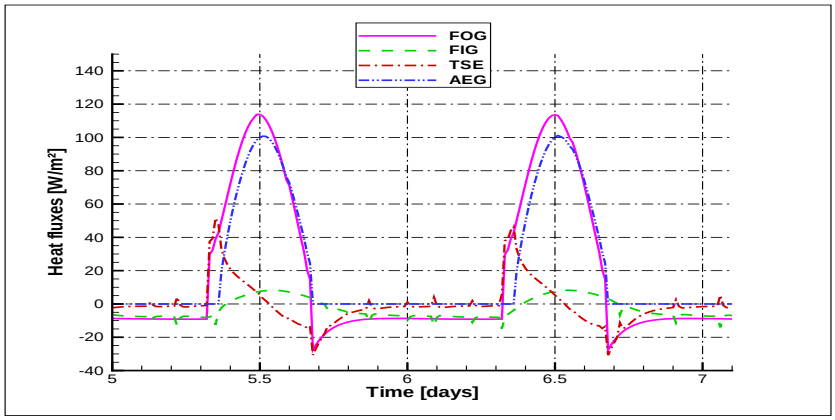

Figure 4.24: Heat fluxes involved in the global heat balance at the TIM-insulation double skin facade for two January days.

time (tipically one month).

$$\overline{OTR} = \int_{\tau=0}^{\tau_{end}} OTR dt \qquad \overline{OCC} = \int_{\tau=0}^{\tau_{end}} OCC dt \qquad \overline{I} = \int_{\tau=0}^{\tau_{end}} I dt. \tag{4.10}$$

For a double skin facade, the additional performance coefficient defined as the ratio of enthalpic gains to the incident solar radiation η_c (Eq.4.13), introduced in Chapter 2, is also a characterization parameter.

$$\zeta_{el} = \frac{|\overline{OTR} + \overline{OCC}|}{\overline{I}}. \tag{4.11}$$

$$\zeta_{el} = \frac{\int_{\tau=0}^{\tau_{end}} |(\epsilon_o(\sigma(F_{f-g}(\epsilon_g T_g^4 + (1-\epsilon_g)T_{sky}^4) + (1-F_{f-g})T_{sky}^4) - \sigma T_{wo}^4)) + (h_o(T_a - T_{wo}))| dt}{\overline{I}}. \tag{4.12}$$

$$\eta_c = \frac{\int_{t=0}^{t=t_{end}} [\sum_{j=1}^{j=CV} \dot{m} c_p (T_{j+1} - T_j)] dt}{\overline{I}}. \tag{4.13}$$

Table 4.14: Monthly integrated external heat losses coefficient ζ_{el} for different configurations of facades. Enthalpic heat gains coefficient η_c between brackets for the double skin facade.

Case	Double window	Double window plus TIM	Single insulation skin	Double skin: glass, TIM plus insulation (η_c)
January	0.89	0.46	1.11	0.55 (0.30)
February	0.76	0.42	1.09	0.52 (0.32)
March	0.46	0.38	1.04	0.45 (0.36)
April	0.45	0.38	1.02	0.42 (0.39)
May	0.41	0.41	–	–

From Table 4.14 it is observed that the heat losses are reduced drastically during the colder months, with the use of TIM. For this climatic data, differences are not noticeable from June month, since from this period outdoor temperatures are larger, and heat losses are not so relevant. In the case of an insulated single wall, monthly integrated heat losses are larger than incident solar radiation ($\zeta_{el} > 1$), by adding an external skin with TIM, heat losses are reduced in more than 50%.

4.7 Numerical parametric analysis of double skin TIM facades

A numerical analysis has been carried out of the incidence of different configuration parameters of TIM wall in a double skin facade. The parameters considered have been:

- The thickness of TIM panel
- The properties of the absorber sheet
- The thickness of air channel
- The presence of an air gap between external glass sheet and TIM panel.

These parameters have been analyzed in the following facade configurations:

1. The double skin facade with 0.05m TIM layer, which has been described as the third case in section 4.6, Table 4.12.
2. The same TIM facade of previous case with 0.10m of TIM.

3. The double skin facade with 0.05cm TIM layer, and a selective absorber with the following properties: $\alpha = 0.95$, $\epsilon = 0.10$, an air gap of 0.005m has been added between TIM and absorber.
4. The double skin of the first case with an air channel of 0.02m width.
5. The double skin of the first case with an air channel of 0.08m width.
6. The double skin of the first case without air gap between external glass and TIM.

In all the cases, the air channel has been considered opened and the air circulation through it is due to natural buoyancy forces, air enters to the channel to the outside air temperature, and it is heated mainly by the solar radiation absorbed by the absorber wall which is converted into convective gains in the air.

The main purpose of the designs analyzed will be to get a reduction of the heating load of a building by combining insulation plus the air channel flow which may be useful in different manner:

- To account a pre-heated air flow to help the heating system.
- To assure a ventilation of the room by using the chimney effect of the channel, taking air from indoors. A forced convection flow could be also implemented.
- To account an additional thermal resistance in cloudy days, or during nights proceeding to close the inlets and outlets of channel.
- To refresh the surface of the facade with outdoor cooler air during summer nights. In this case, a roller curtain between external glass sheet and TIM element would help to reduce unwished solar gains during summer days.

For the cases analyzed, indoor temperature is allowed to vary between 20 and 25°C, heating system is assumed to have a capacity of 2000 W, and the volume of air of the adjacent room has been considered 110 m^3. No internal generated gains have been foreseen, and a rate of air exchange has been fixed to 0.1 renovations per hour with external air. Heat transfer is produced only by the fenestration analyzed, the rest of the walls conforming the room are considered to be adiabatic. Numerical simulation has been performed for January month, considerering monthly climatic data of Geneve city [4].

Figure 4.25 shows the values of external losses due to thermal radiation (at left), and convection (right) for all the situations considered. The differences of heat losses among all the cases is given at noon, when external surface temperature is larger than outdoor air temperature. The case with lower heat losses is that with 2cm air channel

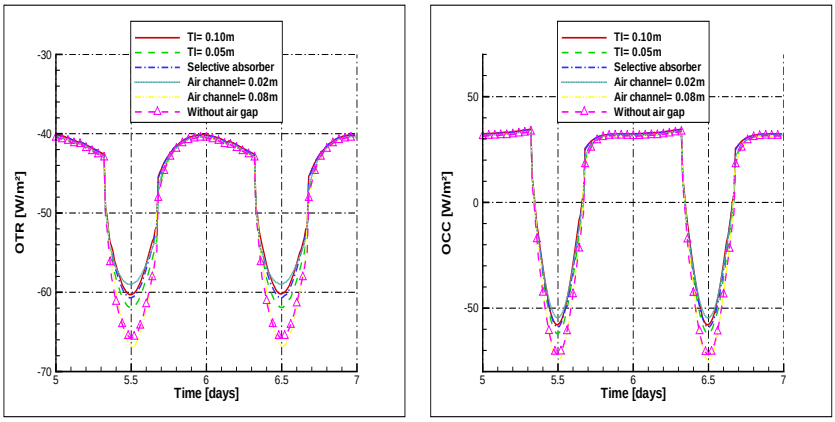

Figure 4.25: Thermal losses due to radiation (left) and convection (right) for different designs of a TIM-insulation double skin facade for two January days.

Table 4.15: Monthly integrated main variables for different configurations of double skin facades including TIM (MJ/m^2). January month.

Case	$\overline{HSD}$	$\overline{OTR}$	$\overline{OCC}$	$\overline{FOG}$	$\overline{FIG}$	$\overline{ITR}$	$\overline{ICC}$	$\overline{AEG}$	$\overline{TSE}$
TIM=0.05m	103.2	−126.9	17.3	53.5	−7.2	−5.7	−1.4	60.5	0.21
TIM=0.10m	100.5	−124.7	23.3	64.1	−4.6	−3.8	−0.7	68.2	0.48
Selective absorber	102.1	−125.3	21.7	56.5	−6.4	−5.2	−1.2	62.6	0.31
0.02m air channel	104.8	−125.1	22.1	60.4	−8.9	−7.1	−1.8	69.3	0.06
0.08m air channel	99.9	−130.1	9.2	41.5	−3.8	−3.3	−0.5	44.4	0.96
Without air gap	104.7	−129.9	9.3	42.9	−8.7	−6.9	−1.8	51.7	0.03

width. This case corresponds also to that with larger enthalpic gains as it is shown in Figure 4.26. This Figure shows that the larger absorber surface temperature at noon is produced for the case with 8cm air channel, whereas at night larger absorber obtained temperature is produced for the case with 10 cm TIM.

Table 4.15 shows the values of the heating demand $\overline{HSD}$, the heat losses by thermal radiation ($\overline{OTR}$) and convection ($\overline{OCC}$), the total external and internal gains ($\overline{FOG}$, $\overline{FIG}$), the internal thermal radiation ($\overline{ITR}$) and convection ($\overline{ICC}$), the enthalpic gains of air channel ($\overline{AEG}$), and the total stored energy ($\overline{TSE}$). All these values are integrated for the January month.

For January it is observed that the monthly integrated values of thermal radiation ($\overline{OTR}$) are negative, meaning that during this month, external thermal radiation

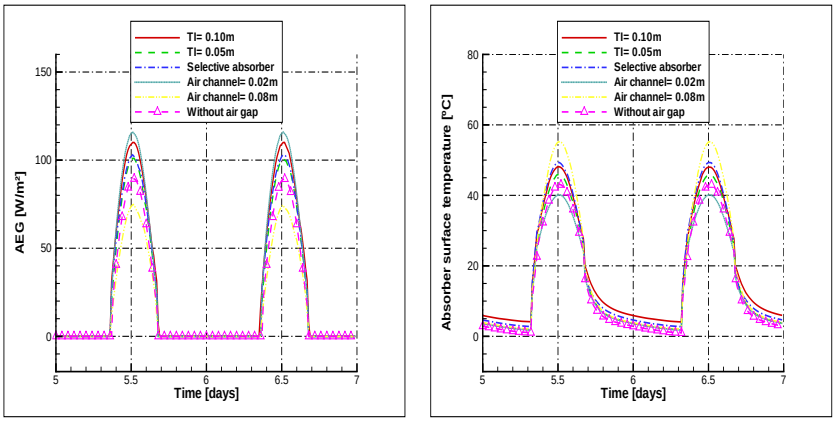

Figure 4.26: Enthalpic gains of air channel (left) and absorber surface temperature (right) for different designs of a TIM-insulation double skin facade for two January days.

represents always a heat loss. On the other side, integrated external convective heat flux ($\overline{OCC}$) is positive although instantaneously positive and negative values are produced as it is observed in Figure 4.25. Convective flux ($\overline{OCC}$) is positive at noon when glass external temperature is larger than outdoor air temperature, as can be seen in Figure 4.21, which corresponds to the first case analyzed.

Table 4.15 shows that the integrated values of each variable for the different options considered are quite similar, the optimum design would be that with 0.10m TIM between two air gaps combined with the selective absorber. These values indicate that an accurate numerical long term analysis is necessary for each climatic condition to choose the optimum design. Depending on climate, it might be possible to replace the good performance of a selective absorber with a thicker air gap.

Moreover, the efficiency of this facade design is not only related with its capacity of reducing heat losses but also with the possibility of obtaining a pre-heated air flux through facade channel, this parameter is linked with thickness of channel, and the level of walls temperatures arisen. This efficiency has been quantified by means of the enthalpic heat gains coefficient η_c. Table 4.16 shows the values of external heat losses coefficient ζ_{el} and enthalpic gains coefficient η_c for the cases analyzed during January months.

Table 4.16: Monthly integrated external heat losses coefficient ζ_{el} and enthalpic heat gains coefficient η_c for different configurations of double skin facades including TIM

Case	ζ_{el}	η_c
TIM=0.05m	0.55	0.31
TIM=0.10m	0.51	0.34
Selective absorber	0.52	0.32
0.02m air channel	0.52	0.35
0.08m air channel	0.61	0.22
Without air gap	0.61	0.26

4.8 Conclusions of the analysis of facades including transparent insulation

The use of transparent insulation materials in advanced facades of buildings allows to reduce thermal external losses in cold climates. It may be combined with an air channel in the case of double skin facades. In this case, an additional advantage is obtained since it is possible to account with an enthalpic gain that can be used for different applications.

The single skin facades have been analyzed as direct gain systems (double window and double window with TIM). A reduction of approximately 50% of heat losses (in the conditions of the numerical experiment) has been obtained, which is translated in a saving of 74% of heating demand in January month. On February, heating demand is almost reduced completely. For indirect gain systems (TIM layer with internal insulation and an insulated wall), the reduction of heating demand is lower, it is about 13% during January month.

The parametric analysis of double skin facades including TIM shows that increment on the thickness of TIM produces a reduction of heat losses. The increment of air channel width produces an increment of heat losses since the temperatures are also higher. When a selective absorber is applied, the effect is similar to increasing the thickness of TIM.

The parametric study shows that an accurate long term performance analysis is necessary to achieve the most suitable designs for a given climatic condition. Since the effects of properties or geometrical parameters produce differentiated transient behaviours, during day and night and at different periods of the year, a transient analysis is essential.

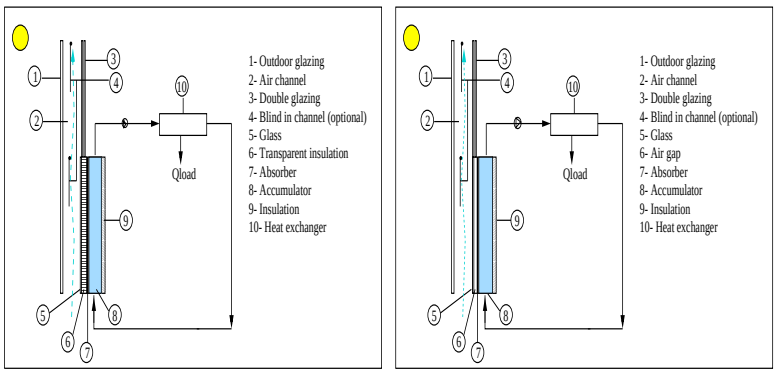

(a) (b)

Figure 4.27: Schematic design of the implementations analysed in a double skin facade, in this case for a space heating application: a)MF1 (with TIM), b)MF2 (without TIM)

4.9 Numerical analysis of facades with integrated collectors-accumulators

4.9.1 Variants considered

The integrated collector-accumulator has been modelled within *AGLA* code, with different boundary conditions according to the geometry. The following variants are foreseen:

- With and without transparent insulation
- With and without indoor insulation
- Implemented in a single skin facade
- Implemented in a double skin facade
- With and without reflective blinds in channel or in the outdoor side of facade (depending on the implementation).

The idea consists in using opaque internal areas of south facades, to incorporate solar collector-accumulator devices whose objective would be helping to find the heating and domestic hot water requirements.

The facade-integrated solar collectors should be optimised to: i)Reduce thermal losses, ii)Increment solar gains, iii)Contribute to reduce the DHW load and iv) Contribute to reduce the space heating load.

In order to reduce thermal losses, transparent insulation is located between glass and absorber surface of the solar collector. Depending on the climatic conditions, the transparent insulation may be avoided in double skin facades, with a suitable strategy of channel performance. Figure 4.27 shows a possible implementation of the integrated collectors in double skin facades, for space heating applications. The case with transparent insulation between glass and absorber is called MF1, MF2 is the name given to the design without TIM.

Figure 4.28 shows an schematic design of a collector-integrated facade for domestic hot water provision in a single skin facade. The cases shown here are called MF4 and MF6. The difference between them is the presence or not of transparent insulation between external glass and absorber cover.

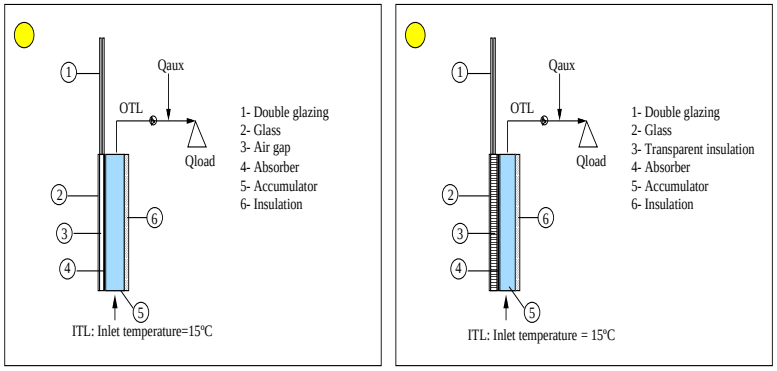

(a) (b)

Figure 4.28: Schematic design of the implementations analysed in a single skin facade, in this case for a domestic hot water application: a)MF4 (without TIM), b)MF6 (with TIM)

4.9.2 A steady approach

At the absorber surface, solar radiation impinging from outdoors and partially reduced by optical losses in external glass cover, is absorbed and converted into useful energy thermal gains and thermal losses. In a typical collector, losses are higher than in the integrated collector, since in this last case, the bottom losses are really thermal gains to the fluid. Additionally, thermal losses from fluid accumulator, are converted

into internal building gains. Assuming some hypothesis as: i)Steady state and ii)One dimensional heat flow; the overall heat loss coefficient of different facade designs is calculated. This parameter serves as a guide to easy compare different designs.

With the hypothesis assumed, it is possible to calculate useful energy gains by equation 4.14.

$$Qu = A_c S - A_c U_L (T_p - T_a). \tag{4.14}$$

Where Qu represents the useful energy gains in Watts, A_c stands for the collector area, S represents the absorbed solar energy, T_p is the absorber plate temperature, T_a is the outdoor ambient temperature and U_L stands for the overall heat loss coefficient.

The thermal losses Q_{loss} are defined by the second term of the previous equation, as stands in equation 4.15.

$$Q_{loss} = A_c U_L (T_p - T_a). \tag{4.15}$$

The overall heat loss coefficient U_L has been numerically calculated using $AGLA$ code, with the following restrictions:

- Outdoor ambient temperature and absorber plate temperature (T_a and T_p) are imposed and fixed as constants.
- Solar radiation is kept null, thermal losses are calculated from a fixed absorber plate temperature.
- Accumulation terms are made null (steady state).

In these conditions, heat flow from absorber surface is calculated using the standards subroutines implemented in $AGLA$, and U_L may be determined (equation 4.16):

$$U_L = \frac{h_o(T_a - T_{wo}) + \epsilon_o(\sigma(F_{f-g}(\epsilon_g T_g^4 + (1-\epsilon_g)T_{sky}^4) + (1-F_{f-g})T_{sky}^4) - \sigma T_{wo}^4)}{A_c(T_p - T_a)}. \tag{4.16}$$

For all the cases, outdoor ambient temperature T_a has been fixed in $20°C$, the collector area A_c has been considered equal to $1m^2$.

Cases analyzed

The variants introduced are summarized in Table 4.17. For the glass and absorber surface, ϵ_{ti} represents the thermal emissivity in the indoor side, ϵ_{to} stands for the thermal emissivity in the outdoor side, while ϵ_t indicates that thermal emissivity is the same at both sides.

Table 4.17: Thermo-physical properties of the situations considered.

MF1:	
Case	Description
1	Outdoor glass: ϵ_t=0.84, TIM glass: ϵ_t=0.84, Absober plate: ϵ_{ti}=0.5, ϵ_{to}=0.84
2	Outdoor glass: ϵ_t=0.5 , TIM glass: ϵ_t=0.84, Absober plate: ϵ_{ti}=0.5, ϵ_{to}=0.84
3	Outdoor glass: ϵ_t=0.1 , TIM glass: ϵ_t=0.84, Absober plate: ϵ_{ti}=0.5, ϵ_{to}=0.84
4	Outdoor glass: ϵ_t=0.84, TIM glass: ϵ_{ti}=0.5, ϵ_{to}=0.84 , Absober plate: ϵ_{ti}=0.5, ϵ_{to}=0.84
5	Outdoor glass: ϵ_t=0.84, TIM glass: ϵ_{ti}=0.84,ϵ_{to}=0.5, Absober plate: ϵ_{ti}=0.5, ϵ_{to}=0.84
6	Outdoor glass: ϵ_t=0.84, TIM glass: ϵ_t=0.84, Absober plate: ϵ_{ti}=0.5, ϵ_{to}=0.1
MF2:	
1	Outdoor glass: ϵ_t=0.84, Indoor glass: ϵ_t=0.84, Absober plate: ϵ_t=0.5
2	Outdoor glass: ϵ_t=0.5 , Indoor glass: ϵ_t=0.84, Absober plate: ϵ_t=0.5
3	Outdoor glass: ϵ_t=0.1 , Indoor glass: ϵ_t=0.84, Absober plate: ϵ_t=0.5
4	Outdoor glass: ϵ_t=0.84, Indoor glass: ϵ_{ti}=0.5, ϵ_{to}=0.84 , Absober plate: ϵ_t=0.5
5	Outdoor glass: ϵ_t=0.84, Indoor glass: ϵ_{ti}=0.1, ϵ_{to}=0.84, Absober plate: ϵ_t=0.5
6	Outdoor glass: ϵ_t=0.84, Indoor glass: ϵ_t=0.84, Absober plate: ϵ_{to}=0.1
MF4:	
1	Outdoor glass: ϵ_t=0.84, Absober plate: ϵ_t=0.8
2	Outdoor glass: ϵ_t=0.5 , Absober plate: ϵ_t=0.8
3	Outdoor glass: ϵ_t=0.1 , Absober plate: ϵ_t=0.8
MF6:	
1	Outdoor glass: ϵ_t=0.84, Absober plate: ϵ_t=0.5
2	Outdoor glass: ϵ_t=0.5 , Absober plate: ϵ_t=0.5
3	Outdoor glass: ϵ_t=0.1 , Absober plate: ϵ_t=0.5

The results obtained for the double skin facade are shown in Figure 4.29, and for the single skin facade in Figure 4.30.

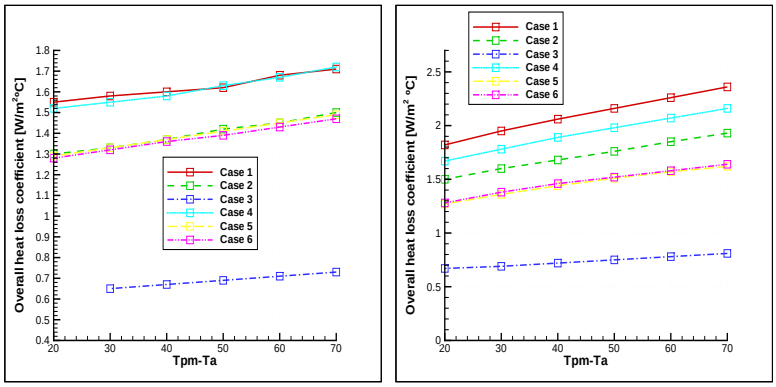

Figure 4.29: Overall heat loss coefficient a)MF1 case b)MF2 case.

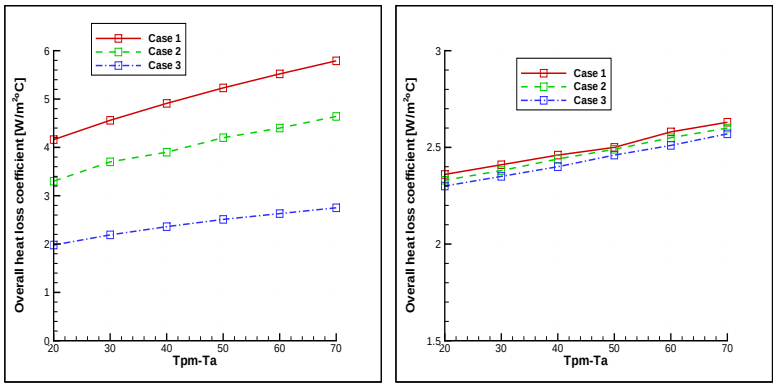

Figure 4.30: Overall heat loss coefficient a)MF4 case b)MF6 case.

Conclusions about the steady analysis

A good way to reduce thermal losses is the application of a low-ϵ coating on the surfaces of the elements conforming the envelope (glasses or absorber surfaces). From the above figures it may be deduced that there are no changes when this coating is applied on opposite surfaces (curves for cases 5 and 6 in Figure 4.29). It may be also

observed that overall heat loss coefficient is dependent on temperature, increasing its value with higher differences of temperatures. Several conclusions may be drawn:

- The presence of an additional glass in the case of double envelope facades, helps to reduce thermal losses.
- In the case of double envelopes, the application of the coating produces more outstanding effects when it is applied in the internal surface of the outdoor glass (or in the external surface of the second glass). This feature is valid in cases with or without TIM.
- The application of a low-ϵ coating produces more outstanding effects in the case of double envelope implementations. In this case, the combination of TIM plus low-ϵ produces the lower values of overall heat transfer coefficient.

The mean values obtained for the different configurations are summarized in Table 4.18 for cases 1 and 3.

Table 4.18: Overall heat loss coefficient for the different configurations U_L $(W/m^{2^\circ}\mathrm{C})$

	Double envelope		Single envelope	
	With TIM	Without TIM	With TIM	Without TIM
	MF1	MF2	MF6	MF4
Case 1	1.68	2.20	2.50	5.2
Case 3	0.70	0.75	2.38	2.4

4.9.3 Parametric analysis

The designs MF1, MF2, MF4 and MF6 were numerically tested for domestic hot water and space heating use. The thermo-physical properties of the elements conforming the facade were adopted from the analysis of the minimun overall heat loss coefficient.

In the case of domestic hot water use, water stored in the facade is warmed by solar energy and it is delivered to the domestic hot water network according to the consumer demand. When there is consumption, water is considered to enter to the facade at a constant inlet temperature equal to 15°C. Top temperature at tank is considered to be the delivery temperature to the load. No heat losses through the pipes are considered. The demand temperature is adopted constant and equal to 43°C.

On the other hand, when the facade is applied to help the space heating system, the top part of the tank in the facade is considered linked to a heat exchanger. Water

from tank, is pumped through the heat exchanger, delivering heat to the annex room, then it returns to the facade entering at bottom.

The following parameters were tested:

- ICS storage capacity
- Storage volume/collector area ratio
- Collector heat loss coefficient
- Space heating consumption and hot water draw profiles

Different collector areas have been considered:
- 1 m^2 - 2 m^2 - 3 m^2 - 4 m^2 - 6 m^2
Storage volume per unit of collector area has varied:
- 20 l/m^2 - 50 l/m^2 - 150 l/m^2
These values represent total storage volume shown in Table 4.19.

Table 4.19: Collection area and total volume of the tested cases.

Collector area [m^2]	Total volume [l]		
Volume/coll.area ratio:	$20l/m^2$	$50l/m^2$	$150l/m^2$
1	20	50	150
2	40	100	300
3	60	150	450
4	80	200	600
6	120	300	900

Domestic hot water and space heating loads estimation

In all the cases analyzed for space heating, a typical residential unit of 90 m^2 of habitable surface, and a volume equal to 225m^3 has been considered. The global heat loss coefficient includes the losses by ventilation, considering an air renovation rate equal to 1 renovation by hour, 13 m^2 of window surface, 45 m^2 roof surface, external walls surface equal to 126.5 m^2, and a perimeter equal to 27 m.

Assuming that indoor temperature remains constant, and taking the monthly average ambient temperature as a representative value for heating load calculation, it is possible to calculate heat losses (Q_{loss}) from the building as:

$$Q_{loss} = UA \cdot DD. \tag{4.17}$$

Where UA is the global heat loss coefficient in $W/^{\circ}C$, and DD represents the degree days (sum of all the positive terms for each month of the temperature difference between indoor temperature and the daily average ambient temperature), [5].

Thus, heating load has been estimated from the global heat loss coefficient of the building and the degree-days with base 15. Global heat loss coefficient is estimated assuming steady state and constant thermo-physical properties of the materials. This coefficient has considered buildings with different insulation levels and architecture implementations [6], as shown in Table 4.20.

Table 4.20: Values of the global heat loss coefficient for different building types ($W/m^{3\circ}C$)

	Building types:		
Insulation level	Detached	Attached	Residential collective
Basic	2.11	1.46	0.885
Insulated	1.17	0.89	0.647
Well insulated	0.586	0.461	0.360

Heating load for the different building types (equation 4.17) is represented in Table 4.21.

Table 4.21: Heating load for different building types for Barcelona city (MJ/month), calculated according expression 4.17.

Building type	Jan.	Feb.	Mar.	Abr.	May	Oct.	Nov.	Dec.
Detached:								
Basic	6234.8	4676.1	3158.42	2050.92	82.04	205.09	2297.03	4799.15
Insulated	3493.32	2619.99	1769.64	1149.12	45.96	114.91	1287.01	2688.94
Well insulated	1731.56	1298.67	877.17	569.59	22.78	56.96	637.94	1332.85
Attached:								
Basic	4314.12	3235.59	2185.44	1419.12	56.76	141.91	1589.41	3320.74
Insulated	2629.84	1972.38	1332.22	865.08	34.6	86.51	968.89	2024.29
Well insulated	1362.2	1021.65	690.06	448.09	17.92	44.81	501.86	1048.54
Residential:								
Basic	2615.07	1961.3	1324.74	860.22	34.41	86.02	963.45	2012.91
Insulated	1911.81	1433.86	968.48	628.88	25.16	62.89	704.35	1471.59
Well insulated	1063.76	797.82	538.88	349.92	14	34.99	391.91	818.81

In the cases applied to domestic hot water contribution, demand temperature (T_{demand}) is fixed to 43°C.

Performance parameters

If outlet temperature from tank is called T_{out} and inlet temperature T_{inl}, useful energy from facade to satisfy space heating or domestic hot water load, is calculated as:

$$Qload = \dot{m}c_p(T_{out} - T_{inl}). \tag{4.18}$$

Domestic hot water load will be:

$$Load = \dot{m}c_p(T_{demand} - T_{inl}). \tag{4.19}$$

Then, auxiliary energy necessary to complement energy delivered by the facade will be:

$$Qaux = \dot{m}c_p(T_{demand} - T_{out}). \tag{4.20}$$

The following parameters will allow to characterize facade performance:

- Solar Efficiency (η_s): it is defined as the rate between the useful energy delivered by the facade and the solar radiation impinging over the facade.

$$\eta_s = \frac{Qload}{I}. \tag{4.21}$$

- Solar Fraction (φ_s): defined as the rate between the useful energy delivered by the facade and the total heating load, calculated according Table 4.21, for the cases applied to space heating. For the implementations designed to provide domestic hot water, it will be the rate between the useful energy delivered by the facade and the domestic hot water load (equation 4.19).

$$\varphi_s = \frac{Qload}{Qload + Qaux}. \tag{4.22}$$

Where $Qaux$ is the energy necessary to complement that delivered by the facade, for the application considered.

Domestic hot water

The cases tested can be summarized as follows:

- Case 1: Collector area= 1 m^2, Storage volume=20 l , stored volume per unit of collector area= 20 l/m^2, thickness of tank=0.02m.
- Case 2: Collector area= 1 m^2, Storage volume=50 l , stored volume per unit of collector area= 50 l/m^2, thickness of tank=0.05m.

- Case 3: Collector area= 1 m^2, Storage volume=150 l , stored volume per unit of collector area= 150 l/m^2, thickness of tank=0.15m.
- Case 4: Collector area= 2 m^2, Storage volume=40 l , stored volume per unit of collector area= 20 l/m^2, thickness of tank=0.02m.
- Case 5: Collector area= 2 m^2, Storage volume=100 l , stored volume per unit of collector area= 50 l/m^2, thickness of tank=0.05m.
- Case 6: Collector area= 2 m^2, Storage volume=300 l , stored volume per unit of collector area= 150 l/m^2, thickness of tank=0.15m.
- Case 7: Collector area= 3 m^2, Storage volume=60 l , stored volume per unit of collector area= 20 l/m^2, thickness of tank=0.02m.
- Case 8: Collector area= 3 m^2, Storage volume=150 l , stored volume per unit of collector area= 50 l/m^2, thickness of tank=0.05m.
- Case 9: Collector area= 3 m^2, Storage volume=450 l , stored volume per unit of collector area= 150 l/m^2, thickness of tank=0.15m.
- Case 10: Collector area= 4 m^2, Storage volume=80 l , stored volume per unit of collector area= 20 l/m^2, thickness of tank=0.02m.
- Case 11: Collector area= 4 m^2, Storage volume=200 l , stored volume per unit of collector area= 50 l/m^2, thickness of tank=0.05m.
- Case 12: Collector area= 4 m^2, Storage volume=600 l , stored volume per unit of collector area= 150 l/m^2, thickness of tank=0.15m.
- Case 13: Collector area= 6 m^2, Storage volume=120 l , stored volume per unit of collector area= 20 l/m^2, thickness of tank=0.02m.
- Case 14: Collector area= 6 m^2, Storage volume=300 l , stored volume per unit of collector area= 50 l/m^2, thickness of tank=0.05m.
- Case 15: Collector area= 6 m^2, Storage volume=900 l , stored volume per unit of collector area= 150 l/m^2, thickness of tank=0.15m.

Two consumption profiles were tested [7], profile 1 presents water use at noon, whereas profile 2 does not. They are described in Table 4.22 and Table 4.23

Table 4.22: Water consumption profile 1-With noon draw

Time		Use	Flow rate		Total [l]
From:	To:		[l/min]	[kg/s]	
8:00	8:15	Shower	5	0.083	72
8:15	8:30	Face and washing hands	1.9	0.03	27.36
13:30	13:45	Food preparation	2.0	0.0331	28.80
15:00	15:15	Hand dishwashing	1.04	0.0182	14.976
19:00	19:15	Clothes washing	4.48	0.074	64.504
20:00	20:15	Face and washing hands	1.9	0.03	27.36
				Total:	235

Table 4.23: Water consumption profile 2 - Without noon draw

Time		Use	Flow rate		Total [l]
From:	To:		[l/min]	[kg/s]	
8:00	8:15	Shower	5	0.083	72
8:15	8:30	Face and washing hands	1.9	0.03	27.36
19:00	19:30	Food + hand dishwashing	3.75	0.062	108
19:30	19:45	Face and washing hands	1.9	0.03	27.36
				Total:	235

Numerical results for domestic hot water applications

The cases described in section 4.9.3 were numerically tested, the annual average solar fraction, solar efficiency and total useful energy are shown in Table 4.24.

Table 4.24: Average annual solar fraction, solar efficiency, outlet temperature and total annual useful energy for the variants analyzed

MF1:	Consumption profile 1				Consumption profile 2			
Case	$Qload[MJ/m^2]$	$T_{out}[^\circ C]$	φ_s	η_s	$Qload[MJ/m^2]$	$T_{out}[^\circ C]$	φ_s	η_s
Case 1	2007.57	24.23	0.2	0.49	1448.41	30.96	0.14	0.35
Case 2	2120.24	21.95	0.21	0.52	1957.92	23.74	0.19	0.48
Case 3	2198.58	21.47	0.22	0.54	2186.95	21.37	0.22	0.53
Case 4	1798.61	28.29	0.36	0.44	1446.61	31.96	0.29	0.35
Case 5	1938.88	26.13	0.39	0.47	1861.51	26.53	0.38	0.45
Case 6	1952.64	25.93	0.39	0.48	1962.8	25.89	0.4	0.48
Case 7	1611.8	31.99	0.49	0.39	1396.21	33.44	0.42	0.34
Case 8	1778.98	29.78	0.54	0.43	1715.18	29.37	0.52	0.42
Case 9	1767.79	29.82	0.53	0.43	1772.17	29.78	0.54	0.43
Case 10	1453.53	34.85	0.59	0.36	1318.83	35.26	0.54	0.32
Case 11	1618.94	32.73	0.65	0.4	1592.31	32.36	0.64	0.39
Case 12	1608.24	32.99	0.65	0.39	1614.51	33	0.65	0.39
Case 13	1188.46	39.64	0.72	0.29	1134.34	39.38	0.69	0.28
Case 14	1334.29	37.54	0.8	0.33	1320.93	37.73	0.8	0.32
Case 15	1345.06	37.75	0.81	0.33	1356.07	37.85	0.82	0.33
MF2:								
Case 1	2517.25	26.56	0.25	0.62	1863.25	34.87	0.24	0.46
Case 2	2687.31	23.8	0.27	0.66	2433.96	26.46	0.27	0.59
Case 3	2750.95	23.05	0.28	0.67	2746.54	22.92	0.28	0.67
Case 4	2202.27	33.15	0.45	0.54	1952.71	36.83	0.4	0.48
Case 5	2416.64	29.45	0.49	0.59	2307.3	30.48	0.47	0.56
Case 6	2486.96	29.07	0.5	0.61	2445.84	28.89	0.5	0.6
Case 7	1905.74	37.92	0.58	0.47	1801.04	40.44	0.55	0.44
Case 8	2170.25	34.37	0.66	0.53	2118.62	34.92	0.65	0.52
Case 9	2216.81	33.8	0.67	0.54	2259.88	33.86	0.69	0.55
Case 10	1687.09	42.29	0.69	0.41	1644.04	44.07	0.67	0.4
Case 11	1922.45	38.91	0.78	0.47	1890.21	39.27	0.77	0.46
Case 12	2012.11	37.83	0.82	0.49	1998.9	37.72	0.81	0.49
Case 13	1375.27	49.85	0.84	0.34	1312.9	50.7	0.8	0.32
Case 14	1506.53	46.46	0.92	0.37	1489.74	46.58	0.91	0.36
Case 15	1601.92	46.17	0.97	0.39	1595.14	46.35	0.97	0.39
MF4:								
Case 1	2351.94	25.47	0.23	0.58	1709.26	32.06	0.17	0.42
Case 2	2574.83	23.34	0.26	0.63	2355.03	25.35	0.24	0.58
Case 3	2665.45	22.74	0.27	0.65	2656.11	22.63	0.27	0.65
Case 4	1995.06	30.5	0.4	0.49	1666.91	33.39	0.34	0.41
Case 5	2270.5	27.94	0.46	0.56	2188.76	28.42	0.44	0.54
Case 6	2309.36	27.97	0.47	0.56	2320.34	27.83	0.47	0.57
Case 7					1578.15	35.2	0.48	0.39
Case 8	2005.24	31.73	0.61	0.49	1980.59	31.74	0.6	0.48
Case 9	2016.78	31.94	0.61	0.49	2027.5	31.85	0.62	0.5
Case 10	1549.03	36.81	0.63	0.38	1460.12	37.28	0.59	0.36
Case 11	1768.93	34.97	0.72	0.43	1756.65	35	0.71	0.43
Case 12	1783.95	35	0.72	0.44	1791.87	34.95	0.73	0.44
Case 13	1205.69	41.61	0.73	0.3	1179.63	41.65	0.72	0.29
Case 14	1372.24	40.24	0.83	0.34	1356.84	40.41	0.83	0.33
Case 15	1423.63	39.68	0.87	0.35	1422.31	39.73	0.87	0.35
MF6:								
Case 1	1992.94	23.94	0.2	0.49	1468.38	30.08	0.15	0.36
Case 2	2161.26	21.98	0.22	0.53	1988.33	23.83	0.2	0.49
Case 3	2237.93	21.5	0.23	0.55	2228.57	21.41	0.23	0.54
Case 4	1726.24	27.47	0.35	0.42	1403.57	30.93	0.28	0.34
Case 5	1893.8	25.8	0.38	0.46	1827.64	26.29	0.37	0.45
Case 6	1921.96	25.8	0.39	0.47	1929.63	25.69	0.39	0.47
Case 7	1580.8	29.41	0.46	0.39	1324.05	32.07	0.4	0.32
Case 8	1668.88	28.79	0.51	0.41	1648.94	28.83	0.5	0.4
Case 9	1670.42	29.04	0.51	0.41	1673.29	28.93	0.51	0.41
Case 10	1329.51	32.61	0.54	0.33	1230.7	33.39	0.5	0.3
Case 11	1483.63	31.18	0.6	0.36	1478.97	31.13	0.6	0.36
Case 12	1471.3	31.51	0.6	0.36	1475.75	31.46	0.6	0.36
Case 13	1069.46	35.91	0.65	0.26	1035.68	36.07	0.63	0.25
Case 14	1188.04	34.89	0.72	0.29	1186.07	34.89	0.72	0.29
Case 15	1183.93	34.98	0.72	0.29	1185.34	34.97	0.72	0.29

These data were represented graphically in Figures 4.31(a), 4.31(b) and 4.31(c) as a function of the rate between storage volume and collector area ratio and the collector area.

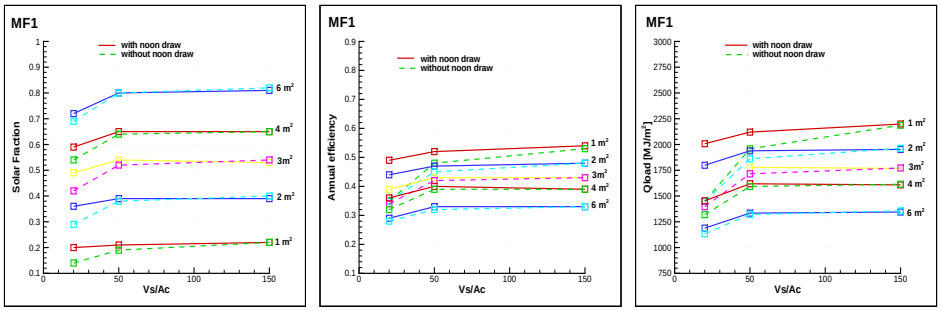

(a) (b) (c)

Figure 4.31: Average annual behaviour for MF1 case, considering two consumption profiles: a) Solar Fraction; b) Solar Efficiency; c)Total annual useful energy gains

In Figures 4.31, each pair of curves represents a collector area at varying storage volumes. Annual system solar fractions are dependent on sizing, larger collector areas produce larger solar fractions. Sufficient storage capacity is needed to achieve the maximum asymptotic solar fraction, from $50l/m^2$ the variation in the solar fraction is negligible, for both consumption profiles. For $20l/m^2$, the solar fraction is lower for the case without noon draw. The larger collection area produces higher temperatures in the accumulator.

Annual solar efficiency decays with increasing collector areas, due to the larger solar radiation available. For the smaller areas, solar efficiency is higher in the cases with noon draw. For the storage volume/collector area ratios lower than $50l/m^2$ the cases without noon draw have lower solar efficiency for the smaller areas.

Total annual useful energy gains reflect the same behaviour than solar fraction, it is notorious that the consumption profile with noon draw presents higher values of useful energy in the cases with smaller collector areas.

The monthly variation of solar fraction and useful energy gains in case 6, is shown in Figure 4.32. It is observed that solar fraction remains quite constant during all the year, with a mean value of 40% in this case. Useful energy ($QLOAD$) presents more variations, it is maximum in October with about 190 MJ/m^2, equivalent to 53 $Kw-h$. This Figure compares the solar fraction and useful energy for the same case (Case 6) implemented in a double skin facade, with (MF1) and without transparent insulation (MF2). It is observed that larger gains are produced for the case without TIM, this behaviour is due to the fact that the cover glass are different and therefore, these cases do not have equal solar gains. In the case with TIM, an additional glass is incorporated, and the complete transparent layer is responsible for lower solar gains. However, it has been chosen to show that it is possible to obtain similar gains, while

keeping lower thermal losses, with a transparent layer without special features. All the glasses have a solar transmissivity equal to $\tau_s = 0.82$.

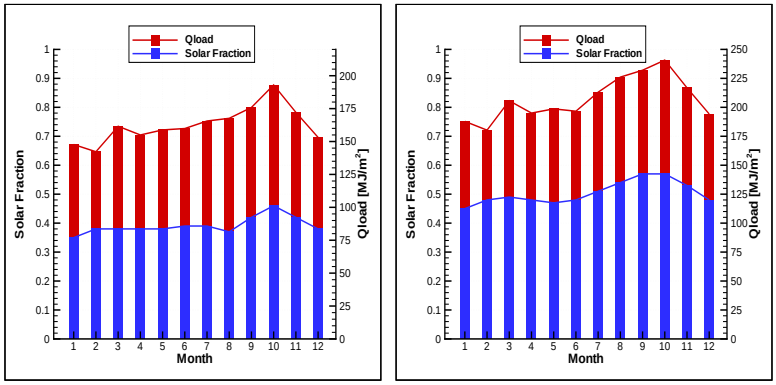

(a) (b)

Figure 4.32: Monthly Solar Fraction for case 6 ($2m^2$, $300l$) in a)MF1 case b)MF2 case

Figure 4.33 shows the annual average behaviour for the MF4 case (single skin implementation without TIM). This case presents the larger solar fraction in accordance with a transparent glass cover with larger solar transmittance $\tau_s = 0.85$.

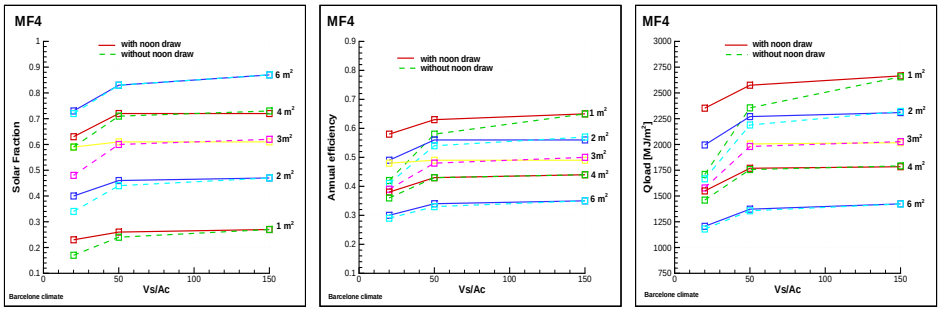

(a) (b) (c)

Figure 4.33: Average annual behaviour for MF4 case, considering two consumption profiles: a) Solar Fraction; b) Solar Efficiency; c)Total annual useful energy gains

Space heating

To analyse the performance of the design for space heating applications, the following assumptions have been considered:

-Indoor room temperature is considered constant and equal to 20°C.

-Global heat transfer coefficient of heat exchanger has been considered constant $UA = 200$ W/°C. Return temperature to the facade is calculated according to:

$$Qload = UA(\overline{T} - Tg) = \dot{m}c_p(T_{out} - T_{inl}) \tag{4.23}$$

where:

$$\overline{T} = 0.5(T_{out} + T_{inl}) \tag{4.24}$$

Tg is the indoor ambient temperature, T_{out} is the outlet water temperature from the facade, $\dot{m}$ is the water flow rate [kg/s], $Qload$ stands for the energy delivered from the heat exchanger and T_{inl} is the return temperature.

-The facade will deliver heat from 17 to 24 each day of the heating months.

The cases numerically tested, can be summarized as follows:

- Case 1: Collector area= 1 m^2, Storage volume=20 l , stored volume per unit of collector area= 20 l/m^2, thickness of tank=0.02m. Water is discharged each half hour from 17 to 24 hours. Mass flow rate= 0.011 kg/s.
- Case 2: Collector area= 1 m^2, Storage volume=50 l , stored volume per unit of collector area= 50 l/m^2, thickness of tank=0.05m. Water is discharged each half hour from 17 to 24 hours. Mass flow rate= 0.027 kg/s.
- Case 3: Collector area= 1 m^2, Storage volume=150 l , stored volume per unit of collector area= 150 l/m^2, thickness of tank=0.15m. Water is discharged each hour from 17 to 24 hours. Mass flow rate= 0.041 kg/s.
- Case 4: Collector area= 2 m^2, Storage volume=40 l , stored volume per unit of collector area= 20 l/m^2, thickness of tank=0.02m. Water is discharged each hour from 17 to 24 hours. Mass flow rate= 0.011 kg/s.
- Case 5: Collector area= 2 m^2, Storage volume=100 l , stored volume per unit of collector area= 50 l/m^2, thickness of tank=0.05m. Water is discharged each hour from 17 to 24 hours. Mass flow rate= 0.027 kg/s.
- Case 6: Collector area= 2 m^2, Storage volume=300 l , stored volume per unit of collector area= 150 l/m^2, thickness of tank=0.15m. Water is discharged each hour from 17 to 24 hours. Mass flow rate= 0.082 kg/s.
- Case 7: Collector area= 2 m^2, Storage volume=300 l , stored volume per unit of collector area= 150 l/m^2, thickness of tank=0.15m. Water is discharged once from 17 to 24 hours. Mass flow rate= 0.012 kg/s.

Numerical results for space heating applications

The monthly solar fraction obtained for each case and architectural implementation is given in Table 4.25.

In all these cases, the well insulated situations present the better behaviour within each building type. Additionaly, and according to their global heat loss coefficient given in Table 4.20, the solar fraction is higher for residential collective buildings, than for attached dwellings and this is at the same time higher than for detached buildings. When the collector area increases, the values of solar fraction become higher for all the configurations analysed, obtaining for the best case ($2m^2$, 300 l, good insulated residential building) a solar fraction equal to 32% in January, and 95% in April and November, in October no additional energy would be necessary. The worst of these cases is the basic detached building which presents a solar fraction equal to 6% in January and 16% in April and November.

The annual average values of solar efficiency (based on eight heating months, as shown in Table 4.25), solar fraction and total useful energy are shown in Figures 4.34(a), 4.34(b) and 4.34(c) as a function of the ratio between storage volume and collection area, for the case of an insulated detached dwelling.

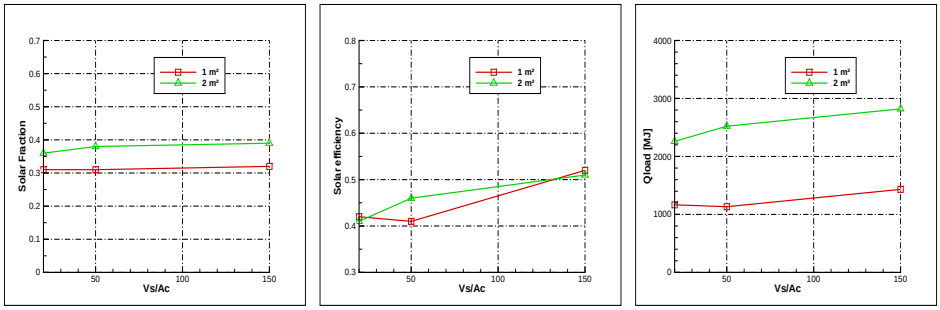

(a) (b) (c)

Figure 4.34: Annual average variables (based on eight heating months) for MF1 case, considering an insulated detached dwelling in Barcelona climatic conditions: a) Solar Fraction; b) Solar Efficiency; c) Total annual useful energy

From the above Figures, several conclusions may be drawn:

- Monthly solar fraction increases with the collector area, in April and November months, with $2m^2$ of collector area, approximately 30% of heating energy is produced by the facade. During October month, the facade is able to deliver the total energy necessary for heating.

Table 4.25: Monthly Solar Fraction of the different cases analyzed, according to the architectural implementation

Month	Detached: Basic	Detached: Insulated	Detached: Well Insulated	Attached: Basic	Attached: Insulated	Attached: Well Insulated	Residential collective: Basic	Residential collective: Insulated	Residential collective: Well Insulated
CASE 1:									
1	0.02	0.04	0.09	0.03	0.06	0.11	0.06	0.08	0.14
2	0.03	0.05	0.11	0.04	0.07	0.14	0.07	0.1	0.17
3	0.05	0.08	0.16	0.07	0.11	0.21	0.11	0.15	0.27
4	0.07	0.12	0.24	0.1	0.16	0.3	0.16	0.22	0.39
5	1	1	1	1	1	1	1	1	1
10	0.82	1	1	1	1	1	1	1	1
11	0.07	0.12	0.24	0.1	0.16	0.3	0.16	0.22	0.39
12	0.03	0.05	0.11	0.04	0.07	0.14	0.07	0.1	0.18
Average	0.26	0.31	0.37	0.3	0.33	0.4	0.33	0.36	0.44
CASE 2:									
1	0.03	0.05	0.09	0.04	0.06	0.12	0.06	0.08	0.15
2	0.03	0.06	0.11	0.04	0.07	0.14	0.07	0.1	0.18
3	0.04	0.06	0.13	0.05	0.08	0.16	0.08	0.12	0.21
4	0.06	0.1	0.2	0.08	0.13	0.26	0.13	0.18	0.33
5	1	1	1	1	1	1	1	1	1
10	0.61	1	1	0.89	1	1	1	1	1
11	0.08	0.14	0.28	0.11	0.18	0.35	0.18	0.25	0.45
12	0.03	0.06	0.12	0.05	0.08	0.15	0.08	0.11	0.19
Average	0.23	0.31	0.37	0.28	0.33	0.4	0.33	0.35	0.44
CASE 3:									
1	0.03	0.05	0.1	0.04	0.07	0.13	0.07	0.09	0.16
2	0.03	0.06	0.12	0.05	0.08	0.15	0.08	0.11	0.2
3	0.06	0.1	0.2	0.08	0.13	0.26	0.13	0.18	0.33
4	0.08	0.15	0.3	0.12	0.2	0.38	0.2	0.27	0.48
5	1	1	1	1	1	1	1	1	1
10	1	1	1	1	1	1	1	1	1
11	0.08	0.15	0.3	0.12	0.2	0.38	0.2	0.27	0.48
12	0.03	0.06	0.13	0.05	0.08	0.16	0.08	0.11	0.21
Average	0.29	0.32	0.39	0.31	0.34	0.43	0.34	0.38	0.48
CASE 4:									
1	0.04	0.08	0.16	0.06	0.1	0.2	0.1	0.14	0.26
2	0.05	0.1	0.2	0.08	0.13	0.25	0.13	0.18	0.32
3	0.09	0.16	0.33	0.13	0.22	0.42	0.22	0.3	0.54
4	0.13	0.24	0.48	0.19	0.32	0.61	0.32	0.44	0.78
5	1	1	1	1	1	1	1	1	1
10	1	1	1	1	1	1	1	1	1
11	0.13	0.23	0.47	0.19	0.31	0.6	0.31	0.43	0.77
12	0.06	0.1	0.2	0.08	0.13	0.26	0.14	0.18	0.33
Average	0.31	0.36	0.48	0.34	0.4	0.54	0.4	0.46	0.62
CASE 5:									
1	0.05	0.09	0.18	0.07	0.12	0.22	0.12	0.16	0.29
2	0.06	0.11	0.22	0.09	0.14	0.27	0.14	0.2	0.35
3	0.1	0.18	0.37	0.15	0.24	0.47	0.24	0.33	0.6
4	0.14	0.25	0.51	0.2	0.33	0.64	0.34	0.46	0.83
5	1	1	1	1	1	1	1	1	1
10	1	1	1	1	1	1	1	1	1
11	0.15	0.26	0.53	0.21	0.35	0.68	0.35	0.48	0.87
12	0.06	0.11	0.23	0.09	0.15	0.29	0.15	0.2	0.37
Average	0.32	0.38	0.5	0.35	0.42	0.57	0.42	0.48	0.66
CASE 6:									
1	0.06	0.1	0.2	0.08	0.13	0.25	0.13	0.18	0.32
2	0.07	0.12	0.24	0.09	0.16	0.3	0.16	0.21	0.38
3	0.11	0.2	0.4	0.16	0.26	0.51	0.27	0.36	0.65
4	0.16	0.29	0.59	0.24	0.39	0.75	0.39	0.53	0.95
5	1	1	1	1	1	1	1	1	1
10	1	1	1	1	1	1	1	1	1
11	0.16	0.29	0.59	0.24	0.39	0.74	0.39	0.53	0.95
12	0.07	0.12	0.25	0.1	0.16	0.32	0.16	0.22	0.4
Average	0.33	0.39	0.53	0.36	0.44	0.61	0.44	0.51	0.71
CASE 7:									
1	0.05	0.09	0.19	0.08	0.12	0.24	0.13	0.17	0.31
2	0.06	0.11	0.23	0.09	0.15	0.29	0.15	0.2	0.37
3	0.11	0.19	0.38	0.15	0.25	0.49	0.25	0.35	0.62
4	0.16	0.28	0.56	0.23	0.37	0.71	0.37	0.51	0.91
5	1	1	1	1	1	1	1	1	1
10	1	1	1	1	1	1	1	1	1
11	0.16	0.28	0.56	0.22	0.37	0.71	0.37	0.51	0.91
12	0.07	0.12	0.24	0.1	0.16	0.3	0.16	0.21	0.39
Average	0.32	0.38	0.52	0.36	0.43	0.59	0.43	0.49	0.69

- Annual average values of solar fraction show the same relationship with the collection area than monthly values. The maximum asymptotic value of solar fraction is achieved from $50l/m^2$. With 150 l/m^2 and $2m^2$, an average annual solar fraction of 40% is obtained.
- Solar efficiency does not vary so outstandingly with collector area, but it is quite sensible to storage volume/collector area ratio. It increases with the increment of Vs/Ac ratio.
- $Qload$ represents the total annual useful energy, it varies notoriously with collection area, and its increment is less noticeable from $50l/m^2$. The maximum value obtained is 2800 MJ equivalent to 777 $Kw-h$.

The solar fraction produced by each of the cases described previously, with different architectural implementations (as mentioned in Table 4.20) has been numerically investigated. Figure 4.35 shows the monthly solar fraction obtained for the different architectural implementations. The cases shown in this Figure correspond to the case 3 which has a storage volume of 150 l.

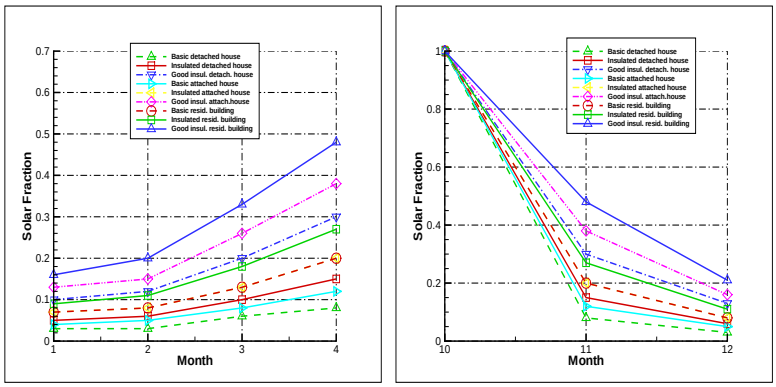

Figure 4.35: Monthly solar fraction for MF1, case 3, according to the architectural implementation: a) From January to April; b) From October to December

4.9.4 General conclusions from the facade designs with integrated collectors-accumulators

From the analysis carried out for the different variant designs, it may be generally concluded that:

- Annual solar fractions are dependent on sizing, evidently, larger collector areas produce larger solar fractions.
- The maximum asymptotic value of solar fraction is achieved (in the majority of cases) with 50 l/m^2. From this value, solar fraction increases slowly.All these cases were considered with south orientation.
- Annual solar efficiency is not so dependent on collection area, for all the cases. It is quite sensible to storage volume/collector area ratio. For values lower than 50 l/m^2 the DHW cases without noon draw have lower solar efficiency for smaller areas.
- For the DHW cases, annual solar fraction does not vary outstandingly with the consumption profile (with or without noon draw) with larger collection areas. When collector area is smaller, the cases with noon draw present larger solar fraction with storage volume/collector area ratios lower than 50 l/m^2.

Regarding the results for space heating contribution, according with the degree of insulation of a dwelling and its architecture implementation, different levels of solar fraction may be achieved for any climatic condition. In all the cases, the maximum monthly values corresponds to the higher level of insulation (the lower heat loss coefficient) and the larger collector area. Regarding to the volume managed, variations are not so outstanding from 50 l/m^2. For the considered climatic conditions, the best case corresponds to a good insulated residential building, whereas the worst to a basic detached dwelling.

From the results obtained, it may be concluded that the facades with integrated collectors-accumulators may result an attractive design to contribute to reduce energy consumption in buildings, however, their performance will be strongly dependent (as in any active system) on azymuth of the captating surfaces, optical properties of the materials and climatic conditions. Therefore, it is necessary to account with a numerical simulation tool in order to be able to predict the thermal behaviour in different conditions.

NOMENCLATURE

A_c	collector area (m^{-2})
c_p	specific heat (J kg^{-1} $^\circ K^{-1}$)
k	thermal conductivity (W m^{-1} $^\circ K^{-1}$)
S	absorbed energy (Wm^{-2})

T	temperature
t	time

Greek symbols:

α	solar absorptivity
ϵ_t	thermal emissivity
η_i	ratio of net gains to incident solar radiation
η_{ip}	ratio of positive internal gains to incident solar radiation
η_c	ratio of enthalpic gains to incident solar radiation
ρ	density (kg m^{-3})
τ	solar transmissivity

Acronyms:

AGLA	Advanced Glazed Facade Simulation Code
$SHGC_o$	Overall Solar Heat Gain Coefficient
TIM	Transparent Insulation Material
U_0	Overall Heat Transfer Coefficient

References

[1] Comerç i Turisme. Generalitat de Catalunya. Institut Català d'Energia. Departament d'Indústria. Atles de Radiació Solar a Catalunya. Technical report, 1995.

[2] D. Neeper. Thermal dynamics of wallboard with latent heat storage. *Solar Energy*, 68(5):393–403, 2000.

[3] ASHRAE. *ASHRAE HANDBOOK Fundamentals*. 1997.

[4] J. Remund, R. Lang, and S. Kunz. *METEONORM Version 4.00*, 1999.

[5] Comerç i Turisme. Institut Català d'Energia. Generalitat de Catalunya. Departament de Treball, Indústria. Els graus-dia de calefacció i refrigeració de Catalunya. Resultats a nivell municipal., 2003.

[6] A. Mitjà Sarvisé, J. Esteve Reyner, and J.J Escobar Sanchez. *Estalvi d'energia en el disseny d'edificis. Aplicació de sistemes d'aprofitament solar passiu*. Generalitat de Catalunya, 1986.

[7] C. Christensen, G. Barker, and J. Thornton. Parametric study of thermal performance of integral collector-storage solar water heaters. In *Proceedings of the 2000 American Solar Energy Society Annual Conference*, pages 261–266, 2000.

Chapter 5

Applications

5.1 Introduction

Numerical code $AGLA$ has been applied during the development of this thesis in numerous consultancy work to assist in the design of envelopes of singular buildings, such as the *Agbar Tower building* [1] in Barcelona, the central headquarters building of *Caixa Terrassa* in Terrassa city [2], the new building for the headquarters of *Association of Technical Engineers* in La Rioja [3], a new office building in Vilanova i la Geltru, the new building of the *Bishop of Terrassa* and punctual consultancy for different architecture offices and constructive companies.

In the majority of the cases, the outputs obtained by $AGLA$ have been useful in several manner:

- To help the engineering team in charge of the design of the HVAC system.
- To decide about the choice of the most convenient glasses, in external and internal skin, since this decision has to take into account not only the aesthetics requirements but also the energetic performance of the envelope in Summer and Winter periods.
- To help in the decission about the nature of the flow to be used in channel (forced vs natural convection).
- To numerically quantify the influence of bioclimatic strategies, such as the use of shadowing elements, thermal inertia, coatings, etc.
- In general, to have a complete outlook of the thermal performance of the facade, in terms of temperatures and heat fluxes through it.

In the following paragraphs, a summary of some aspects analyzed in these works will be outlined.

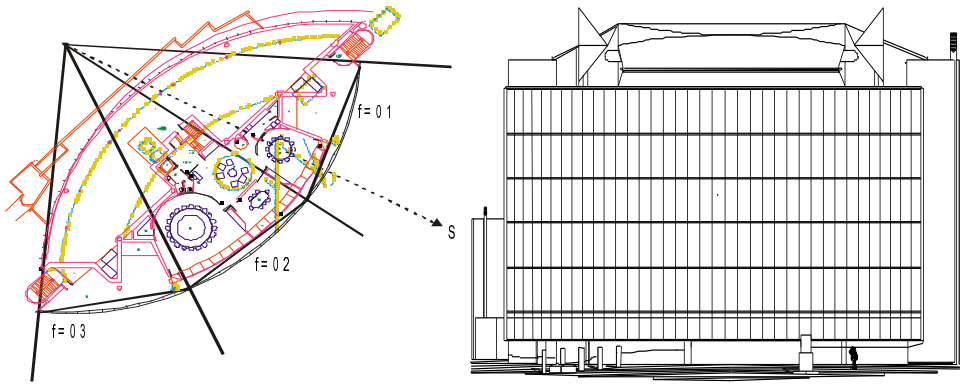

(a) (b)

Figure 5.1: Schematic plant of new building of *Caixa Terrassa*: a) Semi-circular facade was divided in three zones; b) External image of the building

5.2 *Caixa Terrassa* facade assistance design

This building is formed by a semi-circular glazed double envelope of approximately 1245 m^2, as shown in Figure 5.1. Internal skin presents opaque zones combined with large transparent areas. Movement of air in channel is achieved by means of a ventilation system (forced convection). In summer, air channel is used to renovate indoor air, cooling at the same time, the surface of the facade.

The facade was divided in three sections, with different azymuths. A lot of variables were studied, in order to predict channel behaviour, optimize external and internal glazing, optimize channel width, and predict temperatures and heat fluxes in standard and extreme meteorological conditions.

5.2.1 Analyzed aspects

The numerical analysis was carried out in order to assess the perfomance of the following aspects:

- Channel design: structure of channel, procedence of air (indoor or outdoor), convection regime (natural or forced)
- Interaction of channel with the ventilation system: an unique channel with total height or a channel by storey level.

Figure 5.2: Oudoor aspect of the building

- Bioclimatic strategies to reduce overheating or thermal losses: use of shadowing, blinds in channel, closed channel, etc
- Quantification of the improvement derived from the use of a ventilated channel.
- Help to the selection of suitable glazing and blinds.
- Help to the decision of geometric aspects, such as width of channel, mass flow rate, presence of shadowing, etc.
- Incidence of different aspects in HVAC system.
- Effect of extreme climatic conditions.

5.2.2 Air channel numerical study

This study was based on comparing the thermal performance (internal heat gains and losses through the facade) for a single skin (constituted by the internal skin of the original design) and the double skin with the introduction of changes in air channel geometry and air flow regime. The cases may be summarized as follows:

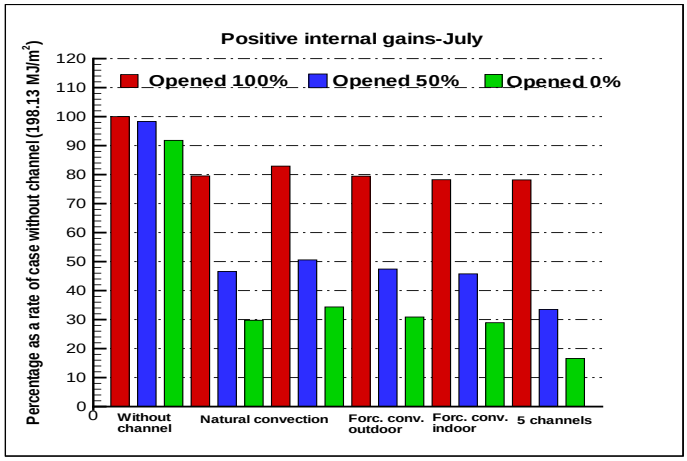

Figure 5.3: Internal gains obtained with the different variants during July month, with variable aperture degree of the blinds, as a percentage of the case without channel.

- Without air channel (single internal skin)
- An air channel of the total height of the building and width =0.10 m, with natural convection flow
- An air channel of the total height of the building and width =0.10 m, with natural convection flow and air filters in the inlet and outlet
- An air channel of the total height of the building and width =0.10 m, with forced convection flow, taking air from outdoors, and flow rate equivalent to one renovation in an hour of the indoor air.
- An air channel of the total height of the building and width =0.10 m, with forced convection flow, taking air from indoors, and flow rate equivalent to one renovation in an hour of the indoor air.
- Five air channels (one for each storey), 0.10 m width, taking air from indoors. Air flow rate equivalent to one renovation in an hour of the indoor air among the five channels.

A blind was included in all the cases, and its aperture degree was varied.

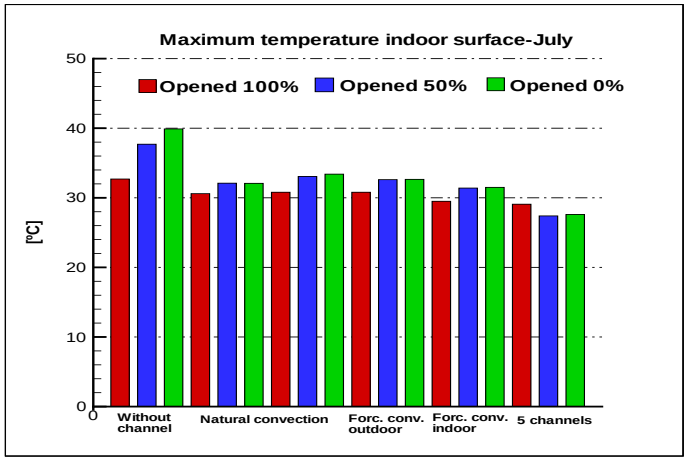

Figure 5.4: Maximum indoor surface wall temperature obtained for the different designs, with variable aperture degree of the blinds.

Figure 5.3 shows the internal positive gains integrated during July month, for the different cases, and aperture degree of the blind. The case without channel (single skin envelope) is the one which presents larger heat gains. When no blind is considered (red bar), internal gains are quite similar for all the double skin cases considered. When the blind is completely closed, internal gains are lower for a facade constituted by five channels (one for storey level). This is due to the lower level of temperatures of the internal surface for this case (as shown in Figure 5.4.) The air channel configuration applied in the building was that of forced convection, with the total height of the building, taking heat from indoors and with blinds in the channel.

5.2.3 Glazing numerical study

Different glazing systems were simulated in order to find the most adequated from the architectural and energetic point of view. Finally, three options were chosen in the last stages. These options are described by the following features:

- Case A: Non ventilated facade (California glass type): Double glazing with external 6 mm glass, with $\tau_s = 31\%$, $\rho_s = 24\%$, $\epsilon_t = 0.10$ in indoor surface, 12 mm air gap, indoor glass: 6mm, $\tau_s = 82\%$, $\rho_s = 7\%$, $\epsilon_t = 0.84$

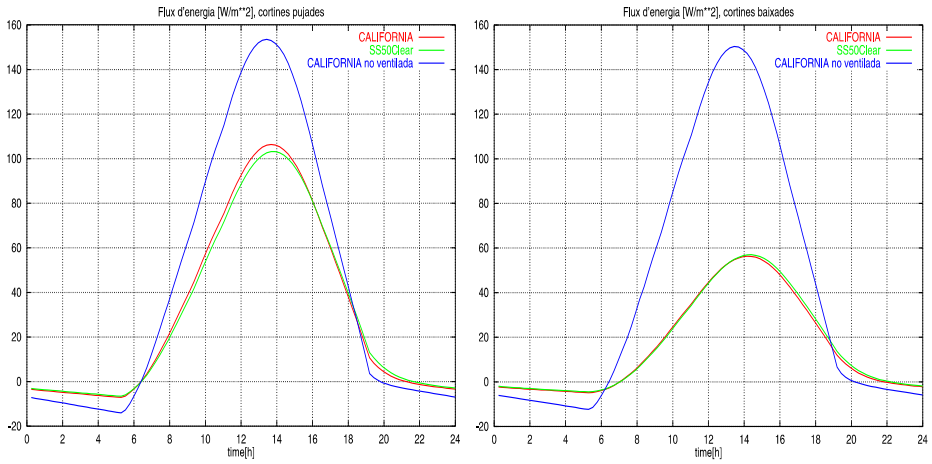

(a) (b)

Figure 5.5: Summer day heat fluxes: a) With opened blinds; b) With closed blinds

- Case B (SS50Clear glass type): Ventilated facade: Outdoor glass 16 mm, $\tau_s = 29.7\%$, $\rho_s = 5.6\%$, $\epsilon_t = 0.84$, air channel is 55 cm width, and indoor glazing is 6-12-8. The features of the 6 mm glass are: $\tau_s = 56.6\%$, $\rho_s = 17.7\%$, $\epsilon_t = 0.10$ whereas the 8 mm glass presents $\tau_s = 71.2\%$, $\rho_s = 7.2\%$, $\epsilon_t = 0.84$
- Case C (California glass type): Ventilated facade: Outdoor glass 12 mm, $\tau_s = 32\%$, $\rho_s = 19\%$, $\epsilon_t = 0.84$, air channel and indoor glazing with the same features than Case B

The heat fluxes produced through the facade during a summer day are shown in Figures 5.5(a) and 5.5(b) for a situation with the blinds opened and closed.

Positive values represent energy fluxes entering in the building, which have to be compensated with air-conditioning; otherwise, negative values represent thermal heat losses, which should be compensated with heating consumption. Total energy entering through the facade during the whole year are represented in Figures 5.6(a) and 5.6(b) for the cases described and the two positions of the blind.

The three options considered in the previous figures show that the design with a double skin facade presents lower heat gains than that with only one skin. The two double skin cases considered produce quite similar internal heat gains and losses, the main difference between them was economic. The use of a double skin ventilated facade helps to reduce the energy consumption due to air-conditioning. This feature

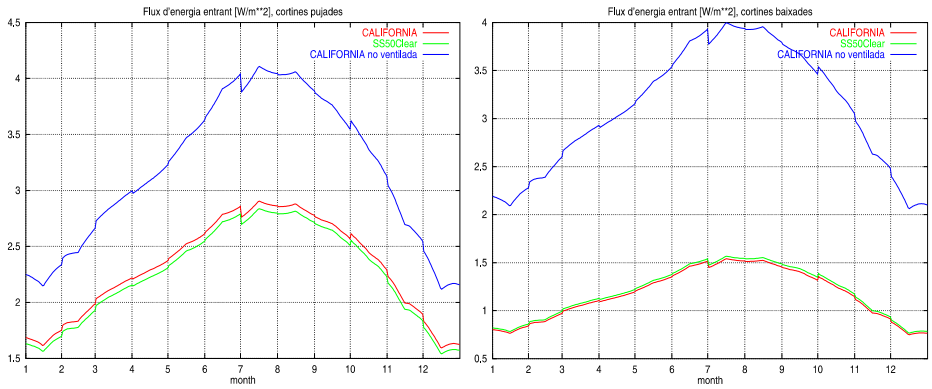

(a) (b)

Figure 5.6: Entering heat flux [W/m^2]: a) With opened blinds; b) With closed blinds

is shown in Table 5.1. In this Table, the cooling needs of each option are referred to the non-ventilated case, the case C presents 38% of the cooling needs of the single skin facade when the blind is closed.

Other important aspect to deal with in transparent glazed facades, is the temperature of the internal surface of the facade. The difference of temperature between the internal surface and the internal elements (like human beings), results in radiative heat transfer which may produce a disconfort situation. In the double skin ventilated facade, this temperature difference is lower than for a single envelope, as it is shown in Table 5.2.

5.2.4 Conclusions

Numerical simulations carried out with the numerical code described within this thesis, have allowed to quantify the advantages that a double skin envelope design could present in reference to a single skin design. The numerical optimization developed considered different channel possibilities, the use of internal and/or channel blinds and different climatic conditions. The results obtained helped the architecture team and propietary of the building to choose the suitable glasses in order to keep the aesthetics requirements originally foreseen, reducing at the same time, the energy consumption. As a consequence of the effort applied to the

Table 5.1: Annual indoor heat fluxes

	Thermal indoor gains $[kW-h/m^2year]$	Percentage of cooling needs in reference with the option A (conventional facade)
With blind		
Non ventilated facade (A)	314	100%
Ventilated facade B	121	38.6%
Ventilated facade C	119	37.8%
Without blind		
Non ventilated facade (A)	323	100%
Ventilated facade B	229	70.9%
Ventilated facade C	235	72.8%

Table 5.2: Maximum indoor wall surface temperature

	Maximum indoor wall temp. - indoor air temperature $[^\circ C]$	Percentage of reduction of the difference between maximum indoor wall temperature and indoor air temperature in reference with the option A (conventional facade)
With blind		
Non ventilated facade (A)	34.58-24=10.58	100%
Ventilated facade B	30.10-24=6.10	42.3%
Ventilated facade C	29.87-24=5.87	44.5%

energetic optimisation of the facade together with the application of a programm of environmental management, this building has received ISO 14001 certification.

5.3 *Agbar tower* assistance design

(a) (b)

Figure 5.7: *Agbar Tower building*: a) Detail of the construction of the external concrete facade with the internal windows areas; b)General external view.

This building is constituted by an ovoid central body (main services) encircled by a larger one. The space between the central body and the external one is used for offices. The total height of the building is 142 m, it is constituted until the 26th level (109 m) by a concrete structure with artesanal distributed huecos for the windows (Figure 5.7(a)). Concrete is covered by coloured aluminium plates and finally all the concrete layer is covered by a second transparent skin, formed by glass slats with variable slope, type and serigraphy levels. The top zone of the building (33 m) is constituted by a dome whose both skins are formed by glass layers.

The consultancy work was focused on the following items:

- Numerical analysis of representative zones of the concrete areas, variable in azimuth and composition, in order to quantify heat gains and losses through these zones, and maximum temperatures of internal opaque surfaces and windows.

- Numerical analysis of the dome zone. The main purpose of this study is to quantify the heat gains through this area, maximum temperatures of

the internal glass surface and adequacy of the selected serigraphys levels in internal and external skin.

5.3.1 Bottom zone: integrated annual values

The bottom zone of the building was divided in six zones, from 0 to 5, corresponding to different heights and positions in the perimeter of the building. Each one of these zones was divided in a number of facades, differentiated by its azymuth and geometric composition. Each facade, in turn, has been divided in a number of zones, according to the features of the glasses of the external skin, the composition of the internal skin and the corresponding storey level.

The treatment of the composition of this zone of the building is summarized in Table 5.3.

Table 5.3: Geometric composition of the bottom zone of the building

	Number of facades	Azymuth of the extreme facades			Total height [m]
FUSTE 0	14	22	59	SO	10.45
FUSTE 1	24	140	−153	N	18.76
FUSTE 2	24	59	140	NO	18.24
FUSTE 3	14	22	59	SO	18.42
FUSTE 4	23	−41.5	22	S	18.03
FUSTE 5	14	−153	−113.5	NE	18.42

Tables 5.4 and 5.5 show the thermo-physical and optical properties of some areas of the bottom zone of the building, used during a numerical simulation.

Table 5.4: Thermo-physical properties of the opaque internal layer

Material	Thickness [cm]	ρ $[kg/m^3]$	cp[J/kg $^\circ C$]	λ	ϵ_o
Ondulated plate	0.12	2700	921	180	0.8
Air chamber	10.5	1.17	1005	0.027	
Insulation	4	35	840	0.036	
Concrete	30	2400	1090	1.63	0.9

Table 5.5: Optical and thermo-physical properties of internal double glazing

	ρ_o	α_o	ϵ_o	τ	ρ_i	α_i	ϵ_i	w	ρ	cp	λ
External	0.07	0.11	0.84	0.82	0.07	0.11	0.1	6	2500	795	1.1
Air gap	-	-	-	-	-	-	-	15	-	-	-
Internal	0.07	0.08	0.84	0.85	0.07	0.08	0.84	4	2500	795	1.1

As has been stated in chapter 2, numerical code verifies the global balance of the facade (Eq. 2.138), which is the following:

Outdoor gains = Indoor gains + Enthalpic gains in channel + Stored energy

$$Qout = Qin + Qca + Qsto$$

These values integrated for the whole year are shown in Table 5.6 for the five zones of the bottom area of the building chosen as representatives.

Table 5.6: Integrated annual values of the variables conforming the global balance $[kWh/m^2]$.

FUSTES	$Qout$	Qin	$Qsto$	Qca	I	η_i	η_c
0	482.4	219.3	11.2	252.0	1446.2	0.15	0.17
1	202.9	124.5	9.6	69.0	631.3	0.20	0.11
2	331.6	180.5	11.3	139.9	1033.2	0.17	0.14
3	446.9	196.6	13.4	236.9	1446.1	0.14	0.16
4	474.6	203.4	13.8	257.5	1517.3	0.13	0.17
5	319.7	212.9	10.1	96.8	863.3	0.25	0.11

The internal gains are constituted by a solar contribution, plus radiation and convection internal heat transfer (Eq. 2.137).

$$Qin = Qs + Qtr + Qc$$

These variables are represented in Figure 5.8.

All the zones have similar composition, varying the disposition of the transparent and opaque zones and the azymuth. From the numerical analysis, it is deduced that the outstanding heat gains are due to solar radiation, whereas thermal radiation and convective gains are negligible when total integrated annual values are considered. The zones with larger south oriented areas present larger heat gains. This zone of the building was numerically studied considering that it was constituted by the internal

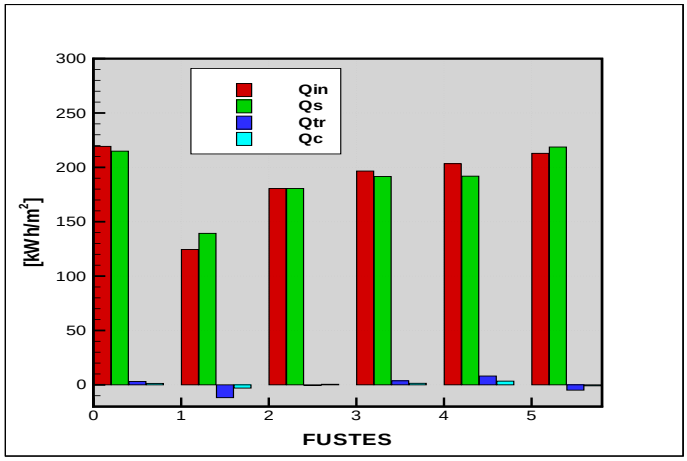

Figure 5.8: Annual integrated internal gains produced in bottom zone.

skin (single skin facade) formed by the windows areas plus the opaque zones. As result of the daily, monthly and annual analysis, it was concluded that the internal gains were larger for this last case. This is due to the larger solar gains in this case (although incident solar radiation is lower), at the same time heat losses are also larger for the case with a single skin. The average value of the fraction of positive internal gains for all this zone of the building is $\eta_{ip} = 0.25$ for the single skin case, while $\eta_{ip} = 0.19$ for the double skin configuration.

5.3.2 Top zone: dome

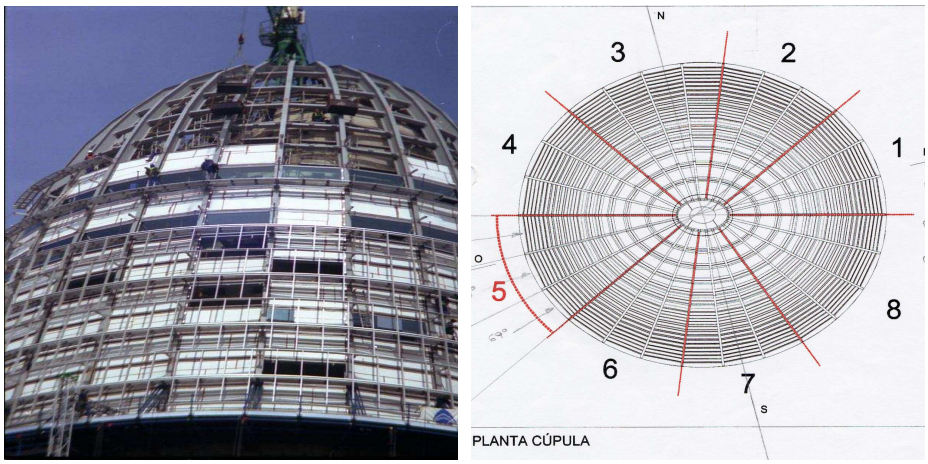

(a) (b)

Figure 5.9: *Agbar Tower building*: a) Detail of the dome zone; b)The dome was divided in eight meridians.

Building's dome requires an exhaustiv energetic analysis since it will be the most exposed area (1935 m^2). It is formed by a double skin, whose external layer is constituted by slats, with different optic properties, slopes and levels of serigraphy. The internal layer is constituted by a double glazing which presents different properties, levels of serigraphy and films coatings.

To analyse the thermal performance of the dome, it has been divided in eight vertical segments (Figure 5.9) Each segment or meridian has been, moreover divided in two or three sub-meridians with their corresponding azymuth. Each one of these sub-meridians is constituted by a number of facades, and each facade, is constituted by a number of zones, differentiated in function of the geometry and thermo-physical properties.

Furthermore, the dome has been also separated in four horizontal areas or rings. A total of 232 facades and 1974 zones have been numerically solved. The development of the dome is shown in Figure 5.10, where the different levels of serigraphys in the internal skin are represented by different colours.

The numerical work developed has been focused on the following items:

- Annual integrated heat gains and losses for each meridian of the dome.

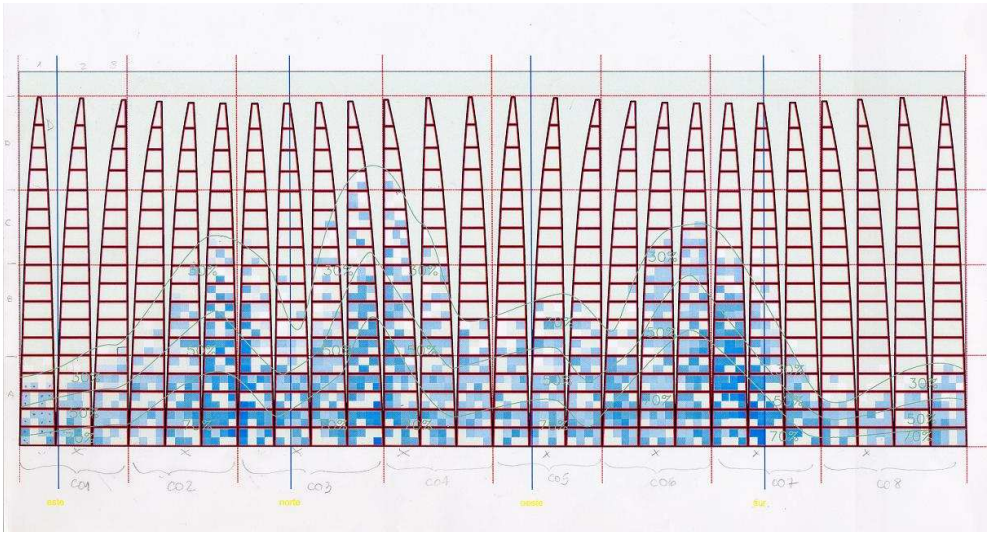

Figure 5.10: Development of internal skin of dome

- Monthly integrated heat gains and losses for each meridian of the dome.
- Analysis of inertia effects.
- Detailed analysis by rings of the dome .
- Analysis of variants in the design of the dome:
    1. External skin with serigraphys (as original project), internal skin without serigraphys.
    2. Without external skin, without serigraphys in the internal skin.
    3. Without external skin, with serigraphys in the internal skin.

As an example of the outputs analyzed during this work, Figure 5.11(a) shows the values of the variables of the global balance integrated during one year, for each meridian of the dome. Figure 5.11(b) shows instantaneous values of the global balance variables and external ambient and average internal surface temperature. Accumulated energy corresponds mainly to the energy stored in air. Figure 5.12 shows the annual integrated values of the heat fluxes conforming internal gains.

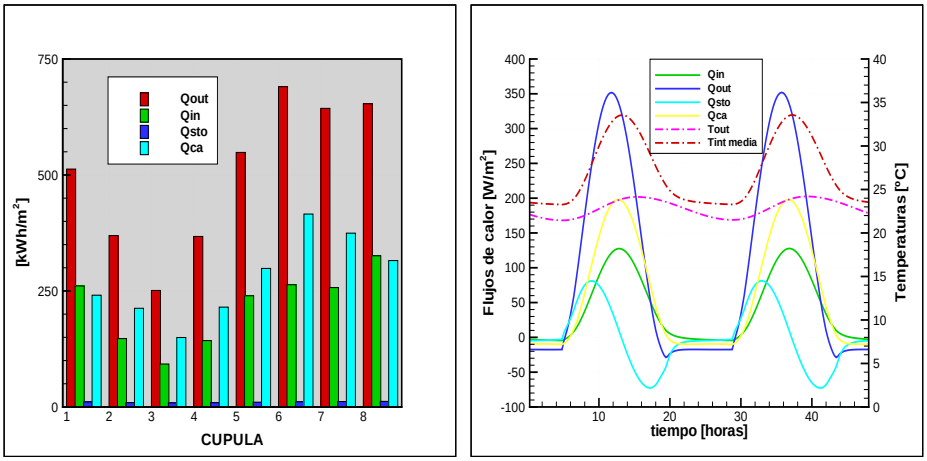

(a) (b)

Figure 5.11: *Agbar Tower dome*: a) Integrated annual variables of global balance for each meridian of dome; b)Instantaneous heat fluxes and temperatures for July 15th and 16th produced in seventh meridian of dome as a whole

Table 5.7: Integrated annual variables of the global balance for each meridian of the dome $[kW - h/m^2]$

CUPULA	$Qout$	Qin	$Qsto$	Qca	I	η_i	η_c
1	512.7	260.9	10.9	240.9	1285.2	0.20	0.19
2	369.4	147.4	9.3	212.7	946.0	0.16	0.22
3	251.1	92.6	8.8	149.7	755.7	0.12	0.20
4	367.5	143.1	9.2	215.2	967.4	0.15	0.22
5	548.6	239.7	10.3	298.6	1302.2	0.18	0.23
6	690.3	263.5	11.1	415.8	1589.7	0.17	0.26
7	643.6	257.3	11.7	374.6	1699.5	0.15	0.22
8	653.5	325.9	12.0	315.6	1623.6	0.20	0.19

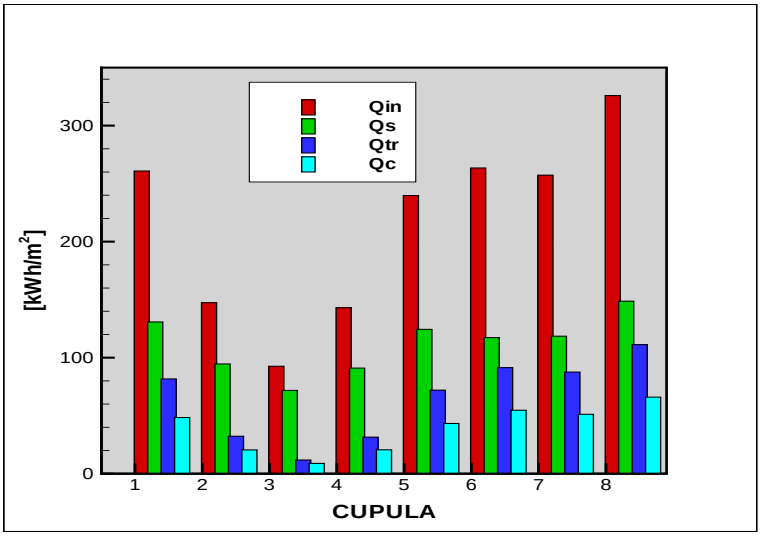

Figure 5.12: Integrated annual variables of internal gains for each meridian of dome

5.3.3 Conclusions

The dome presents different serigraphy levels in the external and internal surface. The proper combination of these levels allows to keep the hotter surfaces in the external surfaces. The south oriented dome zones have larger incident solar radiation (I in Table 5.7), however, solar gains (Q_s in Figure 5.12) are comparable to the rest of the zones. This is due to the proper combination of serigraphys in external and internal skins, and glass type in the external skin. Thus, the zone with north orientation is constituted by a large surface without serigraphy. Internal gains due to thermal radiation and convection are much important in this case compared to the bottom zone of the building. As average annual value, positive internal gains are 22% of the solar incident radiation.

5.4 *La Rioja Association of Industrial Engineers*, facade assistance design

This building is formed by four facades south, north, east and west oriented, with a height equal to 3.20 m. The geometric configuration is shown in Table 5.8.

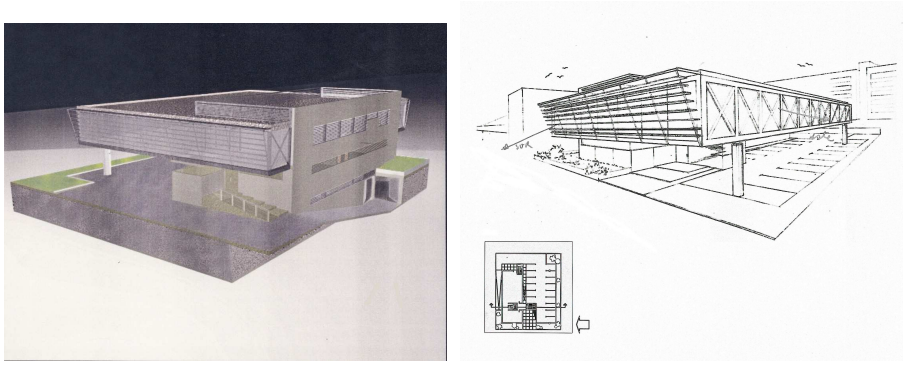

(a) (b)

Figure 5.13: Views of the building: a)West facade (partially transparent) b)South and east facades.

Table 5.8: Description of the facades

Facade	Height [m]	Width [m]	Azymuth
South	3.20	22.50	18° (south-west)
North	3.20	22.50	-162° (north-east)
East	3.20	30.0	-72°
West	3.20	30.0	108°

South, north and east facades are completely constituted by glass surfaces (Figure 5.13), west facade is formed by a combination of windows areas with opaque zones (72.72 m^2 opaque and 24.45 m^2 windows).

The study carried out for this building was focused on:

- Helping in the choice of the most suitable glasses for the transparent facades.
- Analysis of the maximum temperatures produced in the internal surfaces of the four facades.
- Incidence of overheating in transparent facades.
- Comparison of the single and the double skin facade thermal performance.

South, east and west facades are surrounded by neighbouring buildings which produce partial shadows over the facades. Incident solar radiation over each surface

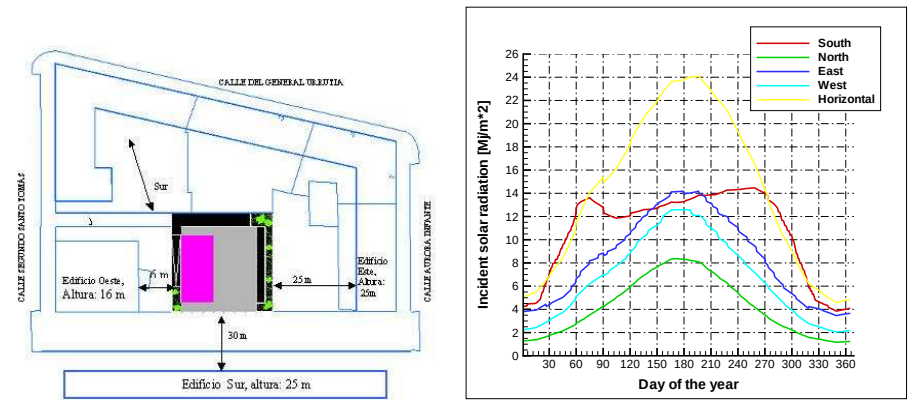

(a) (b)

Figure 5.14: Shadowing effects: a)Scheme of the position of neighbouring buildings to take into account shadows effects. b)Incident solar radiation over each facade of the building

has been calculated, according to the scheme shown in Figure 5.14(a), resulting in a reduction of incident radiation as shown in Figure 5.14(b). Each point of this curve represents a daily integrated value, during winter months available radiation is larger for the south facade.

Facades south, east and north were numerically simulated as single and double skin facades. The variables of the global balance are represented in Figure 5.15(a) for the single skin case and in Figure 5.15(b) for the double skin case, as annual integrated values.

It is observed that for the single skin case, external gains are converted totally into internal gains (not accumulated energy), in the case with an additional external skin, internal gains become reduced related to the external gains because of the effect of the air channel, but they do not differ outstandingly from those values obtained in the case with only one skin in the facade.

The variables which conform the internal gains are shown in Figure 5.16 for both options, as annual integrated values.

The internal thermal radiation and convection constitute always a thermal loss for the single skin case, whereas they are net thermal gains in the double skin case, for south and east facades. Although the net internal gains are quite similar for both facade configurations, solar gains are larger for the single skin case, this produces that the internal positive gains (heat that must be eliminated by air-conditioning) to

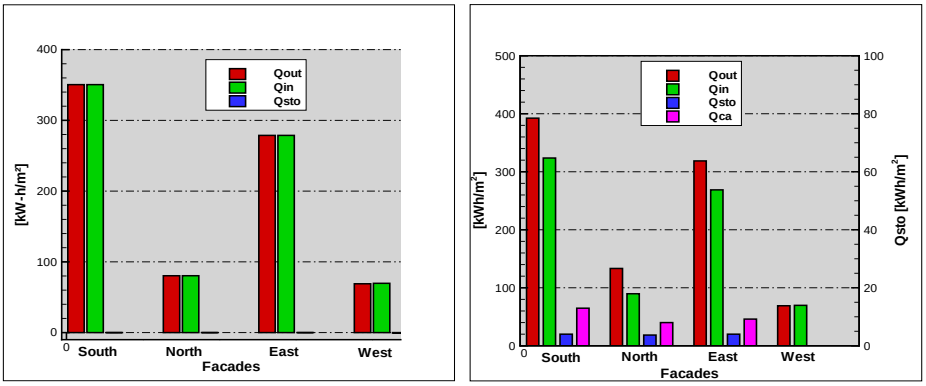

(a) (b)

Figure 5.15: Global balance of the facades: a)Single skin in facades south, north and east b)Double skin

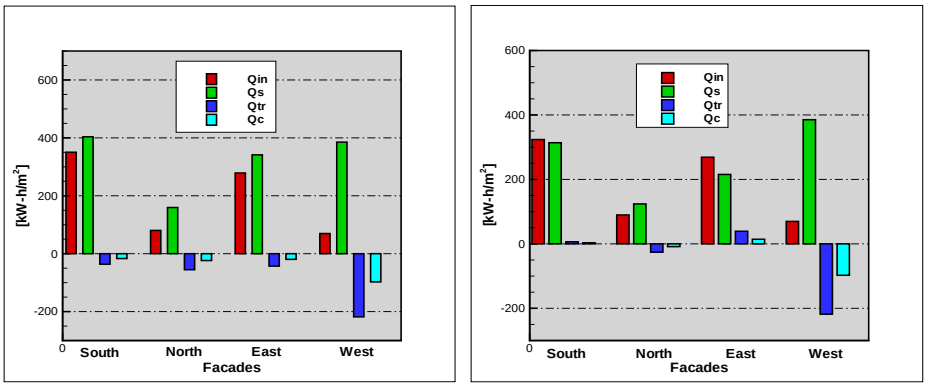

(a) (b)

Figure 5.16: Internal gains: a)Single skin in facades south, north and east b)Double skin

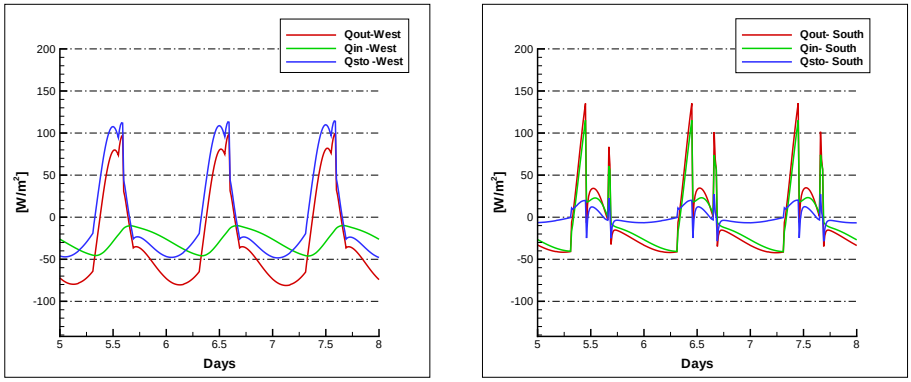

Figure 5.17: Total external energy $Qout$, internal net gains Qin and stored energy $Qsto$ from 5 to 8th January. At left, for a west facade and at right, for the south facade, single skin configuration. For the south case, it is observed the reduction of solar gains at noon, due to the shadows effects of the neighbouring buildings.

be larger for the single skin case.

5.4.1 Thermal inertia and maximum temperatures

Inertia performance can be only analyzed from instantaneous behaviour, since the integrated variables hide the charge and discharge processes. Figure 5.17 shows the heat fluxes in a succession of four january days, for the south facade and a zone constituted by opaque areas of the west facade for a single skin. South facade is not able to accumulate energy since it is completely constituted by glass ($Qsto$ curve), the opaque zones have a larger accumulation capacity, this produces a reduction in the heat gains.

Figure 5.18 presents the maximum temperatures of the internal surface of each facade (MAIWT), in the case of a single skin configuration.

Figure 5.19 represents the monthly internal gains coefficient (η_{ip}) for each facade, considering single and double skin configuration. This coefficient indicates the energy that penetrates the building through the facades, in relation to the incident solar radiation. This value is lower for the double skin facades, since a part of the available energy is transformed in air channel gains.

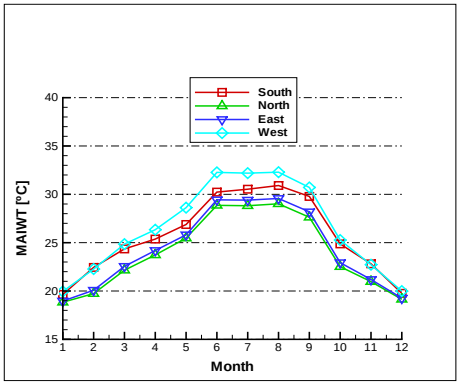

Figure 5.18: Monthly maximum temperature of the internal glass or opaque surface. Single skin configuration

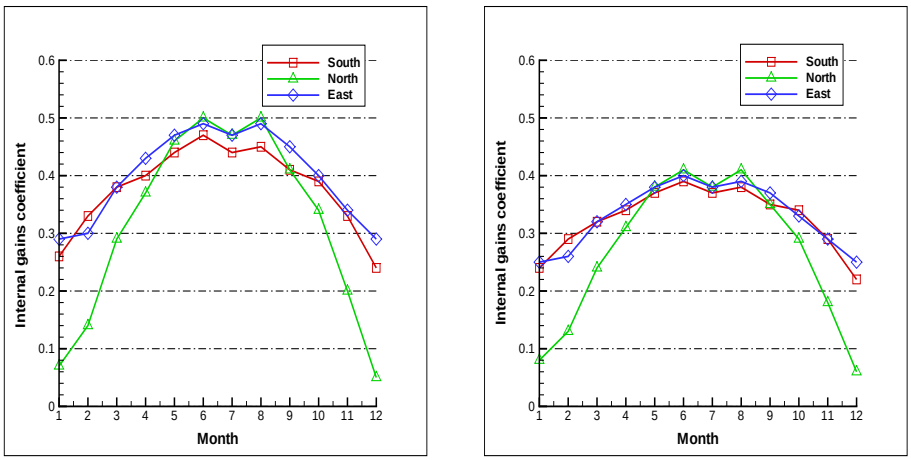

Figure 5.19: Monthly internal gains coefficient for each facade, at left for a single skin configuration, at right considering a double skin implementation.

5.4.2 Conclusions

As general conclusions of this work, it may be stated the following results:

- One of the key aspects of this project has been the glasses selection. The numerical analysis has shown that during the air-conditioning period, the heat gains through the facade are larger for the west facade (however it is constituted by opaque zones), it confirms that the glasses present a suitable solar control performance.
- During heating period, although the building presents large surfaces completely transparent, the heat losses remain low, thus reducing the heating consumption. Once again, the west facade is the one that presents larger heat losses and heat gains.
- Maximum temperatures remain in an acceptable level during the hotter months, for all the facades.
- As conclusiones from the comparison with a double skin configuration in the transparent facades, it may be inferred that in this case, thermal inertia of the building is increased, and global heat losses and gains become reduced.

5.5 General conclusions

This chapter has dealt with some practical applications of the numerical tool developed, for the design and optimization of real-building facades. The numerical prediction of monthly and instantaneous heat gains and losses allow to calculate the heating and air-conditioning equipment necessary to keep comfortable internal conditions. Moreover, the implementation of innovative designs as an air channel between two skins of the facade, or advanced passive implementations, may be numerically tested to foresee its thermal behaviour. The results presented in this chapter show the usefullness of the developed tools.

References

[1] D. Faggembauu, A. Oliva, M. Costa, and M. Soria. Numerical analysis of the fluid-dynamic and thermal behaviour of the double envelope of the Agbar tower, designed by the architectures Ateliers Jean Nouvel and B720 Arquitecturas S.L. Technical report, 2002.

[2] D. Faggembauu, M. Costa, M. Soria, and A. Oliva. Simulation of the thermal and fluid-dynamic behaviour of ventilated facades for Caixa of Terrassa-building by J. Baca architect. Technical report, 1999.

[3] D. Faggembauu and A. Oliva. Numerical analysis of the thermal and fluid-dynamics behaviour of the facades for the new headquarters of the Association of Industrial Engineers in La Rioja. Architecture Portales Ingenieria, S. A. Technical report, 2005.

Chapter 6

Conclusions

6.1 Concluding remarks

This thesis pretends to be a contribution to the field of dynamic building simulation, focusing on solving in the most accurate, but time-affordable manner, heat transfer and fluid flow in single and double skin facades. This field is an important one, to achieve low-energy, efficient consuming buildings.

This work introduces a specific numerical code, based on the one-dimensional and transient numerical resolution of the governing equations (continuity, momentum and energy) in the whole facade domain. Since the objective is to simulate the thermal behaviour during long time periods (typically one year), it is necessary to use one-dimensional models in order to keep a low CPU time.

One-dimensionality varies according to the preponderant direction of heat flow in each zone of the domain, thus, it considers the indoor-outdoor direction for the glazed and opaque areas, and the flow direction for the air channel. The objective of the numerical tool is to allow the evaluation of the performance of the facades over the course of one year. Additionally, it introduces advanced elements into the composition of the facade, such as phase change materials, selective surfaces, special glazing, transparent insulation materials and integrated collectors-accumulators. Numerical simulation is carried out from basic thermo-physical properties of the materials and geometric information.

The numerical models implemented within the numerical tool have been submitted to a verification and validation process in different forms. The numerical code was verified at the first stage by comparing the numerical results with those obtained for simplified situations with analytical solutions. In a second stage, a comparison with tabulated global performance coefficients of simple facade configurations was carried out, and a comparison with the results of other building simulation codes was developed according to the methodology proposed by *BESTEST* procedure. Experimental research has been carried out in test cells

situated at different geographical locations, thus they were subjected to different climatic conditions. It has been focused on measures of temperatures and heat fluxes at the surfaces of the facade. This task has produced good results, allowing to conclude that however, the numerical tool is limited to one-dimensional models, it is able to predict the thermal performance of these advanced facades in an accurate mode.

A *standard* double skin facade has been defined and it has been extensively numerically studied, comparing its performance with single skin facades constituted by different materials. From the simulation results, a lot of information about the thermal behaviour is generated, for this reason, performance parameters have been defined in order to characterize different designs, these parameters are time-integrated or instantaneous. They have been defined as the ratio of net internal gains (η_i), the ratio of positive internal gains (η_{ip}), the ratio of air channel enthalpic gains (η_c), and the ratio of heat losses (ζ_{el}).

Since, for each climatic condition and constructive solution, the main goal of the facade in relation to its thermal behaviour, may vary (for instance, it may be to get a reduction of solar gains, or to increase them or to get low surface temperatures), it is not logical to define a thermal efficiency parameter, but performance parameters. In Mediterranean climates, the transparent facades usually have problems of overheating, thus, an efficient facade would be one with low rate of internal gains. In other climatic conditions, however, heat losses are the main inconvenient of large glazed areas. Emphasis has been paid in this work, in facades constituted by transparent insulation, since they allow to combine transparency with low heat losses. The parametric study of facades constituted by transparent insulation, shows that an accurate long term performance analysis is necessary to achieve the most suitable designs for a given climatic condition. Since the effects of properties or geometrical parameters produce differentiated transient behaviours, during day and night and at different periods of the year, a transient analysis is essential. In this sense, the usefullness of numerical tools like the one described in this thesis is relevant.

The possibilities of reducing energy consumption dedicated to heating and production of domestic hot water are numerically analyzed. This reduction has been focused on the possibilities that the facade may offer to integrate collectors and water-accumulators on its surface, considering that not allways it is possible to have roof space available to integrate active solar systems. This would be one of the advantages of these systems, furthermore, profit may be obtained from the opaque zones of facades, which can present an attractive external design, combined with a usual internal aspect. These designs have been numerically tested considering different levels of insulation in the building and domestic hot water consumption profiles. Their performance is strongly dependent on azymuth of captating surfaces,

optical properties of the materials and climatic conditions, therefore numerical optimisation is a mandatory task to implement adequated designs.

The numerical models described within this thesis have been applied to the design and optimisation of facades of real buildings. Some of these results are presented. The numerical outputs have focused on: i)helping the engineering team in charge of the HVAC system, ii)giving information to help in the decission about the most convenient glasses, iii)analysing different flow regimes in air channel of double skin facades, in order to achieve the design objectives, iv)testing different design elements, like inertia, coatings, shadows, etc., v)obtaining a complete outlook of the thermal performance of the facades, in terms of temperatures and heat fluxes through it. Numerical code becomes a testing bank of different architectonic proposals, in order to help in the design of innovative solutions, always having in mind, the optimisation of building energy consumption.

6.2 Future actions

This development constitutes a first, but solid step for the evolution towards a full-building simulation tool. Additional work is necessary to continue progressing in this field. Future actions are focused on different aspects, regarding the numerical models, the following steps are considered:

- Additional numerical models have to be incorporated in order to improve the indoor thermal simulation.
- Additional shadows elements have to be considered, at this moment, awnings, overhangs and curtains are considered, but also vertical adjacent fabric elements and louvers should be taken into consideration.
- Modelling of illumination performance.
- Implementation of additional thermostatic control.
- Improvement of heat transfer coefficients, for specific design conditions.
- Improvement of air channel model, fed from the experimental research.

Regarding the experimental infrastructure, future work may be divided in two types:

- Improvement of the experimental work carried out on the integral facade in real outdoor climatic conditions, in order to determine the air conditioning and/or heating consumption of different variants, the behaviour of the designs with collector-accumulators in the processes of charge and discharge, and the air behaviour in the facade channel.

- Experimental work in Laboratory controlled conditions, in order to obtain or verify the heat transfer coefficients (for instance, in water accumulator, or in closed and/or opened air channel) acquired from more detailed numerical simulations.

Additionally, graphical friendly interfaces for data input and output should be implemented in the near future, with the incorporation of databases of materials, properties and packages of constructive implementations.

As final aspect, the link of this numerical code with a multi-dimensional simulation of specific zones, like the air channel or a room, may be affordable in the future, accounting with the incresing computing power, the use of improved turbulence models, and the possibilities of multi-processing in computer clusters. Information about the local and global heat transfer coefficients, will allow to predict even more accurately thermal behaviour for relevants periods of time.

Publications originated from this work

Publications in International Journals

- D. Faggembauu, M. Costa, M. Soria, A. Oliva. Numerical analysis of the thermal behaviour of ventilated glazed facades in Mediterranean Climates. Part I: Development and validation of a numerical model. Solar Energy journal.Vol 75 (2003), pp: 217-228.
- D. Faggembauu, M. Costa, M. Soria, A. Oliva. Numerical analysis of the thermal behaviour of ventilated glazed facades in Mediterranean Climates. Part II: Applications and analysis of results. Solar Energy journal. Vol 75 (2003), pp: 229-239.
- D. Faggembauu, M. Costa, M. Soria, A. Oliva. Modelling of single and double skin advanced facades with transparent insulation materials. Submitted to Solar Energy journal.

Publications in Proceedings

- M. Soria, M. Costa, H. Schweiger, D. Faggembauu, A. Oliva. Simulación numérica y optimización de fachadas multifuncionales ventiladas. In *XIII Congreso Nacional de Ingeniería Mecánica.* Año 12, Volume: 4, pp. 643-648, Terrassa. 1998.
- D. Faggembauu, M. Costa, M. Soria. Diseño de fachadas multifuncionales ventiladas utilizadas como sistemas térmicos pasivos. In *XIIII Congreso Asociación Argentina de Energía Solar.* Revista especial ASADES, Argentina. 2000.
- M. Costa,.D. Faggembauu, M. Soria, C.Farré. Comparación y Descripción de difererentes niveles de simulación numérica de la piel de un edificio, concebida como elemento pasivo de diseño. In *Proceedings XIV Congreso Nacional de Ingeniería Mecánica.* Año 13, Volume 3, pp. 1634-1639, Leganés. 2000.
- T. Ojanen, I. Heimonen, C Simonson., M. Costa, M. Soria, D. Faggembauu. PV Panel Siding for Renovation of Walls, Part I: Thermal Performance Experiments in Northern climate conditions. In *Proceedings EuroSun 2000 Conference.* Copenhagen. 2000.
- M. Soria, D. Faggembauu,M. Costa, T. Ojanen, I: Heimonen, C. Simonson. PV Panel Siding for Renovation of Walls, Part II: Numerical Analysis. In *Proceedings EuroSun 2000 Conference.* Copenhagen. 2000.

- D. Faggembauu, M. Soria, M. Costa, A. Oliva. Simulación Numérica y Validación Experimental de fachadas ventiladas mediante el software *AGLA*. In *IX Congreso Ibérico de Energía Solar, III Jornadas Técnicas sobre Biomasa.* Córdoba. 2000.
- D. Faggembauu, M. .Costa, M. Soria, A. Oliva. Strategies To Reduce Thermal Overheating In Mediterranean Climates Using Large Glazed Areas. In *International Forum on Renewable Energies (FIER 2002).* Tetouan. 2002.
- D. Faggembauu, M. .Costa, M. Soria, A. Oliva. Description and analysis of a specific numerical simulation tool to simulate double skin facades. Application to the study of advanced facades with integrated collectors-accumulators. In*ISES Solar World Congress 2003.* Göteborg, Sweden. 2003.
- D. Faggembauu, D.Kizildag, A. Oliva, J. Cadafalch. Advanced Solar Facades with Integrated Collectors-Accumulators for domestic hot water and space heating applications. In *Proceedings EuroSun 2004.* Freiburg, Germany. 2004.
- D. Faggembauu, A. Oliva, M. Soria. Analysis of transient effects on the performance of advanced double and single skin facades including transparent insulation. Numerical study and experimental validation. In *Proceedings EuroSun 2006 Conference.* Glasgow. 2006.